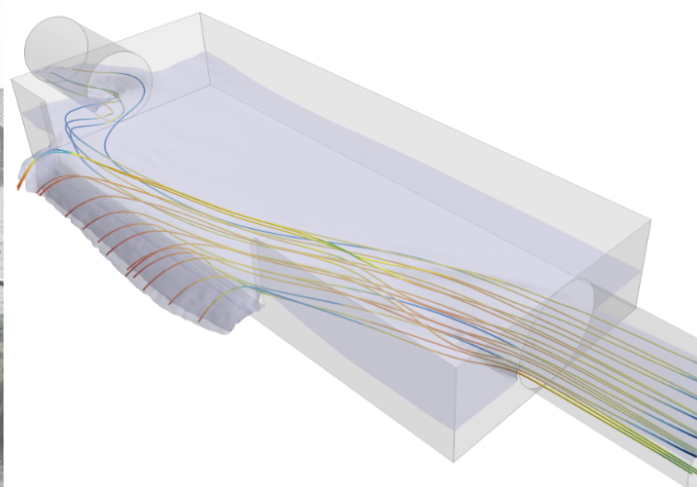
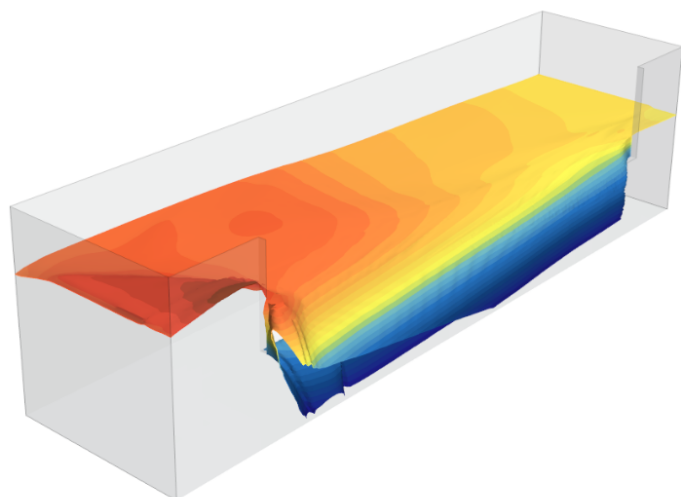


Predicting Rating Curves for Combined Sewer Overflows



Author:

Mathias Ulsted Jackerott

Supervisors:

Michael R. Rasmussen
Jesper Ellerbæk Nielsen
Rasmus Nielsen

June 9, 2023



AALBORG UNIVERSITY
STUDENT REPORT

Department of the Built Environment

Thomas Manns Vej 23

9220 Aalborg Ø

<https://www.en.build.aau.dk/>

Title: Predicting Rating Curves for Combined Sewer Overflows

Project: Master thesis of MSc Water and Environmental Engineering

Project period: Autumn semester 2022 and spring semester 2023

Supervisors:

Michael R. Rasmussen

Jesper Ellerbæk Nielsen

Rasmus Nielsen

Author:

A handwritten signature in blue ink that reads "Mathias Jackerott".

Mathias Ulsted Jackerott

Pages: 100

Appendices: 20

Synopsis:

En metode til at forudsige Q-h kurver for overløbsbygværker er blevet udviklet med afsæt i to forskellige typer af overløbsbygværker; sideoverløb og lige-på-overløb. Q-h kurven kan forudsiges ved kendskab til 3 parametre; overløbskoefficienten, rists hydrauliske modstand og kapaciteten af udløbsledningen. Via CFD modellering af tilfældigt genererede overløbsbygværker er overløbskoefficienten blevet relateret til det opstrøms Froudes tal i kammeret samt bredden af overløbskronen, og kan forudsiges ved kendskab til disse. Metoder til at estimere en rists hydrauliske modstand er blevet fremsat, og metoder til derefter at relatere den hydrauliske modstand af risten til et reduceret flow over overløbskanten er blevet udviklet for horisontalt og vertikalt monterede riste. Metoderne er blevet valideret via CFD modellering og laboratorieforsøg og har vist sig at være præcise. Kapaciteten af udløbsledningen er blevet estimeret vha. en simpel hydraulisk model. Q-h relationer er blevet forudsagt for 5 laserscannede overløbsbygværker og sammenlignet med CFD modeller samt målte data. De forudsagte Q-h relationer er blevet vurderet som værende præcise for de overløbsbygværker, der passer i en af de to overnævnte typer. En kalibreringsmetode til fastsættelse af overløbskanten er udviklet, og er i kombination med de forudsagte Q-h kurver benyttet til at estimere årlige overløbsmængder.

Foreword

This report represents a 45 ECTS master project at the education of Water and Environmental Engineering at Aalborg University. The project obtained data from the Danish MUDP Lighthouse project called Overløb. I would like to thank Lasse Sørensen from Vandcenter Syd for sharing his knowledge and providing data, as well as Ane Loft Møllerup from Novafoss for their data contribution. Additionally, I would like to thank Morten Borup from Kryger for his insights into the modeling of the downstream sewer system and Malte Ahm for showing interest in the project. Lastly, I am thankful to my three supervisors, Michael R. Rasmussen, Jesper Ellerbæk Nielsen, and Rasmus Nielsen, for their excellent guidance and engaging discussions.

Abstract

This project presents a method to predict the rating curves of combined sewer overflow (CSO) structures based on the geometry of the structure and the connected sewer system. 3 important parameters have been found to influence the rating curve; the weir coefficient, the capacity of the discharge pipe and the resistance induced by potential screens. Methods to predict the weir coefficient have been proposed for two types of CSO structures being side weir and stilling pond CSO structures. Furthermore the location for installing a water level sensor giving the best prediction has been determined. Based on CFD modelling of close to a thousand randomly generated CSO structures, it was found that the weir coefficient can be predicted based on the Froude number and the geometry of the weir crest. A method to relate the hydraulic resistance of a screen to the flow over a weir were proposed, and the method has been validated and found accurate based on laboratory experiments and CFD modelling. Based on the laboratory test it was further shown how the hydraulic resistance of the screen increased as the screen clogged. A simple model of the CSO discharge pipe has been proposed and validated against the results of CFD models.

Rating curves of 5 real life CSO structures have been predicted and compared with the results from CFD modelling and real-life measurements. The predicted rating curves have been deemed accurate for structures which falls within one of the two types of CSO structures.

Table of Content

Chapter 1 Introduction	1
1.1 CSO Structures	5
Chapter 2 Problem Statement	10
Chapter 3 The Weir Equation	12
Chapter 4 Experimental Methods	18
4.1 Experimental Setup - Sharp Crested Weir	18
4.2 Experimental Setup - Screens	20
Chapter 5 Computational Fluid Dynamics	23
5.1 CFD Model - Sharp Crested Weir	26
5.2 CFD Model - Ideal Channel	27
5.3 CFD Model - Stilling Pond CSO Chamber	28
5.4 CFD Model - Ideal Side Weir	30
5.5 CFD Model - Side Weir CSO Chamber	31
Chapter 6 Validation of CFD Modelling	33
6.1 Sensitivity Analysis	35
Chapter 7 Prediction of the Weir Coefficient	37
7.1 Stilling Pond	37
7.2 Ideal Side Weir	41
7.3 Side Weir CSO Chamber	47
7.4 Splitting up the Weir Coefficient	51
Chapter 8 Adjusting for CSO Fittings	54
8.1 Hydraulic Effects of Screens	56
8.2 CFD Model - Screens	58

8.3 Screens - Results	60
Chapter 9 Submersion of the Weir	65
9.1 Modelling the Downstream Network	67
Chapter 10 Comparison with real life CSO structures	70
10.1 Kalkværksvej	70
10.2 Fredtoftevej	73
10.3 Lindevangsvej	78
10.4 Bergsøe plads	80
10.5 Thulevej	82
Chapter 11 Discussion	85
Chapter 12 Conclusion	93
Chapter 13 Perspectives for Further Work	95
References	97
A Dimensional Analysis	101
B Derivation of the Weir Equation	104
C Correction for Surface Tension Effects	106
D Automatic Calibration of the Weir Crest	111
E Resistance of Bar Gratings	115
F Screen Resistance Calculations	117
G Horizontal Screen - Additional Results	118
H Weir Predictions Parameters	119

Introduction

1

Denmark, along with the rest of the EU, is committed to achieving the goals of the EU Water Framework Directive by 2027, which include attaining a good ecological status in all of the EU's waters. One of the ways to achieve this is by reducing the discharge of nutrients let into streams, rivers, lakes and seas. Since the 1990s, there has been a significant reduction in the yearly discharges of nitrogen and phosphorus in Denmark, primarily due to better management of fertilizer use and improved wastewater treatment [Jung-Madsen et al., 2021]. Examining pollution originating from point sources [Frank-Gopolos et al., 2021] approximates that urban runoff accounted for approximately 16% of nitrogen, 23% of phosphorus and 31% of Biochemical oxygen demand (BOD) of total annual discharges from point sources in 2020. Therefore, mitigating urban discharges would be an important measure toward attaining the objectives of the EU Water Framework Directive.

The urban runoff can be differentiated into two categories; combined sewer systems and separate sewer systems. In the combined sewer systems stormwater and wastewater are managed within a shared system, and all the water is transferred through the sewer system to the wastewater treatment plant. However, during periods of intense rainfall, the capacity of the system may be exceeded, resulting in water building up within the system. To prevent diluted wastewater from building up and posing risks to public health, combined sewer overflow (CSO) structures has been build. These CSO structures act as safety valves, redirecting the excess wastewater to a nearby water body. In separate sewer systems, the stormwater is kept separated from the wastewater, and the stormwater is discharged to a nearby water body and only the wastewater is led to the waste water treatment plant. The separate sewer system does therefore not experience excessive loads in the same way as the combined system.

Approximately half of the urban runoff pollutant load can be attributed to combined sewer overflows. The rest originates from separate urban drainage systems [Frank-Gopolos et al., 2021]. This is despite the fact that the discharged water volume from the separate systems is approximately 10 times larger than from the combined systems [Frank-Gopolos et al., 2021]. Despite lots of resources has been used

and are being used, replacing combined sewer systems with separate systems, thereby removing the possibility for sewer overflows as well as ensuring a more effective treatment of the wastewater at the treatment plant, the annual discharges from urban runoff has stayed approximately the same [Frank-Gopolos et al., 2021]. The explanation might be due to an increased population in combination with an increase in impermeable surfaces leading to increased strain on the system [Department for Environment Food and Rual Affairs, 2022]. In the future the strain on the system is suspected to increase even more due to more intense rain events, thereby leading to more frequent overflow events.

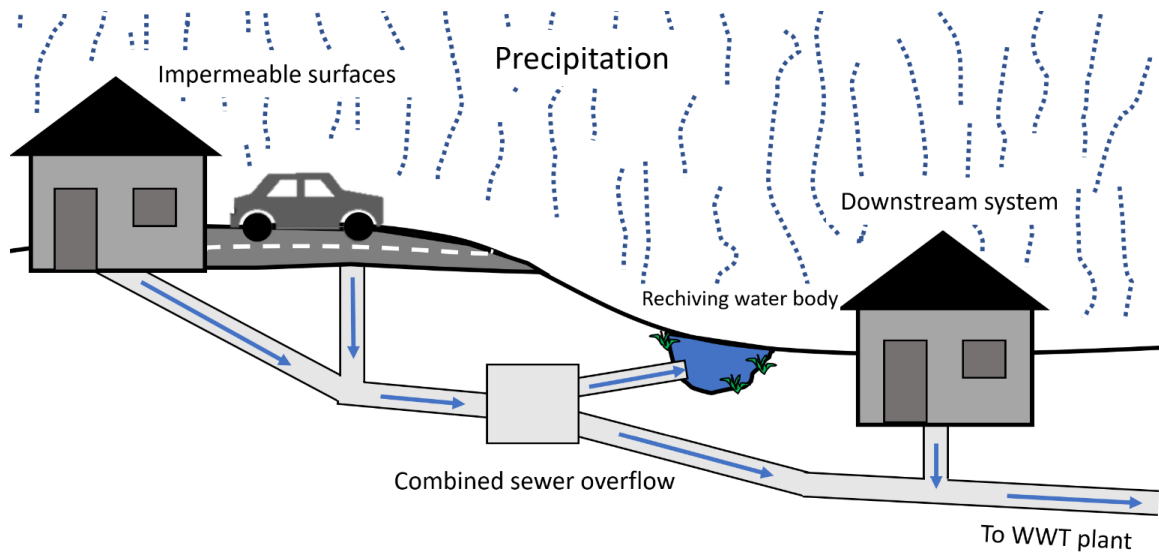


Figure 1.1. Illustration of a combined sewer system and the workings of a cobined sewer overflow.

While the annual discharge of nutrients from CSO's contributes only to a small portion of the overall nutrient discharge, their impact on the affected water bodies is significant. This is because the discharges happens over small periods of time, and affect vulnerable water systems such as streams. As a result the effect of combined sever overflows is reckoned to be larger than what the yearly discharge loads indicates. Problems with combined sewer overflows include the discharge of harmful pathogens into public bathing areas, acute ecological effects in the receiving water bodies due to oxygen depletion and toxification and aesthetic pollution by gross solids from the sewer system.

To avoid these problems, the policy in Denmark has been to convert the combined sewer systems into separate systems. Despite the fact that problems with combined sewer overflows can be solved by the transition to separate sewer systems, this has been found not to be without problems, as it leads to larger discharge volumes increasing the hydraulic loads. Furthermore the urban runoff has been reckoned not always to be as clean as expected. Recently a permission to discharge urban runoff to a nearby river was declined by the Environmental and Food Complaints Board

of Denmark, due to the river having too high concentrations of cobber, and thereby the discharge of additional cobber from the urban runoff were prohibited [Miljø- og Fødevareklagenævnet, 2023]. It is suspected that this decision will lead to an altered practice, not allowing for discharges of urban runoff containing substances for which the water quality standard is already surpassed [Horten, 2023], thereby questioning the premise of the separate sewer system as a solution to the problems with combined sewer overflows. Furthermore, the conversion of the sewer system is a very expensive, CO₂ emitting and time taking task, and many municipalities plan to finish converting their systems within 50 - 100 years from now [Aarhus Kommune, 2022] - many years too late to meet goals of the EU water framework directive.

Today only few resources are put into monitoring and handling the CSO discharges in general. In many cases very limited knowledge about the CSO structure itself is known, and in some cases the discharge permission has even been lost or forgotten [Moesgaard, 2021]. This lack of attention can be ascribed to a combination of the fact that most combined sewer systems were build many years ago and to the fact that the water companies have no financial interest in reducing the combined sewer overflows. As of today there is no tax on the discharge from CSO's. This is opposed to the discharge of treated waste water, where the water companies have to pay a discharge tax for the remaining pollutants after the treatment.

To deal with these problems and to put more attention to the problem with combined sewer overflows, the UK has in 2022 been the first country in the world to make a specific legislation addressing the problem with combined sewer overflows. In addition to setting ambitious goals for the reduction of CSO discharges, the plan also makes it mandatory for the water companies to "publish near real time data on the operation of storm overflows" [Department for Environment Food and Rual Affairs, 2022]. In Denmark the new government (SVM - Social Democrats, Liberal and Moderates) has in their government platform stated that it is their ambition to tax the discharge from CSO's with a higher rate than the discharge from waste water treatment plants [Regeringen, 2022] .

While simply increasing attention alone doesn't solve the issue with combined sewer overflows, increased focus on the CSO discharges can provide valuable information. It helps identify which CSO structures discharges most frequently or is responsible for the largest pollutant load. Such information can be used in decision-making and prioritization processes when transitioning from combined systems to separate systems. Additionally, increased focus and increased insight may lead to potential optimizations of the sewer system and CSO structures, resulting in reduced discharges.

The MUDP project (Development and Demonstration Project funded by the Danish Environmental Protection Agency), from which this project is based upon, is centered around this concept. The project, which spanned from 2020 to 2023, aims to reduce the discharges from CSO structures through data-driven decision-making [Madsen, 2021].

To assess the discharge of CSO's both the hydraulic loads and the concentration of the pollutants should be estimated. The pollutant concentration is in general very difficult to determine, as it depends on many parameters and processes. And in general the use of average concentrations is the standard practice [Nielsen et al., 2020]. The flow is likewise difficult to measure directly, as flow sensors are very expensive, unreliable and often are difficult or impossible to install in below ground sewer systems [Larrarte et al., 2021]. Often the flow can however be determined quite accurately indirectly, by relating the water level inside the CSO chamber with a discharge flow using a rating curve. The water level is opposed to the water flow cheap to measure using a ultrasonic sensor.

Traditionally, such rating curves have been based on the weir equation. When the water flows over the weir, the water transits from a sub to a supercritical flow. Upstream the weir the flow is therefore unaffected by the downstream conditions, and a unique relationship between the water level and the discharge flow exist. The weir equation is however based of idealised weirs and is only valid for such. In reality CSO-structures are however seldom build in accordance with the assumptions to which the weir equation is based of, and not even all CSO structures are weir based structures. Different kinds of CSO structures exhibit different flow patters and a universal weir equation is therefore not appropriate. The use of computational fluid dynamics (CFD) makes it possible to generate a rating curve fitting any CSO structure, almost no matter the complexity of the geometry. This has been done with success by several scientific papers [Malte Ahm and Rasmussen, 2016], [Fach et al., 2008]. However, the use of CFD requires high resolution knowledge of your CSO chamber and sewer system, and is computationally highly demanding. Furthermore the software is often too expensive for the water companies to consider. Therefore widespread use of CFD modelling to determine custom rating curves for CSO structures is not suspected to be seen within the near future.

This paper therefore sets out to develop a method to predict rating curves for CSO structures without the need for CFD modelling of that exact structure. This will be done by the categorising and modelling of different types of CSO structures, trying to find general trends adjusting the rating curve to adjust for the charastics of different structures.

1.1 CSO Structures

Combined sewer overflow structures (CSO structures) have been designed in a variety of ways, and no universal standard has been established. The design of the structure affects the hydraulic characteristics and thereby also the rating curve of the structure. Furthermore, CSO structures are often seen equipped with screens, scum boards or other installations that influence the hydraulics. It can therefore be challenging to determine which formula to use for which overflow structures and under which conditions it is valid. The task of generalising different overflow structures becomes further complicated by the fact that CSO structures often are built based on site-specific conditions. Furthermore, most of the CSO structures have been built several decades ago, and plans and information regarding the structures have in many cases been lost or forgotten. In many cases, the authorisation for the discharge itself is missing - giving the overall impression that the field in general is suffering from a lack of attention and documentation.

A systematic survey of 335 CSO structures from Aarhus municipality in Denmark provided by Aarhus Vand, looks into what kind of knowledge is available regarding the CSO structures. The study found that in only 22 % of the CSO structures, sufficient information about the structure was available so that the structure could be characterised based on its geometry. The CSO structures of these 22 % (67 structures) were then classified based on the geometry of the structure in the following categories [Murula et al., 2018]:

- Weir based structures
- Well based structures
- Pipe diversion based structures
- Special structures, that do not fit in any of the above

Table 1.1. Distribution of the 67 structures from Aarhus [Murula et al., 2018].

CSO structure category	Percentage
Weir based	48%
Well based	18%
Pipe diversion based	20%
Special	14%

From table 1.1, it is evident that weir-based structures are the most prevalent type of CSO structure. It is suspected that weir-based structures also contribute to a greater discharge compared to other

structures. This is due to the fact that overflow weirs are usually constructed in locations requiring high discharge capacities. Within the category of weir-based structures, two main types can be identified: stilling pond CSO structures and side weir CSO structures [Guo, 2011].

Stilling Pond CSO Structures

In the stilling pond chamber, the water enters and leaves the chamber in opposite ends. The weir is located opposite the inlet, above the outlet pipe [Guo, 2011]. The advantage of the stilling pond is that particles typically have time to settle in the chamber and leave through the outlet pipe rather than being discharged over the weir. The chamber thereby works as a simple treatment of the waste water, and often provides a more efficient separation of suspended solids than the side weir CSO structure [Dufresne et al., 2009].

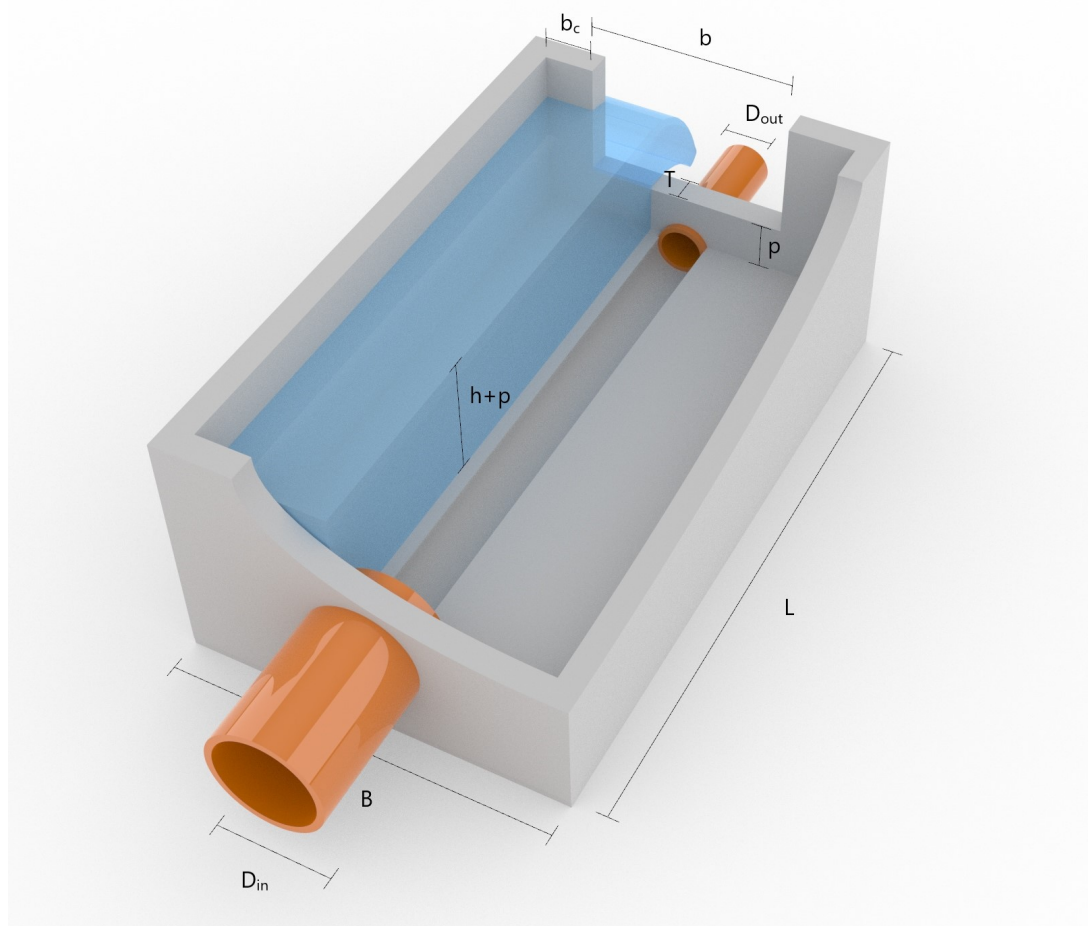


Figure 1.2. Illustration of stilling pond CSO chamber with important geometrical dimensions.

In the stilling pond the water enters the chamber perpendicular to the weir edge. This means that

the velocity head directly results in a larger energy head over the weir. Due to this the weir coefficient for stilling ponds is typically larger than it is for side weirs [Bagheri et al., 2014].

One of the disadvantages of the stilling pond is that the chamber width determines the weir length. Therefore, to ensure an appropriate discharge capacity, the chamber often has to be quite wide. The chamber, however, also must have a certain length as the particles must have time to settle. Therefore, stilling pond chambers often have compact structures - especially when large discharge capacities are desired. The placement of stilling pond CSO chambers might lead to implications when constructed close to roads [Balmforth, 2009].

Side Weir CSO Structures

As opposed to the stilling pond CSO chamber, the water enters the side weir CSO chamber parallel to the weir. It therefore has little to no energy in the direction of the spill flow. This is one of the reasons that the weir coefficient for side weir CSO chambers in general is lower than that of the stilling pond CSO structures [Hager, 1987]. The side weir CSO structure is often found to have a slimmer design than the stilling pond, and in fact the width of the chamber is often seen to approximately match the diameter of the inlet pipe. Side weir CSO structures exist both as one sided and as double sided weirs with weirs on both sides of the chamber. The double sided weir is more complicated to build. However, it essentially doubles the capacity of the CSO chamber, thereby reducing the necessary size of the chamber [WaPUG, 2006]. In the following, one-sided weirs will be in focus, as it is the reckoned to be the most common. A single sided side weir CSO chamber has been illustrated in figure 1.3.

In the side weir CSO chamber, the flow in the main channel decreases gradually due to the flow over the weir. Therefore, the water level is also changing along the weir and so is the discharge over the weir. This makes it more problematic to relate the water level at a single location to the flow over the whole weir. Compared to the stilling pond CSO chamber, the determination of the rating curve is reckoned to be more challenging for side weirs [Di Bacco and Scorzini, 2019]. If the flow in the channel is subcritical, the water level is increasing along the weir length, and if the water level is supercritical, the water level is decreasing along the weir [Balmforth, 2009].

Side weir CSO chambers are sometimes divided into two types: high side weirs and low side weirs. The type depends on the characteristics of the flow and not solely on the geometry. The same side

weir can therefore under some conditions function as a low side weir and in other conditions function as a high side weir [Balmforth, 2009].

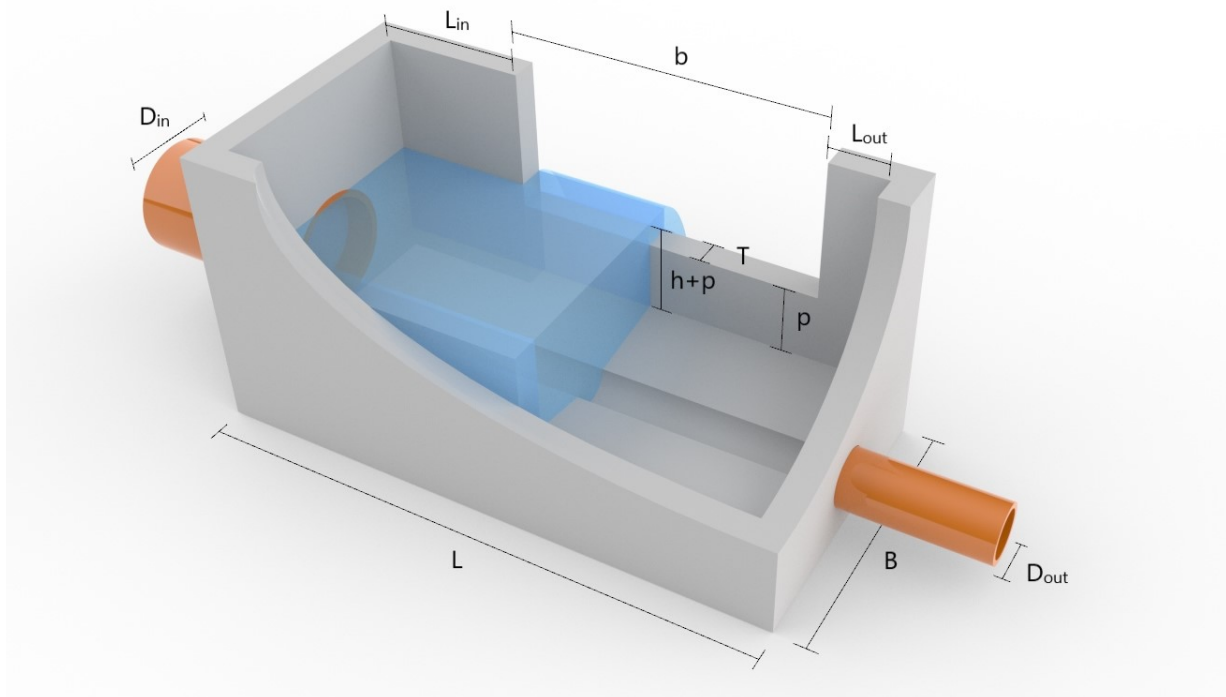


Figure 1.3. Illustration of side weir CSO chamber with important geometrical dimensions.

When it comes to low side weirs, the weir ensures a quite low water level in the chamber. The low water level will increase the possibility for a hydraulic jump to form if e.g. the upstream sewer is very steep. However, a hydraulic jump can also occur in low side weirs without the flow on the upstream sewer being supercritical. In cases of large inflow, the low side weir leads to a rapid draw down of the water level, forcing supercritical flow to emerge with a hydraulic jump to follow. The hydraulic jump gives a large and somewhat unpredictable rise in the water level, and whether or not this jump happens before, after or along the weir, it significantly affects the weir overflow [WaPUG, 2006].

As a rule of thumb, low side weirs typically have a crest level below the centerline of the incoming sewer, and the total energy head at the inlet is larger than twice the weir height [Balmforth, 2009].

In cases of a high side weir, the water level is too large for supercritical flow to emerge. According to WaPUG [2006] side weir CSO chambers should in general be designed with the goal of achieving subcritical flow conditions. However, it is suspected that considerations like this haven't been taken into account for the majority of the existing CSO chambers of today.

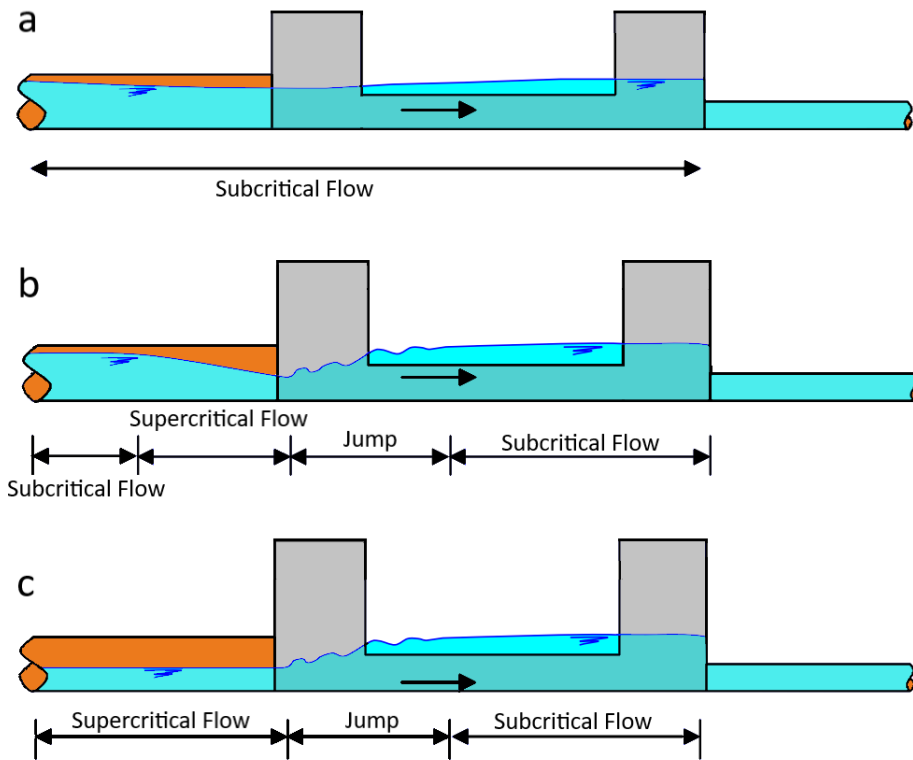


Figure 1.4. Illustration of the three different flowregimes within a side weir CSO chamber. High side weir with subcritical flow (a), low side weir with draw down forming a hydraulic jump (b), supercritical flow conditions in inlet pipe (c). Modified figure after [WaPUG, 2006].

Problem Statement 2

The objective of this master project is to develop methods to predict CSO rating curves without the need for computationally demeaning CFD simulations. The following problem statement has been defined on the basis of this goal:

Can CFD modelling accurately determine Combined Sewer Overflow (CSO) rating curves, and is it possible to derive predictive trends for rating curves solely based on the geometric characteristics of the CSO chamber?

To answer the problem statement, a number of work questions have been defined:

- What determines the flow over a weir and the discharge from a CSO structure?
- What types of CSO structures exist, and is it possible to characterize them?
- How can computational fluid dynamics (CFD) be used to determine rating curves for CSO structures?
- How can the rating curve be predicted based on the geometric characteristics of the chamber without the need for CFD?
- How do screens and discharge pipes affect the rating curve, and what adjustments can be made to incorporate these effects?

To answer the problem statement, different approaches will be used. Both the use of scale models and CFD modelling. The two approaches will assist each other. By using scale models to validate the CFD models, it becomes possible to modify design parameters in the CFD models convinced that the obtained results accurately represent reality.

Artificial CSO structures will be generated and analysed to examine potential correlations between the weir coefficient and geometric lengths or other coefficients influencing the rating curve and the characteristics of the CSO structures.

The effect of the discharge pipe and the presence of a screen will be investigated, and approaches for how to implement the effect of those within the rating curve will be developed.

The accuracy of the predicted rating curves will be assessed through a comparative analysis. The predicted rating curves will be compared to rating curves derived from CFD modeling of actual CSO structures, obtained from three different Danish water companies. Additionally, the predicted rating curves will be compared to real-life measurements collected from the CSO structures.

The Weir Equation 3

The weir equation originates from the work of Poleni [1717], and states that the flow over the weir is proportional to the water head above the weir raised to a power of 1.5. The equation is based on Bernoulli's equation and the continuity equation and has been derived in appendix B.

$$Q = C \cdot B \cdot \sqrt{2 \cdot g} \cdot h^{1.5} \quad (3.1)$$

Where Q is the weir flow ($\text{m}^3 \cdot \text{s}^{-1}$), C is the weir coefficient (-), B is the width of the weir (m), g is the gravitational acceleration ($\text{m} \cdot \text{s}^{-2}$) and h is the water level above the weir crest (m). The weir coefficient is not an universal constant, and depends on the geometry and the roughness of the weir as well as the upstream flow conditions and pressure distribution [Chanson, 2004]. Traditionally weirs are classified into two categories depending on their geometry; sharp crested and broad crested weirs. However, types such as ogee or crump shaped weirs also exist. The different types have been shown in figure 3.1.

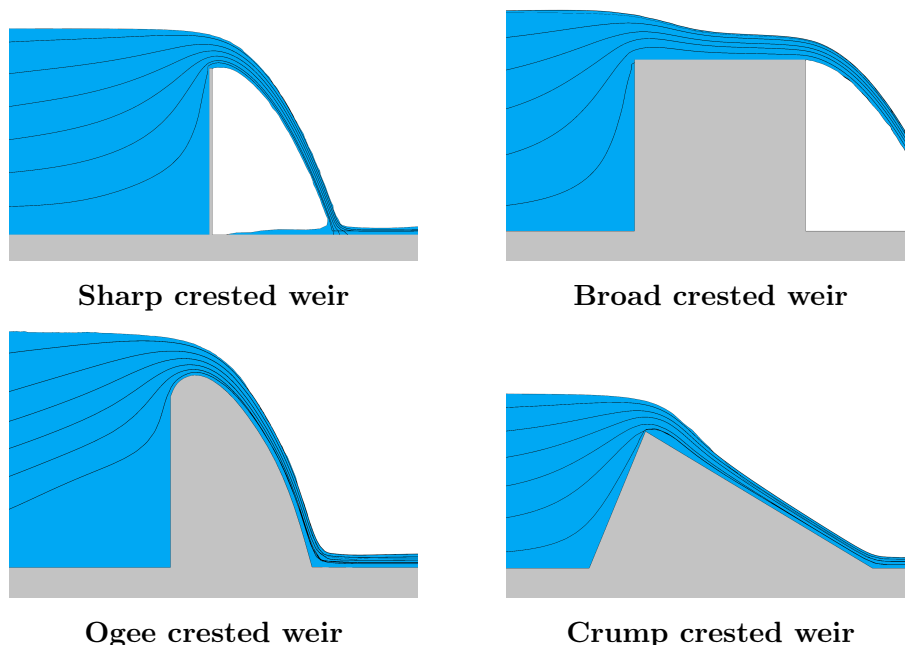


Figure 3.1. Different types of weir geometry. The slopes of the crump crested weir are not to scale.

Ogee and crump shaped weirs often have strictly defined geometries and are typically used in regard to dams and open channels respectively [Chanson, 2004], [Al-Khateeb et al., 2019], and are therefore suspected to be rare in sewer systems.

Assuming an either sharp or broad crested weir, the use of dimensional analysis can narrow down the number of variables suspected to influence the weir coefficient. Furthermore, with the use of dimensional analysis, it is possible to define the weir coefficient based on dimensionless parameters, meaning that a relationship should be independent of the size of a given CSO structure.

For the stilling pond CSO structure, the following geometrical dimensions and physical quantities are expected to have an effect on the weir coefficient:

$$Q = f (h, v, \rho, \gamma, \mu, \sigma, B, T, p, D_{in}, D_{out}, b, v_1) \quad (3.2)$$

Where Q is the weir flow ($\text{m}^3 \cdot \text{s}^{-1}$), h is the water level above the weir crest (m), v is the velocity above the weir ($\text{m} \cdot \text{s}^{-1}$), ρ is the density of water ($\text{kg} \cdot \text{m}^{-3}$), γ is the specific weight of water ($\text{kg} \cdot \text{s}^{-2} \cdot \text{m}^{-2}$), μ is the kinematic viscosity of water ($\text{kg} \cdot \text{s}^{-1} \cdot \text{m}^{-1}$), σ is the surface tension of water ($\text{m} \cdot \text{s}^{-2}$), B is the width of the channel (m), T is the thickness of the weir (m), p is the height of the crest (m), D_{in} and D_{out} is the diameter of the inlet and outlet pipe respectively (m), b is the length of the weir (m) and v_1 is the upstream main channel flow velocity ($\text{m} \cdot \text{s}^{-1}$). f is symbol for an arbitrary unknown function. All of the geometrical dimensions has been shown in figure 1.2. Using h , v and ρ as repeating variables and doing some rearranging we can get the following dimensionless parameters shown in equation 3.3. The derivation has been shown in appendix A.

$$C = f (Fr, Re, We, \frac{B}{h}, \frac{h}{T}, \frac{h}{p}, \frac{L}{B}, \frac{D_{in}}{B}, \frac{D_{out}}{B}, \frac{b}{B}) \quad (3.3)$$

Where Fr is the Froude number in the channel, Re is Reynolds number and We is the Weber number. The results are similar to what is proposed by [Tracy, 1957]. However, Tracy [1957] bases his analysis on an ideal weir, and therefore further reasons that the Froude number is without influence, as the governing parameters h and v cannot be varied independently. However, this assumption does not hold true for CSO structures due to the flow through the outlet pipe.

For side weirs CSO structures two velocities have to be included, as the velocity is not constant along the length of weir. Furthermore lengths of the channel up- and downstream the weir have also been

included (L_{in} and L_{out}). An elaboration on the dimensional analysis has been given in appendix A, and the result has been shown in equation 3.4. The geometrical dimensions has been illustrated in figure 1.3.

$$C = f \left(Fr, Re, We, \frac{B}{h}, \frac{h}{T}, \frac{h}{p}, \frac{D_{in}}{B}, \frac{D_{out}}{B}, \frac{b}{B}, \frac{L_{in}}{h}, \frac{L_{out}}{h}, \frac{v_{in}}{v_{out}} \right) \quad (3.4)$$

Typically surface tension effects are insignificant when having to do with lengths above 3 cm [Bagheri et al., 2014], and the Weber number can therefore be neglected. The Reynolds number can also be neglected as long as we are in highly turbulent regimes, which is almost always the case in real life sewer systems [Winther et al., 2016].

For some idealised conditions, the weir coefficient can be determined theoretically. This is the case for broad crested weirs where the crest is broad enough for hydrostatic pressure distribution to develop on the crest top resulting in critical flow conditions [Chanson, 2004].

For sharp crested weirs, the curvature of the water surface is too large for hydrostatic pressure to be present at the weir crest. Therefore, the weir coefficient of the broad crested weir isn't valid. The discharge over sharp weirs is however well studied, and the weir coefficient can be estimated using equation 3.5.

For many CSO structures, the weir is suspected to be neither broad-crested nor sharp-crested, but rather something in between. The crests are often constructed using materials like concrete or wood, and do not always consist of a sharp metal plate. As a result, the weir coefficient for these intermediate weirs differs from both sharp-crested and broad-crested weirs. Lots of research has been conducted developing empirical equations for such weirs. Azimi and Rajaratnam [2009] divided the types of weirs into four categories; sharp-crested, short-crested, broad-crested, and long-crested weirs, based on the ratio of water level to weir thickness. The empirical equations for these different types of weirs are provided in table 3.1.

Table 3.1. Empirical equations estimating the weir coefficient as a function of the water level (h), the weir height (p) and the thickness of the crest (h) [Azimi and Rajaratnam, 2009].

Name	Regime	Weir Coefficient	
Sharp Crest	$\frac{h}{T} > 2$	$0.41 + 0.053 \cdot \frac{h}{p}$	(3.5)
Short Crest	$0.4 < \frac{h}{T} < 2$	$0.511 + 0.143 \cdot \frac{h}{T}$	(3.6)
Broad Crest	$0.1 < \frac{h}{T} < 0.4$	$0.582 \cdot \left(\frac{h}{h+p}\right)^2 - 0.2 \cdot \left(\frac{h}{h+p}\right) + 0.585$	(3.7)
Long Crest	$\frac{h}{T} < 0.1$	$0.68 \cdot \left(\frac{h}{h+p}\right)^{0.12}$	(3.8)

The different types of weirs have been illustrated in figure 3.2.

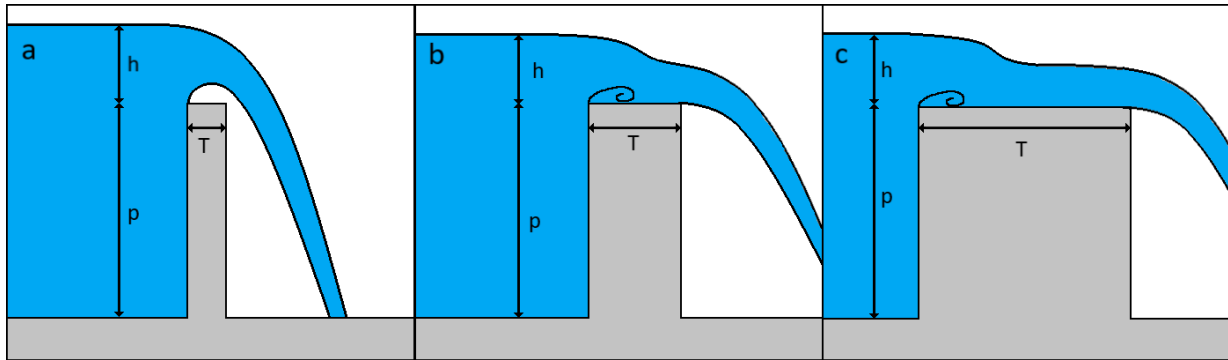


Figure 3.2. Illustration of the different types of weirs. Sharp-crested weir (a), Short-crested weir (b), Broad/Long crested weir (c).

As it can be seen from table 3.1, the weir coefficient depends on 2 dimensionless quantities (h/T and h/p). These equations are however based on an idealised channel with no contraction. As shown in appendix A, these are exactly the two parameters predicted to govern the weir coefficient for an idealised channel.

The equations above have all been based on ideal conditions, where the assumptions of the weir equation are fulfilled, e.g. the assumption of a single water level or water velocity. In CSO structures, the conditions however do not always allow for these requirements to be met. In CSO chambers, the inlet and outlet length is typically too short for a fully developed flow to emerge. Furthermore, the water level is not constant, instead it slightly varies throughout the chamber due to turbulence, drawdown of water by the weir or build up of water against a wall. This is especially the case in side weir CSO chambers, where the nature of the structure creates either a build up or a draw down of water in the main channel along the weir [Hager, 1987].

For side weirs, different approaches exist compensating for the non uniform water level. Either the weir coefficient can be adjusted, or the water level inserted in the weir equation can be substituted with a predicted water surface profile. For side weirs, the latter often results in some form of interpolation of the water level between the start and the end of the weir. Different approaches exist such as Domínguez's approach, where a linear water level between the upstream and downstream weir edges is assumed [Domínguez, 1935], or Schmidt's approach which uses an average between the upstream and downstream water level [Schmidt, 1954]. The most recognized approach is probably De Marchi's theory [WaPUG, 2006]. De Marchi's theory is an analytical solution to the energy equation in the main channel assuming constant energy but a gradual reduction in the flow as the water leaves

the channel over the weir. This results in a prediction of the water level along the weir [Di Bacco and Scorzini, 2019]. The theory is however based on only 1 dimension, and it might therefore not be completely representative for a side weir, where the discharge is also expected to be influenced by the width of the channel. When using De Marchi's theory, the weir coefficient is often denoted C_M .

All of the methods above share the requirement of a water level measurement at each end of the weir. We typically only want to measure the water level at one location in order to hold down costs. However, regardless of whether a single water level measurement or an interpolated water surface profile is used, some deviation from the true water level is unavoidable.

Therefore, based on research of side weirs, [Di Bacco and Scorzini, 2019] proposed, that the used weir coefficient can be seen as a combination of a parameter that compensates for the off water surface profile and a true drag coefficient over the weir, as shown in equation 3.9.

$$C = C_m \cdot C_i \quad (3.9)$$

Where C_i is the ideal weir coefficient over the weir, and C_m is a coefficient that compensates for off water surface profile used, called the model coefficient [Di Bacco and Scorzini, 2019]. This realisation is however not always present when assessing the literature. Therefore, confusion often arises, as it often isn't totally clear what water level profile the weir coefficient is based upon. It can therefore be difficult to directly compare results from different sources [Di Bacco and Scorzini, 2019].

Nappe aeration

The equations of table 3.1 are only valid when the nappe is fully aerated, meaning that the weir is flowing free. The nappe is the sheet of water flowing over the weir. Depending on the geometry of the weir, air can have difficulties entering the underside of the nappe. When this is the case, the pressure below the nappe becomes less than atmospheric, and the nappe is said to be depressed. The flow of a depressed nappe is typically slightly larger than the flow of an aerated nappe. If no air is present below the weir, the nappe is said to be clinging. Clinging nappes typically can have a flowrate up to 25 % larger than the free nappe [Openchannelflow, 2023]. The effect of lacking ventiation of the nappe has been illustrated in figure 3.3.

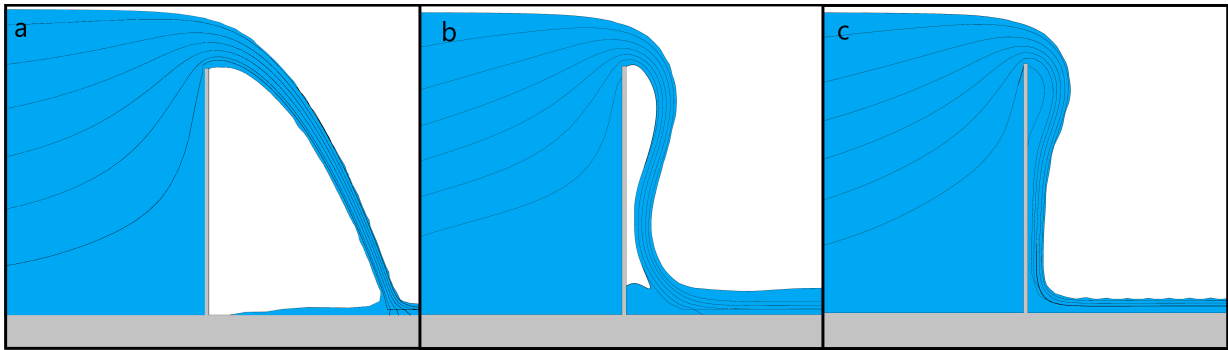


Figure 3.3. Illustration of the effect of lacking ventilation of the nappe. a: a fully ventilated nappe, b: a depressed nappe, c a clinging nappe

The ventilation of a weir can be facilitated using different approaches. However, a side contraction of the weir is typically enough to ensure a full aerated nappe at feasible flowrates. For a contracted weir, the streamlines will converge upstream the weir. This leads to a slightly lowered discharge, which traditionally is handled by reducing the effective weir length by one fifth of the water height [Francis, 1883]:

$$Q = C \cdot (b - 0.2 \cdot h) \cdot \sqrt{2 \cdot g} \cdot h^{1.5} \quad (3.10)$$

The C can be assumed constant as long as the head does not increase to more than $1/3$ of the weir length [United States Department of the Interior Bureau of Reclamation, 2001].



Figure 4.2. A photo of the weir placed in the channel.

The water level has been measured using a ruler located 0,7 m upstream the weir. The flow has been measured 3,5 meters upstream the weir using a OTT C2 current meter. The measurements has been carried out in 4 depths and in 5 positions along the cross section for 50 seconds, and the measured speed of rotation has been converted to a velocity using the attached conversion formula shown in equation 4.1.

$$v = 0.0632 \cdot n + 0.017 \quad (4.1)$$

Where v is the velocity ($\text{m} \cdot \text{s}^{-1}$) and n is number of rotations per second.

Due to the current meter being unable to measure velocities below $0.025 \text{ m} \cdot \text{s}^{-1}$, for a few cases the flow upstream the weir where too low for the flow to be measured. In these cases the flow were instead measured downstream the weir, where the water level is much lower. The flow is however very turbulent, and the water level not nearly as steady as upstream the weir. Under these conditions the water level were only measured in one depth and in 10 positions along the cross section. To try to compensate for the increased uncertainty, the flow has been measured in two locations, 1.2 and 1.6 meters downstream the weir respectively. A picture at the flow measurement setup has been shown in figure 4.3.

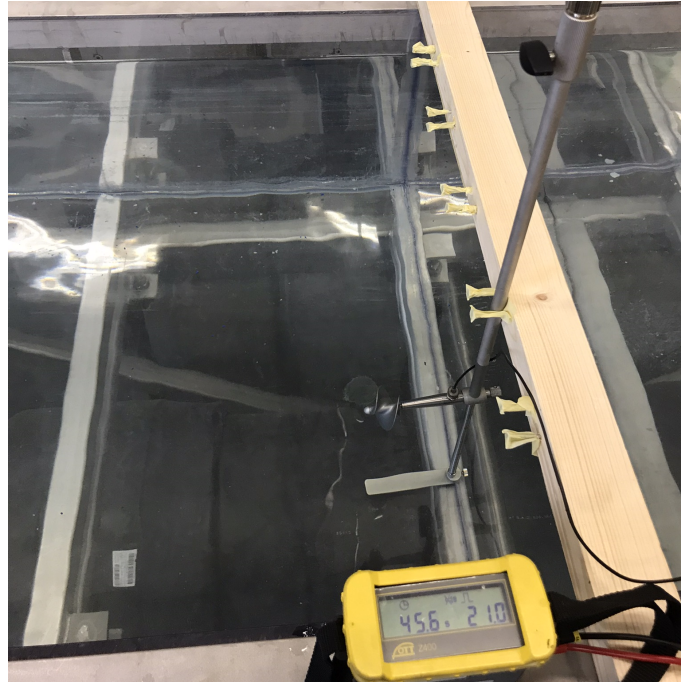


Figure 4.3. A picture of the setup used for flow measurements.

The velocity has been converted into a flow by interpolating between the positions of measurement and by integration over the cross sectional area of the channel. The current meter doesn't allow for measurements closer than 3 centimeters to the button or the edges. Therefore the velocity-profile close to the walls has not been determined. Instead the velocity is assumed equal to the nearest measurement, until a distance of 1 cm from the wall from within the velocity is assumed to decrease linearly having a velocity of 0 at the wall surface.

Inserting the flow and the water head above the weir in eq.3.1, the weir coefficient has been calculated. This has been done for 3 different flowrates. It has also been done for the same flowrate 3 times, to get an idea of the variability of the results.

4.2 Experimental Setup - Screens

To evaluate the impact of a screen on the rating curve of a weir, a screen has been attached to the sharp crested weir shown in figure 4.2. The screen consists of a perforated steel sheet with a grid size of 6x3.5 mm. The screen has been shown in figure 4.4.

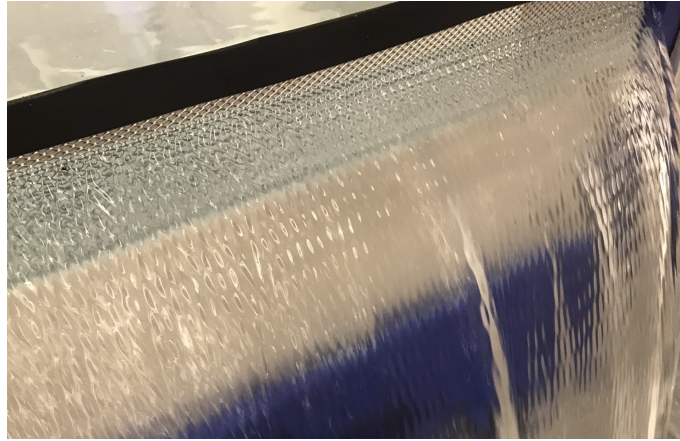


Figure 4.4. Photo of the flow through the screen.

The weir coefficient has been determined the same way as described in section 4.1. Due to the quite small grid size, adjustments has to be made to compensate for surface tension effects. The grid size of real life screens is typically too large for surface tension to have significant effect, and any the effect of such on the results are therefore undesirable. An elaboration of this has been given in appendix C.

To asses the increased resistance of the screen as it clogs, the screen has been covered with small pieces of duct tape (1-2 cm x 1-2 cm) to artificially simulate clogging. 5 different degrees of clogging have been simulated by removing 1/5 of the tape between experiments. The degree of clogging has been estimated with the use of image analysis as illustrated in figure 4.5.

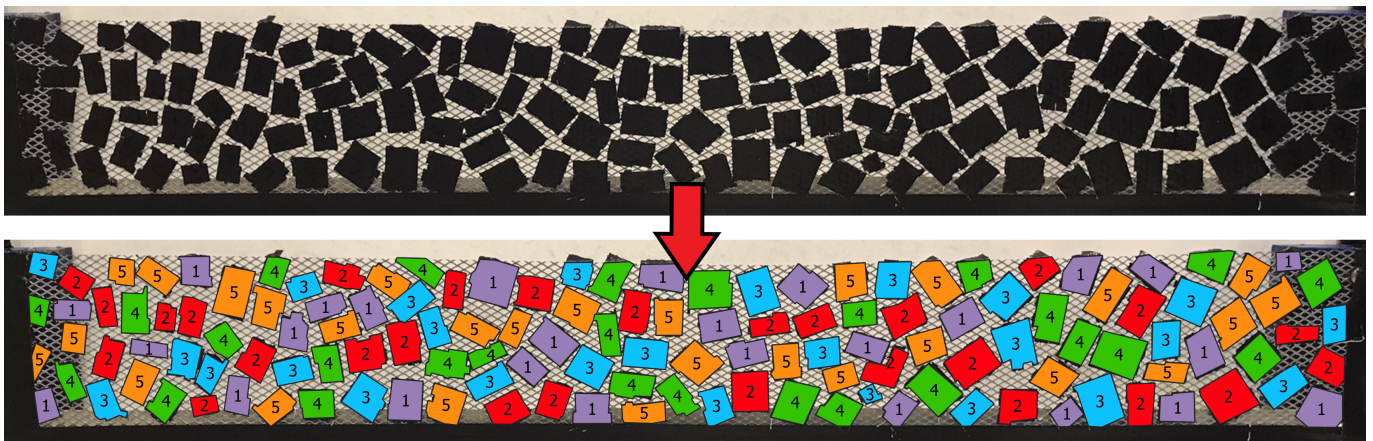


Figure 4.5. Illustration of image analysis of clogged screen. The numbers represent the sequence at witch the tape were removed to simulate different degress of clogging.

As the duct tape were put on at random, there is no grantee for an even vertical distribution. Therefore the distribution has been determined for each of the 5 degrees of clogging, and has been shown in figure 4.6.

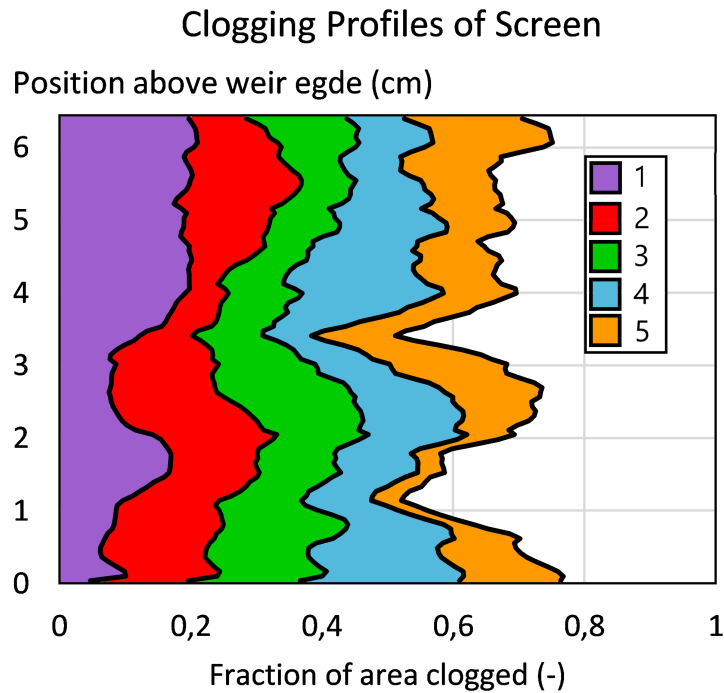


Figure 4.6. The vertical clogging profile, for the 5 different degrees of clogging. The numbers represent the tape numbers of figure 4.5.

The actual clogging fraction as well as the weighted clogging fraction has been shown in table 4.1. The weighted clogging fraction compensates for the hydrostatic pressure distribution, making a clogging in the bottom have larger effect than one at the top.

Table 4.1. The estimated fraction of the screen covered by tape.

Tape numbers	Actual clogged fraction	Weighted clogged fraction
1	0,14	0,13
1+2	0,28	0,27
1+2+3	0,40	0,40
1+2+3+4	0,55	0,55
1+2+3+4+5	0,66	0,65

As it can be seen no significant error would be introduced using the actual clogged fraction, indicating that the clogging are approximately evenly vertically distributed.

The weir coefficient has been determined for the 5 different degrees of clogging. Furthermore the weir coefficient of the clean screen has been determined for 4 different flow rates.

Computational Fluid Dynamics

5

Computational Fluid Dynamics (CFD) is the simulation of fluid motion in and around solid objects. CFD models finds use in a wide range of applications, and has traditionally been widely used in the space, aerospace and automobile industry. The introduction of multiphase modelling has enabled the modelling of free-surface flows, opening up the possibility for the use of CFD modelling in a wide variety of fields, among other the simulation of flows within CSO structures. Serval software programs are available for CFD modelling, and in this project the Simcenter STAR-CCM+ is used. Simcenter STAR-CCM+ is a commercial software by Siemens.

It is not the intention for this report to give an in-depth description of the workings and mathematics of a CFD model, therefore only a brief description of the basics of a mulitphase CFD model has been given. For an in depth description the reader is referred to the STAR CCM+ manual by [Siemens Industry Software, 2020].

CFD relies on the numerical solution of the Navier-Stokes equation and the continuity equation in 3 dimensions. The Navier-Stokes equation has been shown in equation 5.1.

$$\rho \frac{Dv}{Dt} = -\nabla P + \rho g + \mu \nabla^2 v \quad (5.1)$$

Where ρ is the density of the fluid ($\text{kg} \cdot \text{m}^{-3}$), v is the flow velocity ($\text{m} \cdot \text{s}^{-1}$), P is the pressure (Pa), g is the gravitational acceleration ($\text{m} \cdot \text{s}^{-2}$) and μ is the kinematic viscosity ($\text{kg} \cdot \text{s}^{-1} \cdot \text{m}^{-1}$)

$\frac{Dv}{Dt}$ is the material derivative of the flow velocity, ∇P describes the pressure gradient, ρg describes the gravitational force, and $\mu \nabla^2 v$ describes the dispersion of the velocity due to viscous forces. The continuity equation has been presented in equation 5.2.

$$\nabla v = 0 \quad (5.2)$$

The continuity equation states that mass can neither be created or destroyed. Here it assumes the modelled fluid to be incompressible, which is reasonable for water, when considering free surface flows as is the case for this project.

As the equations are solved numerically they rely on a discretisation of the domain in space. Typically the fluid domain is discretized into finite volumes, and the equations are solved using the finite volume method, however other methods such as the finite element method are also used. Star-CCM+ relies on the finite volume method. The discretization of the domain in space is called meshing and is a central part of CFD modelling. Different types of meshing exist subdividing the domain into cells based on triangles, squares or polygons. Creating a mesh consisting of squares is called trimmed meshing, and has been the meshing type used in this project. The trimmed mesh has the advantage, that is is good at modelling right angles, which is often seen within CSO chambers. Furthermore, a trimmed mesh is good at modelling plane surfaces, which is important when modelling of free water surfaces, as they are typically plane. A trimmed mesh generated for a simple CSO structure has been shown in figure 5.1:

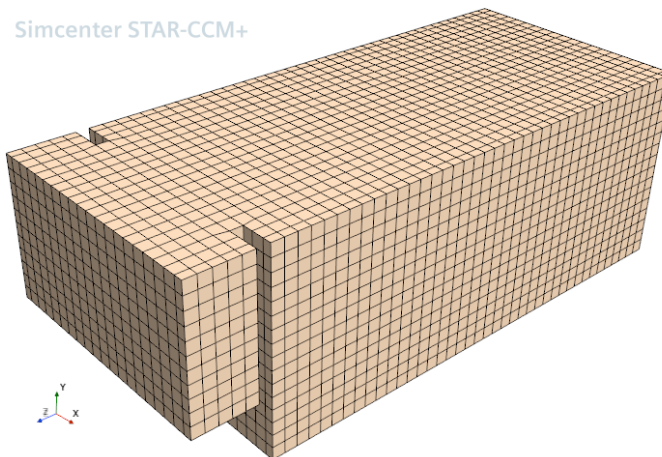


Figure 5.1. The geometry of a simple contracted weir with a trimmed mesh.

If the goal of the model is a transient solution, the domain also has to be discretized in time. Different numerical schemes exist to approximate the solution within each finite volume at each timestep. In this model, an implicit scheme is used due to its ability to provide a stable solution disregarded the timestep used. When dealing with multiphase problems stationary solvers are often inadequate, as pressure differences only propagate slowly through the domain, making it hard for stationary solvers to converge.

Due to the discretisation of the domain in space, the model cannot describe the turbulence that happens on a scale smaller than the discretisation. To compensate for this a turbulence model has to be included. A variety of different turbulence models exist, many of which are based of the Reynolds averaged naiver stokes equations. A $k-\epsilon$ turbulence model has been chosen as it is a widely used

turbulence model. Here the viscosity is substitute for an eddy viscosity. The eddy viscosity is then estimated based on a modelled turbulent kinetic energy and a rate at which the turbulent kinetic dissipates. The introduction of a turbulence model did however not change the solution significantly compared to a laminar model. As the $k-\epsilon$ turbulence model is a fairly simple model, it doesn't increase the calculation time unreasonably, and it has therefore been the model of choice.

To model two different phases being air and water, a multiphase model is included. The volume of fluid (VOF) technique is well-suited for modeling of multiphase systems with well defined interfaces, which typically is the case within sewer systems. In the VOF model, the fluid is considered as a continuous medium, and the volume fraction of each fluid is tracked based on the calculated velocity field and mass conservation. The VOF model assigns each phase with a value between 1 and 0, depending on whether the phase is water or air. The phase interface (being the water surface) then equals the location where the volume fraction of water is 0.5. Using a sufficient mesh resolution and timestep the surface can be tracked throughout the simulation. It is important to ensure a small enough timestep, as high Courant numbers will lead to a dispersion of the water surface.

The definition of the water surface using the VOF method enables the possibility for the use of adaptive mesh refinement. Adaptive mesh refinement increases the spacial resolution close to the water surface, allowing for precise and accurate tracking of the surface. The mesh has been shown using adaptive mesh refinement in figure 5.2.

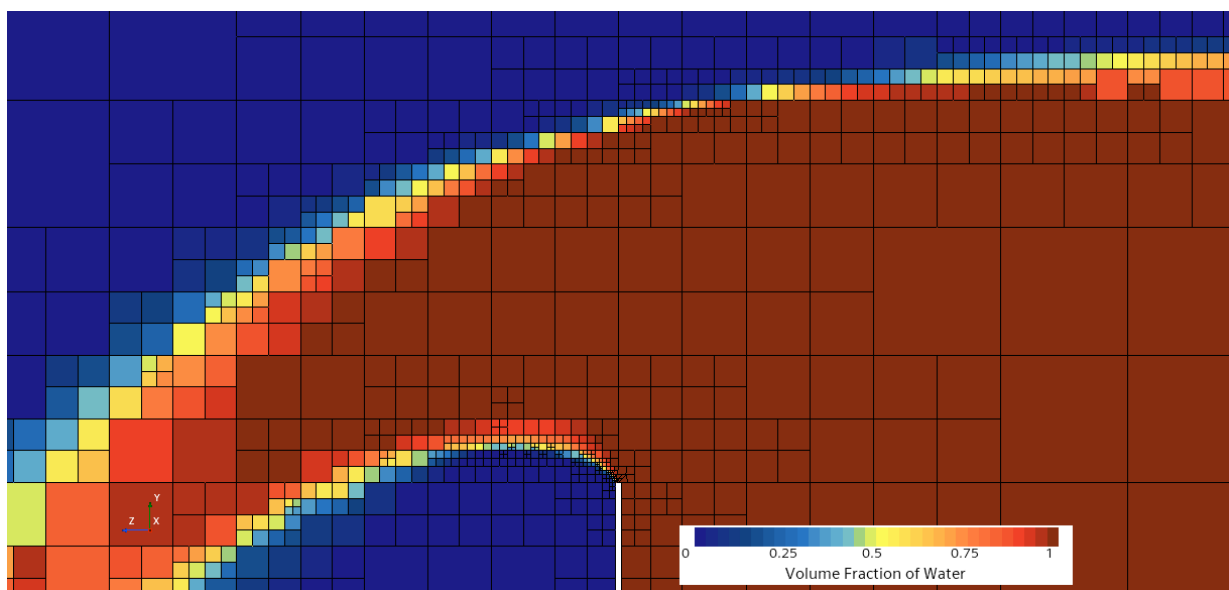


Figure 5.2. Illustration of the mesh at quasi steady state for the modelling of a sharp crested weir. It can be seen that the timestep is too large of the nappe to stay well defined downstream the weir. This however has no effect on the flow over the weir, as it happens after the flow has become supercritical.

5.1 CFD Model - Sharp Crested Weir

The sharp crested weir from the channel has been modelled in Star CCM+. The geometry of the weir as well as the chosen boundary conditions has been shown below:

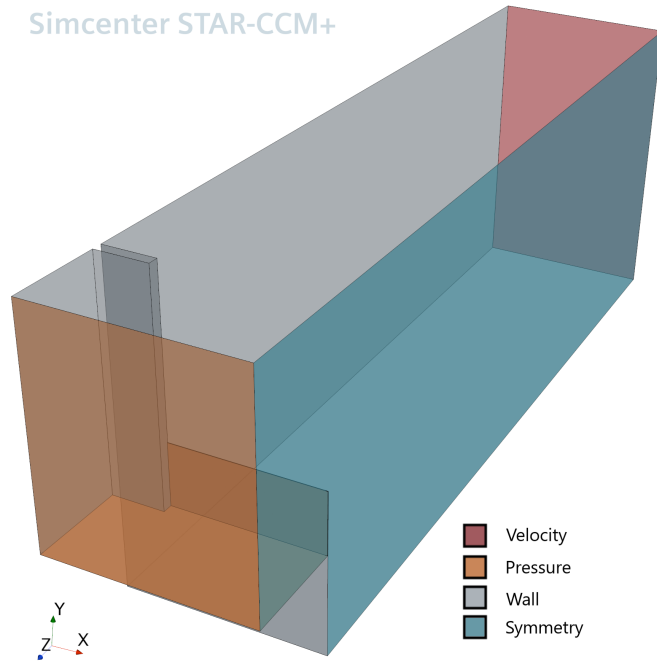


Figure 5.3. The geometry of the CFD model, with colors representing the chosen boundary condition. Only half the channel has been shown, as the other half has been modelled using the symmetry plane. The top of the geometry has not been shown, however, it has been modelled as a pressure boundary as well.

The inlet boundary conditions has been applied with a uniform velocity inlet, assuming ideal fully developed flow conditions. The height of the inflow boundary has been made variable, adjusting itself to match the water level in the chamber, ensuring a perfect uniform inflow.

Downstream the weir a pressure boundary has been chosen with a pressure of 0 Pa. This allows for the water to leave the model after it has passed the weir. The top of the domain has likewise been modelled as a pressure boundary with an air phase having a pressure of 0 Pa. As the domain is symmetric and the simulation is conducted at relative high Reynolds numbers, no asymmetric solutions are expected, and a symmetry plane has been introduced to decrease the computational time.

The domain have been discretized using a trimmed mesh. A base mesh size of 2 cm has been used in

combination with adaptive mesh refinement. A max refinement level of 3 has been chosen allowing for a mesh size of 0.25 cm at the water-air interface. Furthermore the weir edge has been applied as a surface control ensuring a base mesh size of 0.2 cm, which in combination with the adaptive mesh refinement allows for a reasonable discretization of the weir edge.

The model has been simulated using an implicit numerical scheme with a timestep of 0.01 seconds. the simulation has been conducted until quasi-stationary conditions are observed, with the chosen initial condition this happened after around 30 seconds of simulated time.

5.2 CFD Model - Ideal Channel

A weir without any side contraction has been modelled to allow for comparison between the CFD results and the values predicted by the literature formulas presented in table 3.1. The same model has been used as in the model of the sharp crested weir of section 5.1. However the geometry has been altered as shown in figure 5.4.

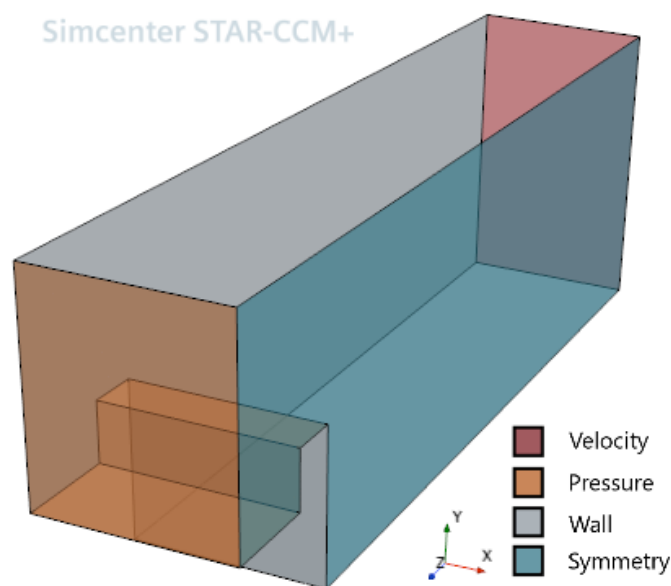


Figure 5.4. The geometry of the CFD model, with colors representing the chosen boundary condition. Only half the channel has been shown, as the other half has been modelled using the symmetry plane. The top of the geometry has not been shown, however, it has been modelled as a pressure boundary as well.

The flow and the thickness of the weir has systematically been altered to obtain the weir coefficient for a range of h/p -ratios and h/T -ratios. 8 different weir thicknesses has been modelled at 6 different flow rates giving a total of 48 simulations. The simulated values has been shown in table 5.1.

Table 5.1

Parameter	Values
T (cm)	0.1, 0.3, 0.9, 1.9, 3.3, 5.1, 7.3, 9.9
Q (L/s)	20, 60, 100, 140, 180, 220

5.3 CFD Model - Stilling Pond CSO Chamber

A simple geometry has been build to simulate the flow within a stilling pond CSO chamber, the defined geometry is similar to the geometry illustrated in figure 1.2. The dimensions of the chamber has been randomly varied. 221 CSO structures has been randomly generated within the following ranges for geometrical lengths as well as flow velocities. In case the outflow surpassed the inflow, the generated structure has been discarded.

Table 5.2. The geometrical parameters is refereeing to figure 1.2.

	lower limit	upper limit	Unit
D_{in}	0,12	0,96	m
D_{out}	0,04	0,56	m
L	0,96	6,72	m
B	0,64	4,8	m
p	0,16	1,84	m
v_{in}	0	4	m/s
v_{out}	0	3	m/s

A constant crest length of 4 cm has been used instead of a traditional sharp crested weir. This has been chosen due to the recognition that weirs in real word CSO structures often aren't equipped with an ideal sharp-crested weir. The weir has been modelled as a contracted weir to ensure proper ventilation of the nappe, this has further been ensured by the induction of a pressure boundary on the downstream side of the weir. The side contractions have been set to a constant length of 16 cm each.

The inlet and outlet has been modelled as velocity outlets. In case only part of the inlet is submerged by water, the part above the water is converted to a no-flow boundary. downstream the weir, a pressure boundary with a constant pressure of atmospheric pressure has been applied. The walls has been modelled as hydraulic smooth surfaces, as the effect of the roughness according to [Fach et al., 2008] has been found to be negligible. The chosen boundary conditions have been illustrated in figure 5.5.

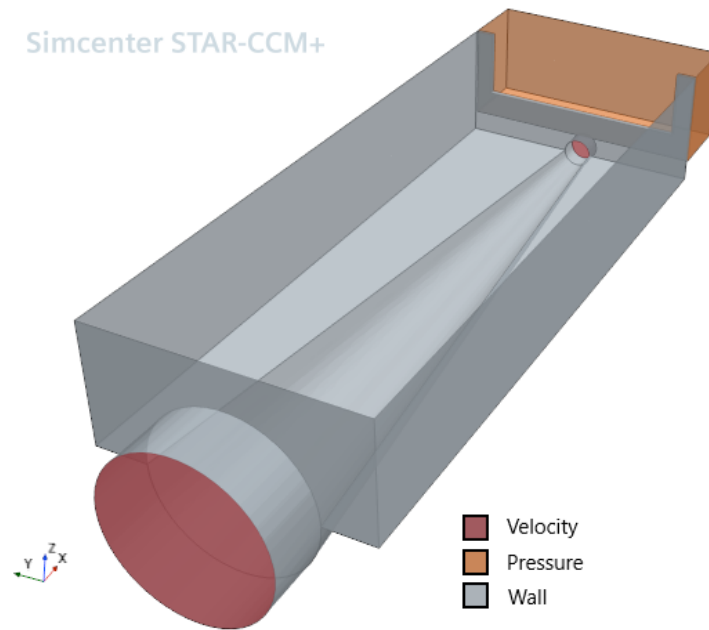


Figure 5.5. Illustration of the boundary conditions chosen. The top of the geometry has not been visualised not to block the backend of the domain. It however has also been modelled as a pressure boundary.

The mesh has been generated using a trimmed mesh with a base size of 16 cm. To archive a sufficient resolution of the pipes and the dry flow channel, surface controls have been applied to the curving surfaces, ensuring a mesh size of 4 cm at the surface. Likewise have surface controls been allied to the weir edge, to ensure a proper resolution of the nappe. Furthermore to ensure a sharp interface between the water and the air phase, adaptive mesh refinement has been applied. The adaptive mesh refinement refines the mesh up till a minimal mesh size of 2 cm (equivalent to a 3 level refinement), with a transition width of 2 layers. A timestep of 0.05 s has been used.

To extract the water surface level throughout the domain, an isosurface defined as the plane where the volume fraction of water and air respectively equals 0.5 is used to track the water surface. The flow over the weir is calculated by subtracting the outflow from the inflow. The flow over the weir is then combined with the water level to calculate a weir coefficient isolating C in the weir equation 3.1.

Furthermore the velocities in all 3 directions are extracted throughout the domain to determine the kinetic energy correction coefficient (α) at the upstream end of the channel. The kinetic energy correction coefficient (α) is defined as [Chanson, 2004]:

$$\alpha = \frac{\int_A \rho \cdot v^3 dA}{\rho \cdot V^3 A} \quad (5.3)$$

Where A is the cross sectional area of the channel (m^2), ρ is the density ($\text{kg} \cdot \text{m}^{-3}$), v is the velocity ($\text{m} \cdot \text{s}^{-1}$) and V is the average velocity over the cross sectional area.

5.4 CFD Model - Ideal Side Weir

To determine the relationship between the geometrical dimensionless coefficients and the discharge coefficient (C) of an ideal side weir, a simple geometry of a side weir in an open channel has been defined. As in the simulation of the stilling pond CSO structure, a constant weir thickness of 4 cm has been chosen. The following geometrical parameters has been changed systematically, using the values presented in table 5.3. Furthermore, the inflow and outflow has been altered to ensure a wide range of upstream channel Froude numbers will be modelled. In total 351 simulations has been conducted.

Table 5.3. The values of the important geometrical dimensions altered.

Parameter	Dimensions
L (m)	0.48, 0.96, 1.44, 2.88
B (m)	0.32, 0.48, 0.96, 1.44, 2.88
p (m)	0.16, 0.32, 0.48

The up- and downstream boundary has been modelled as uniform velocity boundaries. The area of the boundaries above the simulated water surface right next to the boundary has been converted to a no-flow boundary. The water doesn't enter a closed chamber through a pipe, as is typically the case for CSO chambers. Instead the uniform up and downstream boundaries more closely resembles the fully developed flow in an open channel. The boundaries have been located 0,48 m up and downstream the beginning and end of the weir respectively. The geometry and the chosen boundary conditions have been illustrated below:

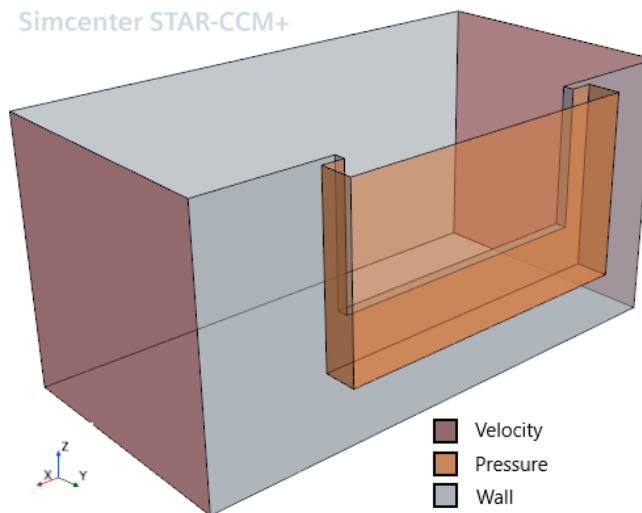


Figure 5.6. Illustration of the boundary conditions chosen. The top of the geometry has not been visualised not to block the backend of the domain, but it has also been modelled as a pressure boundary.

The mesh has been set up using the same criteria as in the simulation of the stilling pond CSO chamber, however as the geometry includes no pipes or dry flow channels no need for surface controls have been necessary. The physics and the definition of the water surface has likewise been modelled as previously described, and the weir coefficient has been determined for each of the 351 simulations throughout the domain.

5.5 CFD Model - Side Weir CSO Chamber

To further examine the flow characteristics of side weir CSO structures, the geometry of a simple side weir CSO chamber has been defined as illustrated in figure 1.3. 300 simulations has been carried out, where the following parameters has been randomly varied withing the ranges shown in table 5.4. To ensure the outflow never surpasses the inflow, the outflow has been defined as random fraction of the inflow.

Table 5.4. *The velocity has been recalculated to a flow assuming a full pipe.

	Lower limit	upper limit	Unit
B	0,48	2,4	m
p	0,08	0,64	m
b	0,48	2,88	m
L_{in}	0,48	1,92	m
L_{out}	0,48	1,92	m
D_{in}	0,12	0,48	m
D_{out}	0,08	0,48	m
v_{in}	0,2	2	$m \cdot s^{-1}$
Q_{out}	0	$0,9 \cdot Q_i$	-

The boundaries as well as the mesh and the physics have been modelled in the same manner as previously explained for the stilling pond CSO chamber. The boundaries and the geometry have been illustrated in figure 5.7.

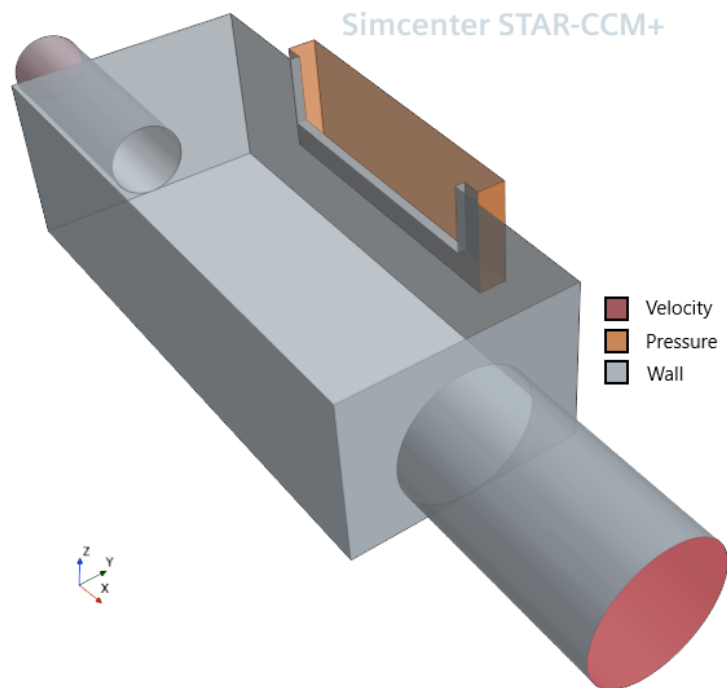


Figure 5.7. Illustration of the boundary conditions chosen. The top of the geometry has not been visualised not to block the backend of the domain, but it has also been modelled as a pressure boundary.

The water surface has been extracted like described in previous sections and the weir coefficient has been determined for all of the simulations.

Validation of CFD Modelling 6

The weir coefficient for the sharp contracted weir shown in figure 4.2 has been determined for 3 different flow rates in the laboratory. The measured flow rates has then been used as boundary conditions in the CFD model of the sharp crested weir, and the weir coefficient has been calculated based on the water level extracted from the model. The results has been presented in table 6.1:

Table 6.1. Laboratory experiment results of the sharp-crested weir showing measured water levels and the calculated weir coefficient along with the weir coefficient from the CFD model.

h (cm)	h/p (-)	Flow (L/s)	C (lab)	C (CFD)
5.1	0.17	12.0	0.41	0.423
6.3	0.2	16.2	0.41	0.426
7.5	0.23	21.7	0,42	0.424

The CFD model of the sharp crested weir has further been simulated increasing the flow rate up to $220 \text{ L} \cdot \text{s}^{-1}$. This has been done to compare the weir coefficient as a function of the $\frac{h}{p}$ -ratio with the theoretical from equation 3.5. The rating curve has been shown in figure 6.1.

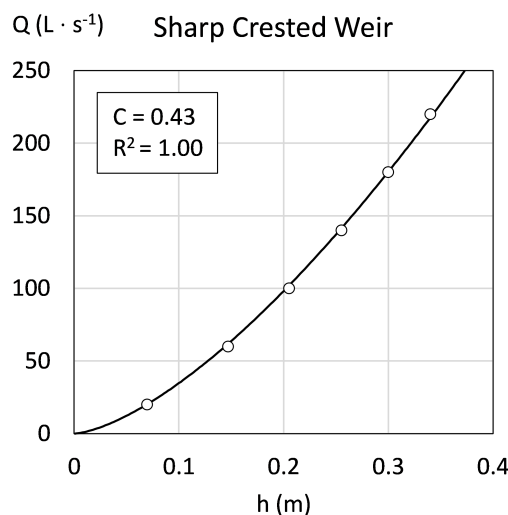


Figure 6.1. The CFD results of the sharp-crested weir. The rating curve has been fitted using a single weir coefficient.

The weir coefficient has been determined for each of the simulation of the sharp-crested weir using the

standard weir equation 3.1, and the equation compensating for the side contractions using equation 3.10. The results have been shown as a function of the $\frac{h}{p}$ -ratio.

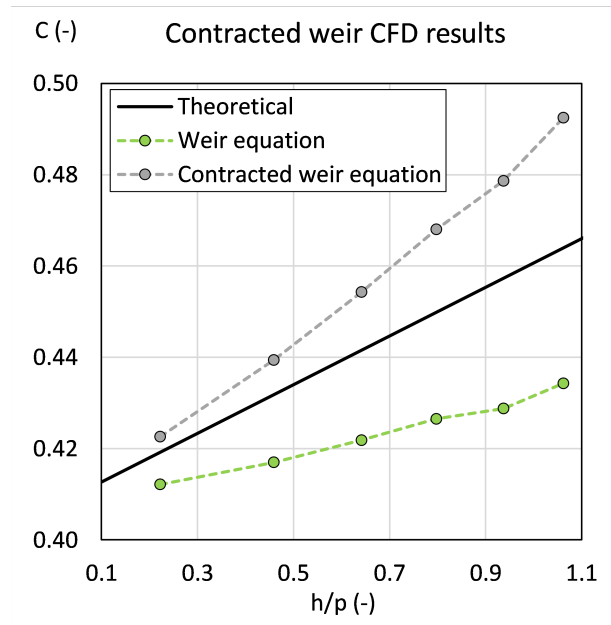


Figure 6.2. The weir coefficients of the CFD model compared to the literature graph of equation 3.5.

To remove the effect of the contraction, the weir coefficient of the sharp crested weir placed within the ideal channel has been calculated. The weir coefficient has been shown in figure 6.3 together with the results from figure 6.1 using the equation adjusting for the side contraction.

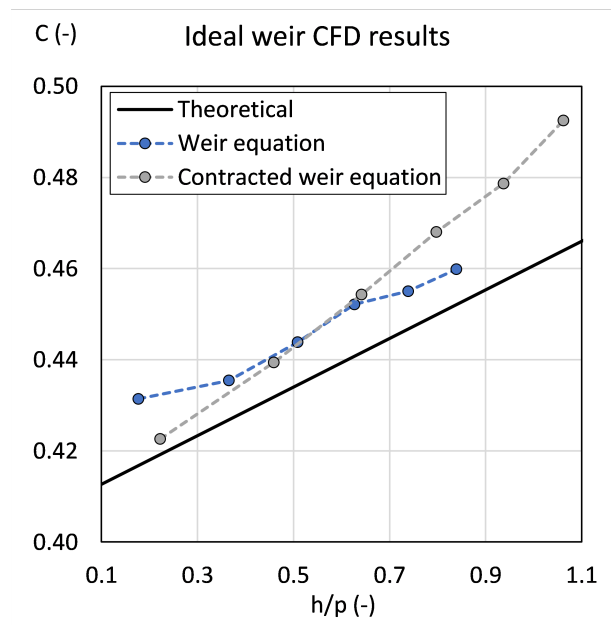


Figure 6.3. The calculated weir coefficient as a function of $\frac{h}{p}$ for the CFD model of the sharp-crested weir without any side contraction shown together with the weir coefficients from the sharp-crested weir with side contraction.

As it can be seen in figure 6.3. The weir with no contractions approximately follows the theoretical. The same is the case of the contracted weir using equation 3.10 to derive the weir coefficient, as long as we are within the range where the equation is valid ($h < \frac{1}{3}b$) which in this case corresponds to ($h < 0.6\frac{h}{p}$). The weir coefficients of the CFD model is however slightly higher than the theoretical.

As previously explained, a CFD model systematically varying the flow (effectively varying the height h) and the thickness (T) of an ideal weir has been conducted for the total of 48 simulations. The results were all in the domain short crested weirs (12 simulations) or sharp crested weirs (36). A significant difference in the calculated weir coefficient were seen as the water level gets large enough for the weir to spring free, and it goes from short to sharp weir. In this model this was found to happen at $h/T=3.4$. The weir coefficient has been shown as a function of the h/T -ratio for the short crested weir and as a function of the h/p -ratio for the sharp crested weir in figure 6.4 and 6.5 respectively.

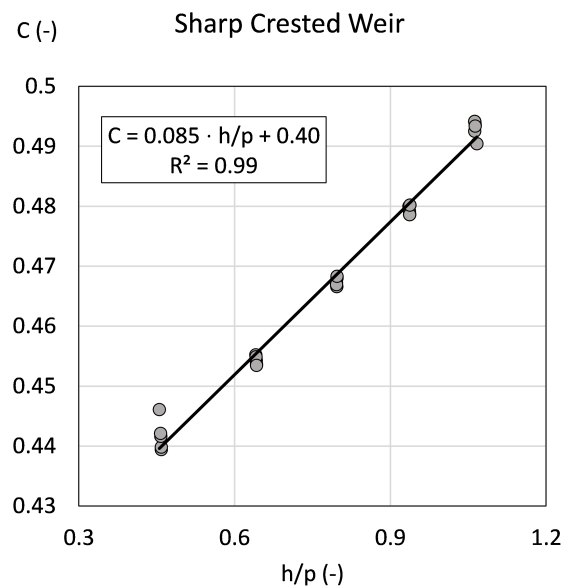
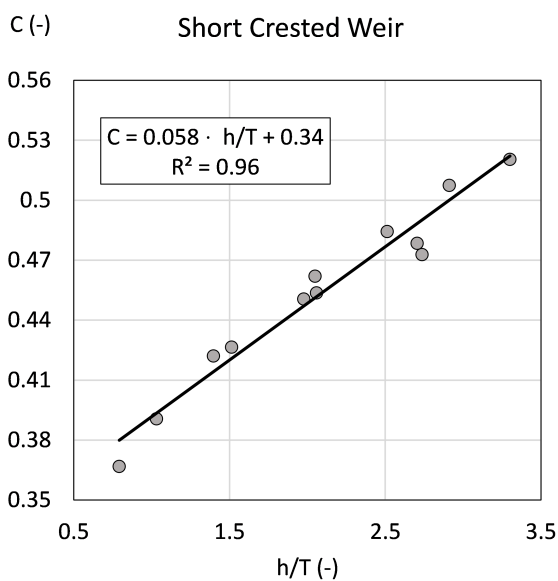


Figure 6.4. CFD results of the short crested weir.

Figure 6.5. CFD results of the sharp crested weir.

6.1 Sensitivity Analysis

To ensure that the results obtained are indented of both the spacial discretization used and the timestep used, a sensitivity analysis has been conducted.

The flow over a contracted weir similar to that of the sharp-crested weir of section 5.1 however with a crest length of 4 cm have been simulated using 5 different mesh refinement levels and 4 different timesteps at a flowrate of 10 l/s. The calculated weir coefficients has been shown in the table 6.2.

Table 6.2. The weir coefficient determined for the same simulation altering the timestep used and the base mesh size. The adaptive mesh refinement allows for mesh sizes 1/8 of the base mesh size.

		Timestep (s)			
		0.05	0.02	0.01	0.005
Basesize (m)	0.02	0.435	0.434	0.433	0.430
	0.04	0.433	0.433	0.432	0.429
	0.08	0.428	0.427	0.425	0.421
	0.16	0.439	0.436	0.442	0.439
	0.32	0.440	0.431	0.430	0.428

As it can be seen, all if the values are within a range of ± 0.01 . The results therefore indicate that the mesh size and timestep used have little to no significant influence. It is therefore assumed that the results are independent of the mesh and time step used within the ranges investigated.

7.1 Stilling Pond

The 221 randomly generated stilling pond CSO structures have been analysed, and the weir coefficient has been determined depending on the relative measurement location of the water level. An example of the calculated water surface as well as the flow streamlines has been shown in figure 7.1.

Simcenter STAR-CCM+

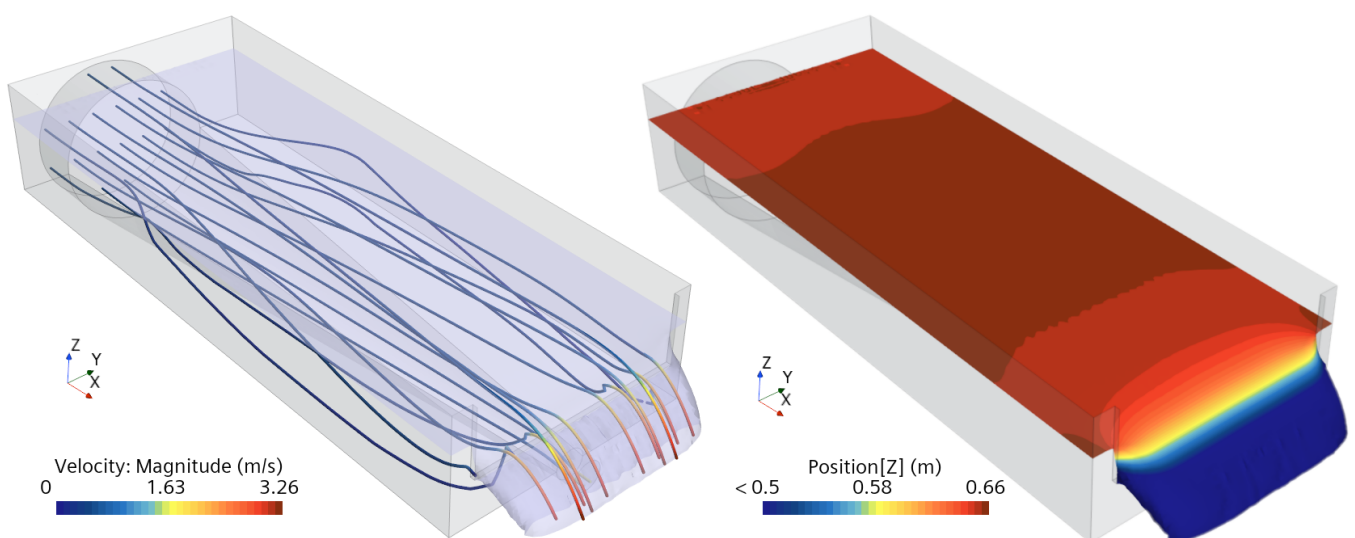


Figure 7.1. Water surface and streamlines for one of the randomly generated stilling pond CSO structures.

The dimensionless parameters presented in equation 3.3 expected to govern the weir coefficient has been calculated for each of the generated structures. The ranges of the dimensionless parameters analysed have been shown in table 7.1.

Table 7.1. The 95% range of the generated parameters of the stilling pond CSO structures.

Parameter	95 % range (mean)
Fr	0.07 - 0.95 (0.45)
B/h	1.79 - 35.8 (10.8)
h/T	1.75 - 16.7 (5.55)
h/p	0.10 - 1.85 (0.43)
L/B	0.56 - 4.87 (1.97)
D _{in} /B	0.20 - 0.67 (0.40)
D _{out} /B	0.05 - 0.33 (0.17)
b/B	0.67 - 0.93 (0.84)
α	1.92 - 28.8 (8.79)

To initially asses the relationship between the different dimensionless parameters and the weir coefficient, a Pearson correlation analysis has been carried out. The analysis has been based on the water level being measured in the center of the chamber.

Table 7.2. Pearson correlation coefficients between the weir coefficient and the different dimensionless parameters from the dimensional analysis.

Fr _B	Fr _{D_{in}}	B/h	h/T	h/p	b/h	D _{in} /B	D _{out} /B	b/B	α
0.74	0.91	-0.15	-0.02	-0.30	-0.06	-0.29	-0.21	-0.14	0.01

As seen in table 7.2, the Froude number has been found to be highly correlated with the weir coefficient. Two different Froude numbers have been used, one where the velocity has been assumed to be based on the width of the channel called (Fr_B) calculated as shown in equation 7.1, and one where the inlet diameter has been used to define the velocity called Fr_{D_{in}} calculated as shown in equation 7.2.

$$Fr_B = \frac{Q_{in}}{B \cdot (p+h) \cdot \sqrt{(p+h) \cdot g}} \quad (7.1)$$

$$Fr_{D_{in}} = \frac{Q_{in}}{D_{in} \cdot (p+h) \cdot \sqrt{(p+h) \cdot g}} \quad (7.2)$$

The use of the first Froude number assumes a uniform flow velocity in the chamber, and thereby a perfect dispersion of the inlet velocity. The second definition of the Froude number assumes a jet, where dispersion only happens in the vertical direction. Due to the larger correlation coefficient, the latter will be used in the following.

A simple multiple linear regression (MLR) has been used to further asses the relationship between the different parameters and the weir coefficient. The parameters have been excluded one by one, in order corresponding to the correlation coefficient of table 7.2. The coefficient of determination has been showed both as a regular value and as bias corrected value, taking into account the reduced

number of degrees of freedom:

$$\bar{R}^2 = 1 - (1 - R^2) \cdot \frac{n - 1}{n - p - 1} \tag{7.3}$$

Where n is the number of datapoints (221), and p is the number of parameters used.

Table 7.3. The coefficient of determination using different numbers of input parameters.

	R^2	\bar{R}^2
Fr	0.82	0.82
Fr, h/p	0.87	0.86
Fr, h/p, D_{in}/B	0.87	0.86
Fr, h/p, D_{in}/B , D_{out}/B	0.88	0.87
Fr, h/p, D_{in}/B , D_{out}/B , B/h	0.88	0.87
Fr, h/p, D_{in}/B , D_{out}/B , B/h , b/B	0.88	0.87
Fr, h/p, D_{in}/B , D_{out}/B , B/h , b/B , L/B	0.88	0.87
Fr, h/p, D_{in}/B , D_{out}/B , B/h , b/B , L/B , h/T	0.89	0.88
Fr, h/p, D_{in}/B , D_{out}/B , B/h , b/B , L/B , h/T , α	0.89	0.89

As it can be seen in table 7.3 the weir coefficient is very much depended on the Froude number. The correlation is slightly improved when including p/h as well. However the introduction of the rest of the parameters doesn't increase the fit significantly.

A slightly better fit between the Froude number and the weir coefficient can be achieved using a 2. order polynomial function of the form of equation 7.4 rather than a linear regression. This has been shown in figure 7.2.

$$C = a \cdot Fr^2 + b \cdot Fr + c \tag{7.4}$$

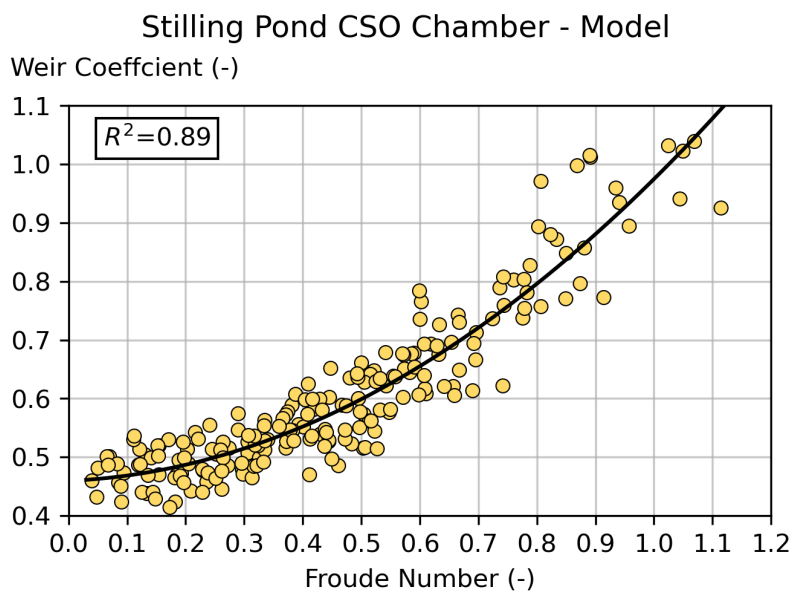


Figure 7.2. Relationship between the Froude number and the weir coefficient, based on a water level measured in the middle of the CSO chamber.

Using the water data from the middle of the chamber, the following relationship has been determined:

$$C = 0.473 \cdot Fr^2 - 0.042 \cdot Fr + 0.460 \quad (7.5)$$

The parameters a, b and c has been shown in H as a function of the relative location of the water level measurement point.

The above analysis has been based on a water level measured in the middle of the CSO chamber. In figure 7.3 the Root Mean Square Error (RMSE) has been calculated throughout the domain, depending the on the relative position of the water level measurement. The red dot indicates the proposed location for determining the water level.

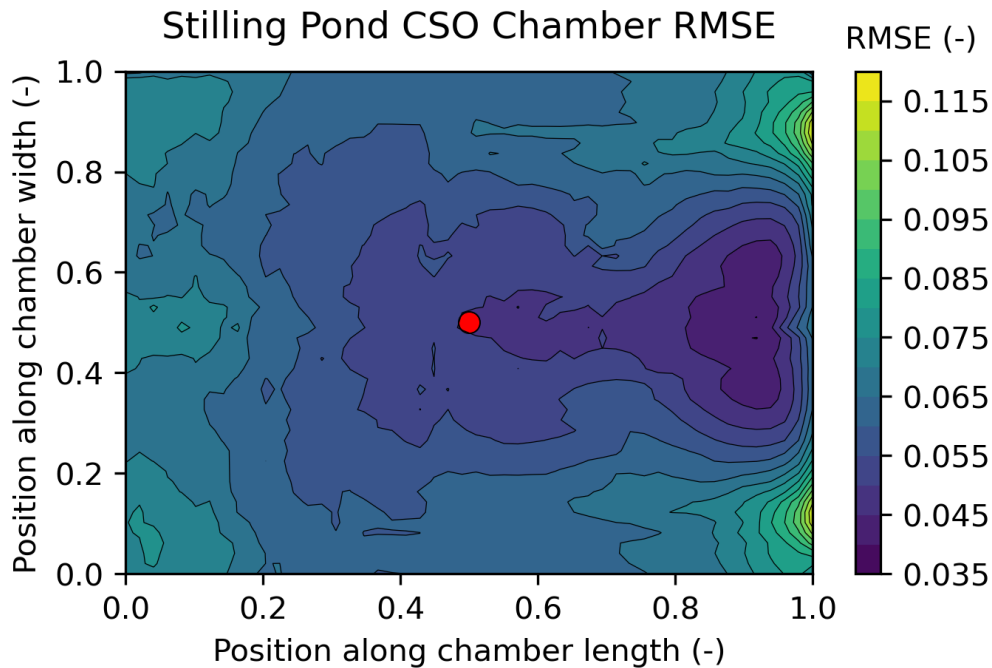


Figure 7.3. The RMSE when predicting the weir coefficient using the Froude number. The prediction has been based of the 2. order polynomial function. The inlet of the chamber is to the left, and the outlet as well as the weir is to the right.

The coefficient of determination has been shown throughout the chamber in figure 7.4.

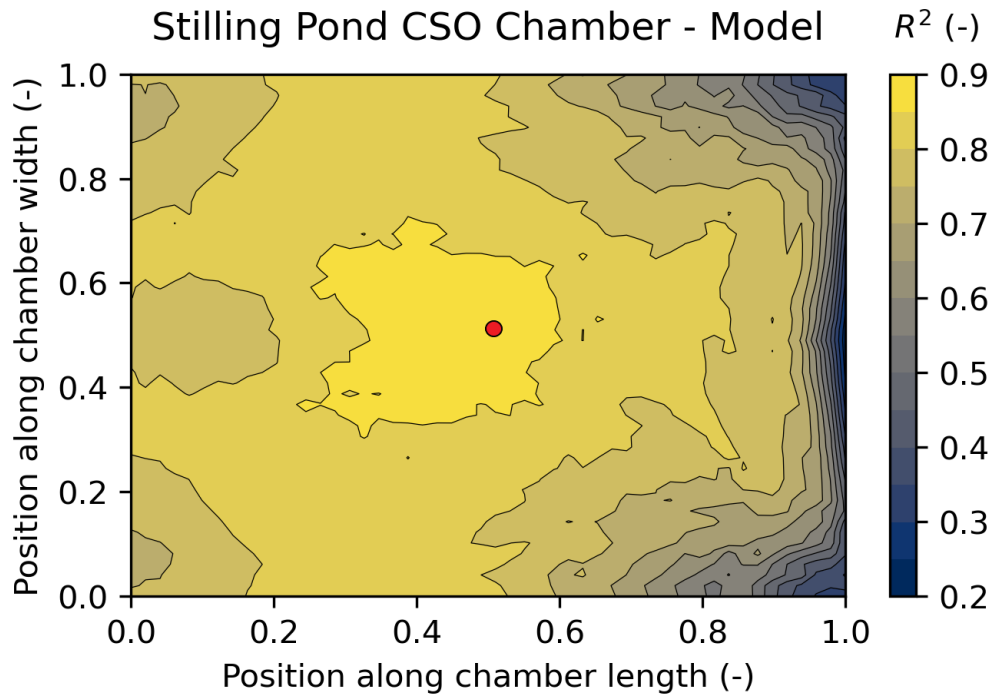


Figure 7.4. R^2 predicting the weir coefficient using the Froude number. The inlet is to the left, the weir is to the right. The position is the relative positing.

7.2 Ideal Side Weir

Like in the previous section, the weir coefficient has been determined throughout the domain for all 351 simulations. Each weir coefficient been determined using a single data point consisting of a weir flow and water level reading. To allow for comparison with the stilling pond CSO structure, the simulations where h/T were found to be below 1.25 has not been included in the following, however, the entire dataset will be analysed as well. In figure 7.5 the streamlines and the water surface has been shown for one of the randomly generated side weirs.

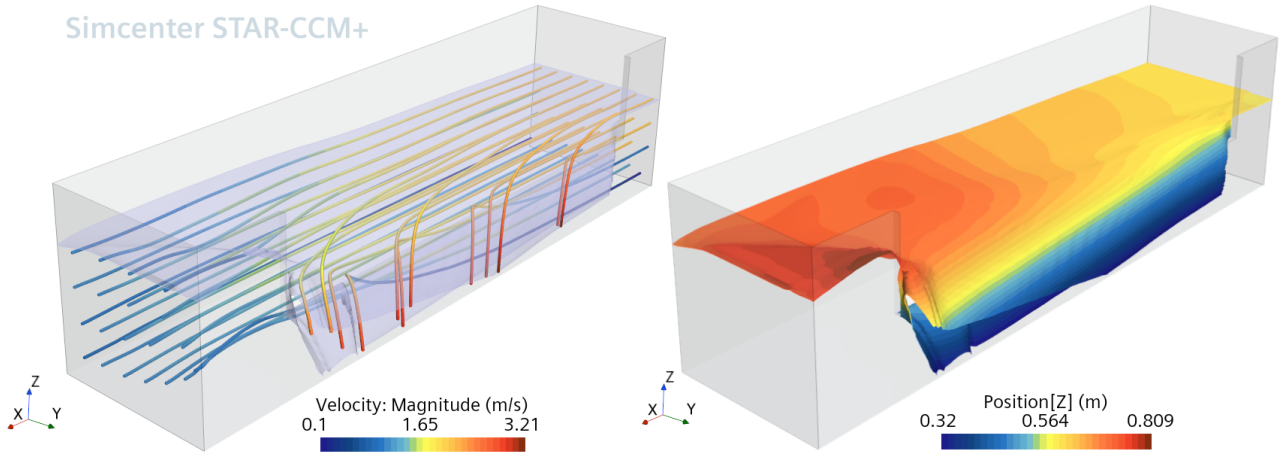


Figure 7.5. Water surface and streamlines for one of the randomly generated side weirs.

The ranges of the calculated dimensionless parameters have been shown in table 7.4.

Table 7.4. The 95% range of the generated parameters of the side weirs.

Parameter	95 % range (mean)
Fr	0.05 - 0.76 (0.33)
b/h	1.29 - 21.1 (7.15)
h/T	1.42 - 13.2 (5.52)
h/p	0.15 - 1.64 (0.40)
L/B	0.33 - 3.00 (1.42)
$v_{\text{out}}/v_{\text{in}}$	0.00 - 0.91 (0.48)

A Pearson correlation analysis has initially been used to assess the relationship between the weir coefficient and the defined dimensionless parameters. The water level has been extracted in the downstream corner opposite the weir. The correlations coefficients have been shown in table 7.5.

Table 7.5. Pearson correlation coefficients between the dimensionless parameters suspected to govern the flow dynamics of the side weir and the calculated weir coefficient.

Fr	b/h	h/T	h/p	b/B	$v_{\text{out}}/v_{\text{in}}$
-0.89	0.08	-0.25	0.29	-0.40	-0.38

As it can be seen in table 7.5 the Froude number has been found to be strongly negatively correlated with the weir coefficient. The Froude number is the upstream channel Froude number, and has been defined using the same water depth as the one used to calculate the weir coefficient. Thereby a small error is introduced, as the flow used is extracted at the inlet to the channel. The error doing this has however been found to be negligible. The Froude number has been calculated using equation 7.1.

Multiple linear regression has been used to make a simple model, predicting the weir coefficient using the above parameters. The coefficient of determination has been shown in table 7.6.

Table 7.6. Coefficient of determination between the weir coefficient and the dimensionless parameters. The values have been corrected to adjust for the reduced degrees of freedom as more parameters are included.

Parameters used in model	\bar{R}^2
Fr	0,81
Fr, b/B	0,81
Fr, b/B, v_{out}/v_{in}	0,82
Fr, b/B, v_{out}/v_{in} , h/p	0,82
Fr, b/B, v_{out}/v_{in} , h/p, h/T	0,84
Fr, b/B, v_{out}/v_{in} , h/p, h/T, b/h	0,84
b/B, v_{out}/v_{in} , h/p, h/T, b/h	0.71

As it can be seen from table 7.6, the Froude number is highly correlated with the weir coefficient. The effect of including the rest of the considered parameters is negligible. Froude number has been found to be an even better predictor than the rest of the parameters combined. Therefore in the following only the Froude number is used in the model. A fit using a 2. order polynomial function has been shown in figure 7.6 resulting in the function shown in equation 7.6.

$$C = -0.072 \cdot Fr^2 - 0.252 \cdot Fr + 0.461 \quad (7.6)$$

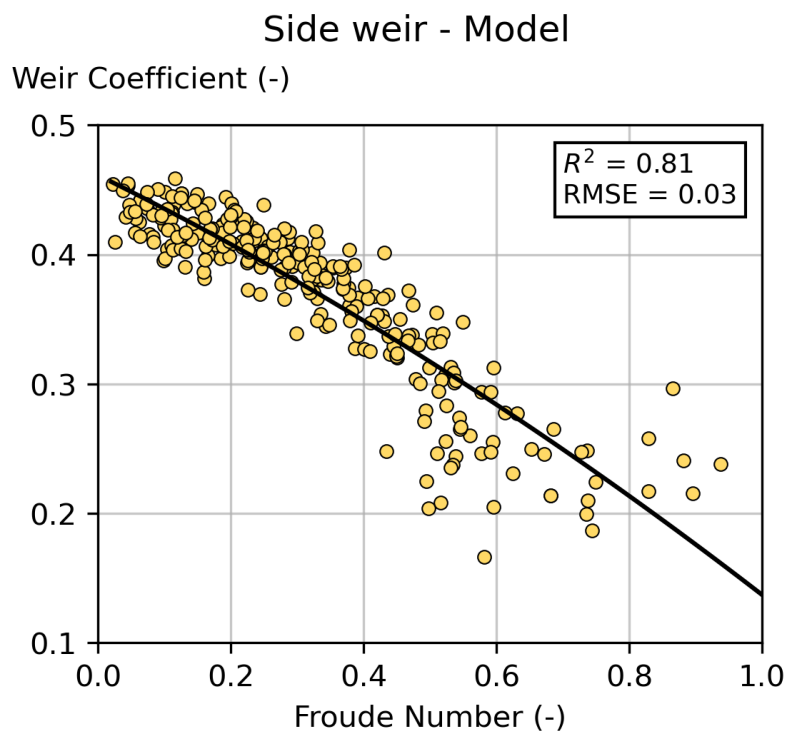


Figure 7.6. Relationship between the Froude number and the weir coefficient for the ideal side weir. The water level used has been measured in the downstream corner opposite the weir.

The parameters of equation 7.6 has been determined depending on the position of the water level measurement. The parameters has been shown in appendix H. The RMSE has been shown throughout the domain in figure 7.7.

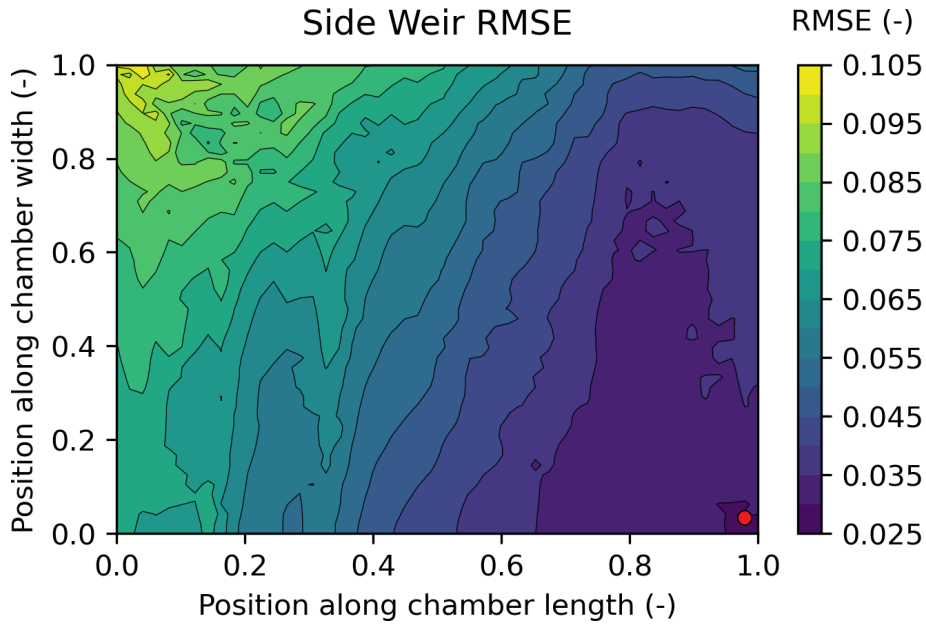


Figure 7.7. RMSE from left to right. Weir is located on top

The coefficient of determination has been shown in figure 7.8.

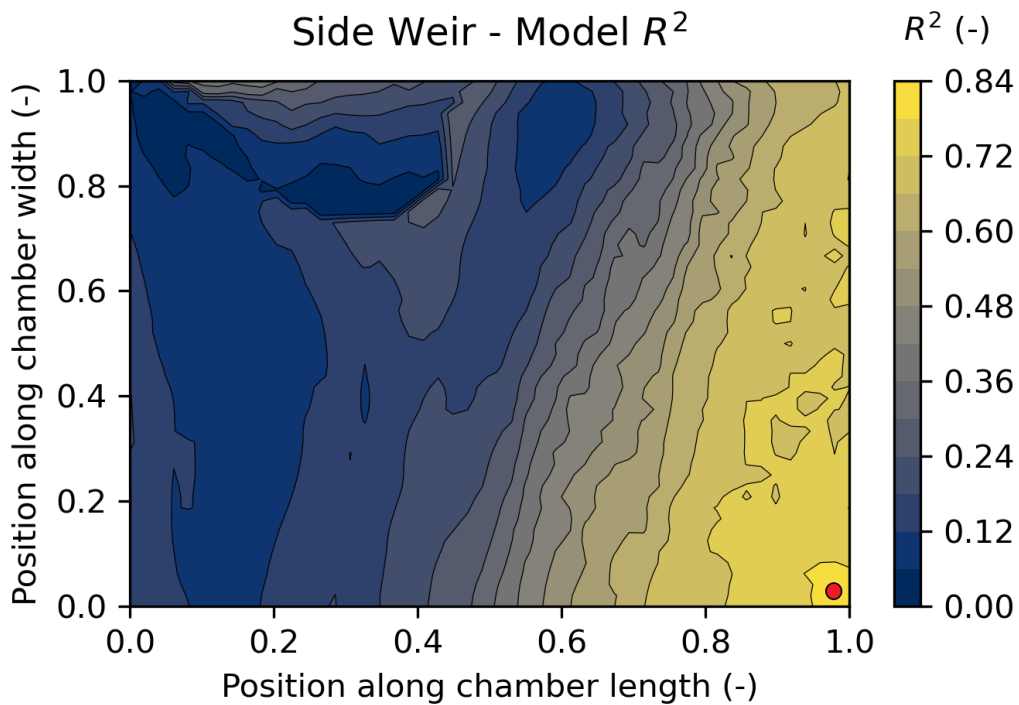


Figure 7.8. Relationship between Founde number and C, inflow from left to right. Weir is located on top

A slightly better prediction has been found using an average water level over an area rather than the water level of a single location. Figure 7.9 shows the correlation using the average water level of an area, that extends from the weir to the center line of the chamber along the whole length of the weir. This correlation has been compared to four different literature formulas by [Bagheri et al., 2014], [Raju et al., 1979], [Subramanya and Awasthy, 1972] and [Nadesamoorthy and Thomson, 1972]. All of the 4 formulas are based on sharp crested wearies, and with the exception of the one by Bagheri et al. [2014] they are all based on the de-Marchi discharge coefficient (C_M). As the de-Marchi discharge coefficient is based on a predicted water surface profile, a comparison is most valid when using an average surface level rather than a single measurement location. The different literature formulas have been shown together with the fitted curve in figure 7.9.

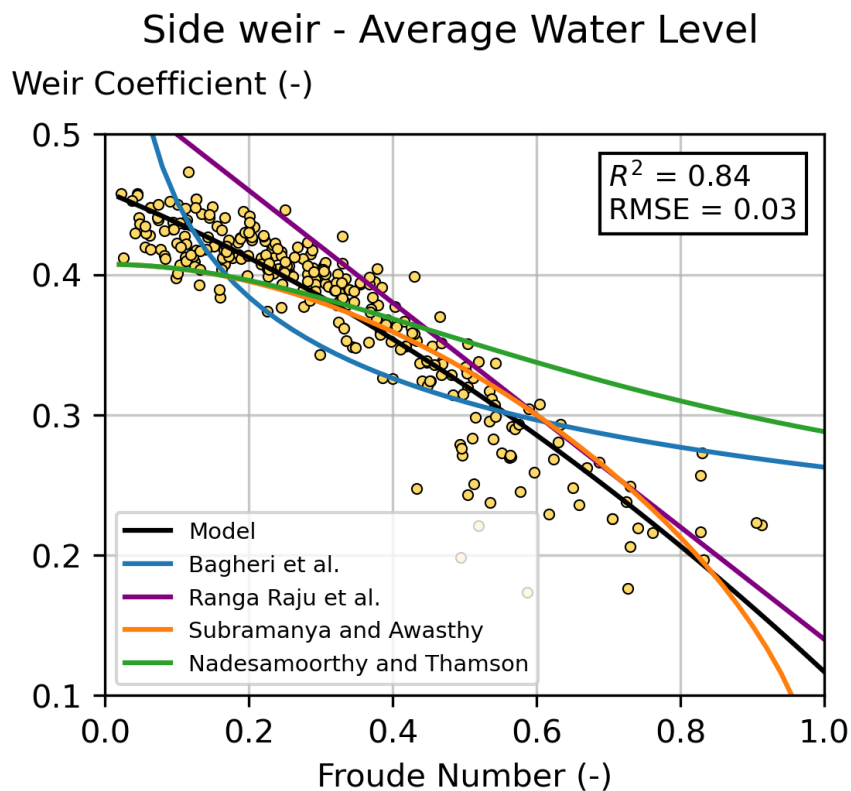


Figure 7.9. Relationship between the Froude number and the weir coefficient based on an average water level together with the four literature graphs. The RMSE and the R^2 is referring to the model of this project [Bagheri et al., 2014], [Raju et al., 1979], [Subramanya and Awasthy, 1972] and [Nadesamoorthy and Thomson, 1972].

So far only the structures where the h/T were above 1.25 have been included in the analysis, excluding the broad crested weir, and part of the short crested weirs. In figure 7.10 the whole dataset has however been included:

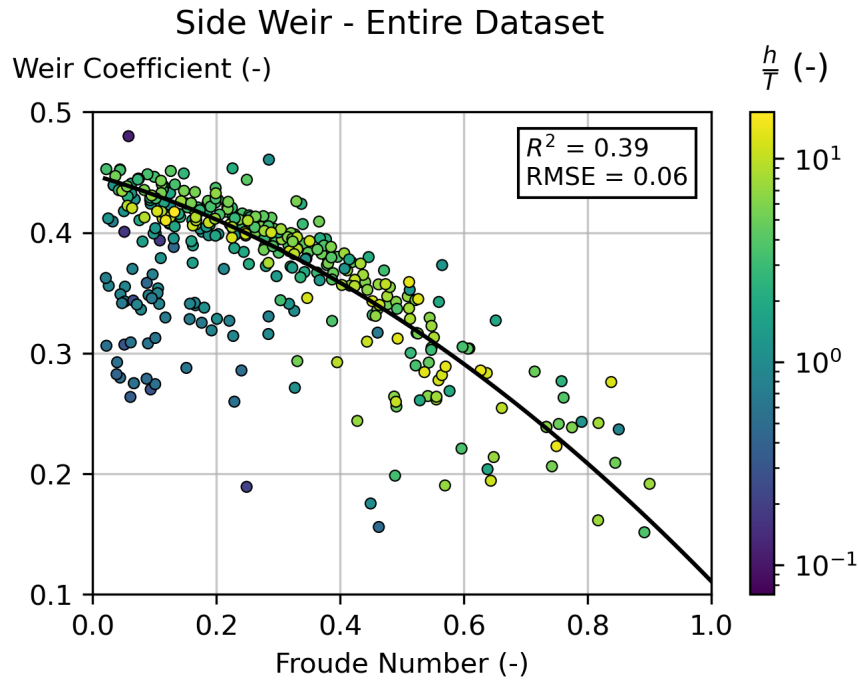


Figure 7.10. The relationship between Froude number and C based on the average water level of figure 7.9 show together with the entire dataset.

A subset where only the simulations having a Froude number below 0.2 has been shown in figure 7.11.

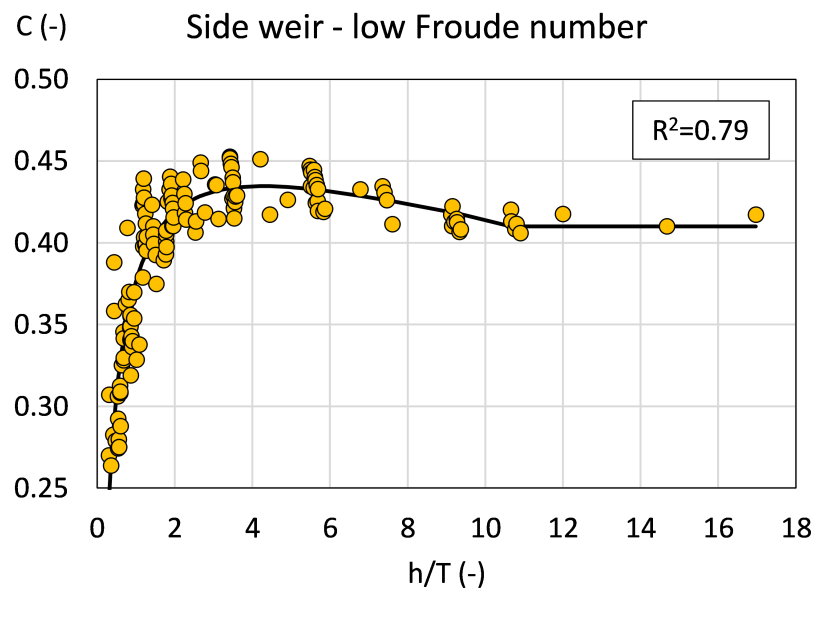


Figure 7.11. The weir coefficient of the side weir for Fr under 0.2

As it can be seen is the weir coefficient is strongly influenced by the h/T ratio, when the value

becomes lower than 2. When h/T becomes above 10, the coefficient is seen to be constant around 0.41, being the standard value of a sharp crested weir. For values of h/T below 10 the following equation has been fitted to the data. This is also the graph shown in figure 7.11.

$$C = -0.147 \cdot \left(\log \left(\frac{h}{T} \right) \right)^2 + 0.186 \cdot \log \left(\frac{h}{T} \right) + 0.376 \quad (7.7)$$

7.3 Side Weir CSO Chamber

In reality we do seldom have an ideal channel when dealing with combined sewer overflow structures, and the ideal channel above therefore is not expected to be representative for majority of the side weir CSO structures. Instead the water enters and exists the chambers through a pipe, which most often has a diameter smaller than the width of the channel leading to a non uniform velocity distribution. The weir coefficient has been determined throughout the domain for the 300 randomly generated side weir CSO structures. The simulated water surface as well as the streamlines throughout the chamber has been shown for one of the side weir CSO structures in figure 7.12.

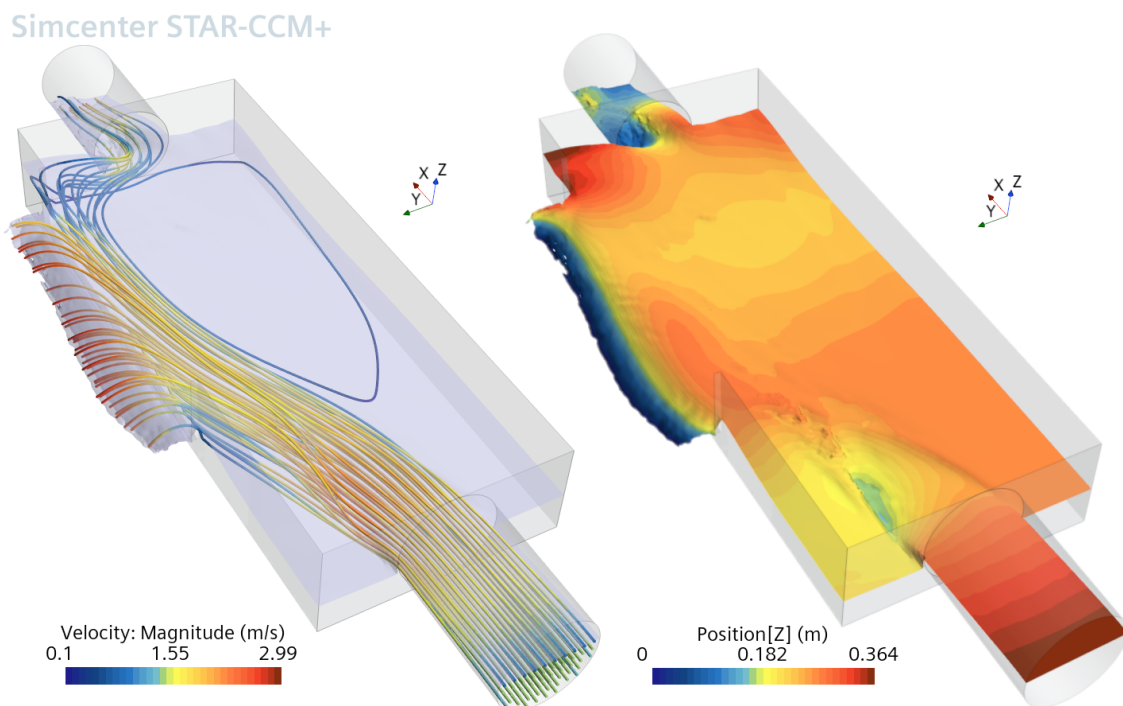


Figure 7.12. Water surface and streamlines for one of the randomly generated side weir CSO structures.

Due the sudden expansion at the inlet of the chamber, we a lot of turbulence is typically seen at the

inlet of the chamber leading to a loss of kinetic energy. This loss of energy can as illustrated in figure 1.4 in some cases result in a hydraulic jump. This behaviour is also seen in some of the simulations, when the inflow is large, and the weir height (p) is low. A small hydraulic jump is seen in figure 7.12. The ranges of the dimensionless parameters of the generated CSO structures have been shown in table 7.7.

Table 7.7. The 95% range of the dimensionless parameters of the generated side weir CSO structures.

Parameter	95 % range (mean)
Fr	0.12 - 1.07 (0.5)
B/h	1.92 - 18.5 (6.51)
h/T	1.61 - 14.3 (4.17)
h/p	1.12 - 4.00 (1.59)
D_{in}/B	0.40 - 0.96 (0.61)
D_{out}/B	0.23 - 0.83 (0.47)
b/B	0.42 - 4.25 (1.65)
L_{in}/h	1.60 - 21.3 (7.26)
L_{out}/B	0.85 - 7.39 (2.91)
v_{out}/v_{in}	0.02 - 0.84 (0.41)

Like previously a Pearson correlation analysis has been carried out to asses the relationship between the dimensionless parameters and the weir coefficient. The analysis has been done for two data points, one in the downstream corner closest to the weir and one in center of the chamber.

Table 7.8. Results of the Pearson correlation analysis for the side weirs CSO chamber. The correlation coefficients has been determined for two different measurement locations.

	Fr_B	$Fr_{D_{in}}$	B/h	h/T	h/p	D_{in}/B	D_{out}/B	b/B	L_{in}/h	L_{out}/h	α	v_{out}/v_{in}
Center	-0.17	-0.19	0.35	0.14	0.34	-0.30	-0.19	-0.07	0.05	0.35	0.14	-0.23
Corner	-0.63	-0.73	0.25	0.27	0.36	-0.01	0.05	0.01	0.22	0.27	0.04	-0.63

Two Froude numbers have been defined based on equation 7.1 and 7.2. The Froude number based on equation 7.2 has been used due to the higher correlation coefficient.

A multiple linear regression using the dimensionless parameters to predict the weir coefficient has been carried out. The parameters have been excluded one by one in ascending order with respect to their correlation coefficient, and the coefficient of determination has been tracked. The coefficients of determination have been shown in table 7.9.

Table 7.9. The coefficient of determination using multiple linear regression to predict the weir coefficient.

Parameters used in model	R^2	\bar{R}^2
Fr	0.53	0.53
Fr, v_{out}/v_{in}	0.77	0.76
Fr, v_{out}/v_{in} , h/p	0.77	0.77
Fr, v_{out}/v_{in} , h/p , h/T	0.77	0.77
Fr, v_{out}/v_{in} , h/p , h/T , L_{out}/h	0.77	0.77
Fr, v_{out}/v_{in} , h/p , h/T , L_{out}/h , B/h	0.78	0.77
Fr, v_{out}/v_{in} , h/p , h/T , L_{out}/h , B/h , L_{in}/h	0.78	0.77
Fr, v_{out}/v_{in} , h/p , h/T , L_{out}/h , B/h , L_{in}/h , D_{out}/B	0.78	0.78
Fr, v_{out}/v_{in} , h/p , h/T , L_{out}/h , B/h , L_{in}/h , D_{out}/B , α	0.82	0.82
Fr, v_{out}/v_{in} , h/p , h/T , L_{out}/h , B/h , L_{in}/h , D_{out}/B , α , D_{in}/B	0.83	0.82
Fr, v_{out}/v_{in} , h/p , h/T , L_{out}/h , B/h , L_{in}/h , D_{out}/B , α , D_{in}/B , b/B	0.85	0.85

Using the multiple linear regression, the RMSE of the model has been shown throughout the domain in figure 7.13, 7.14. The RMSE has been shown in two figures to illustrate the ranges of values found.

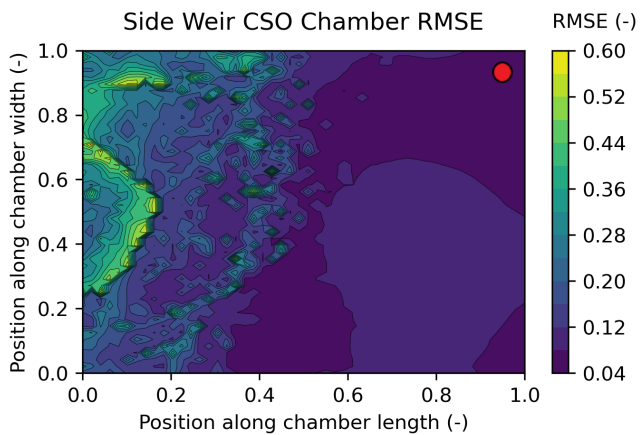


Figure 7.13. The RMSE when predicting the weir coefficient. Inflow from left to right, weir is placed at the top. The whole range has been shown.

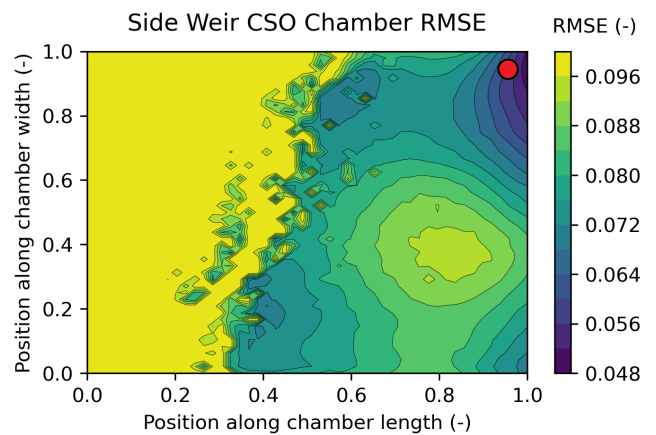


Figure 7.14. The RMSE when predicting the weir coefficient. Inflow from left to right, weir is placed at the top. The range of RMSE has been cut off at 0.1.

The coefficient of determination has been shown in figure 7.15.

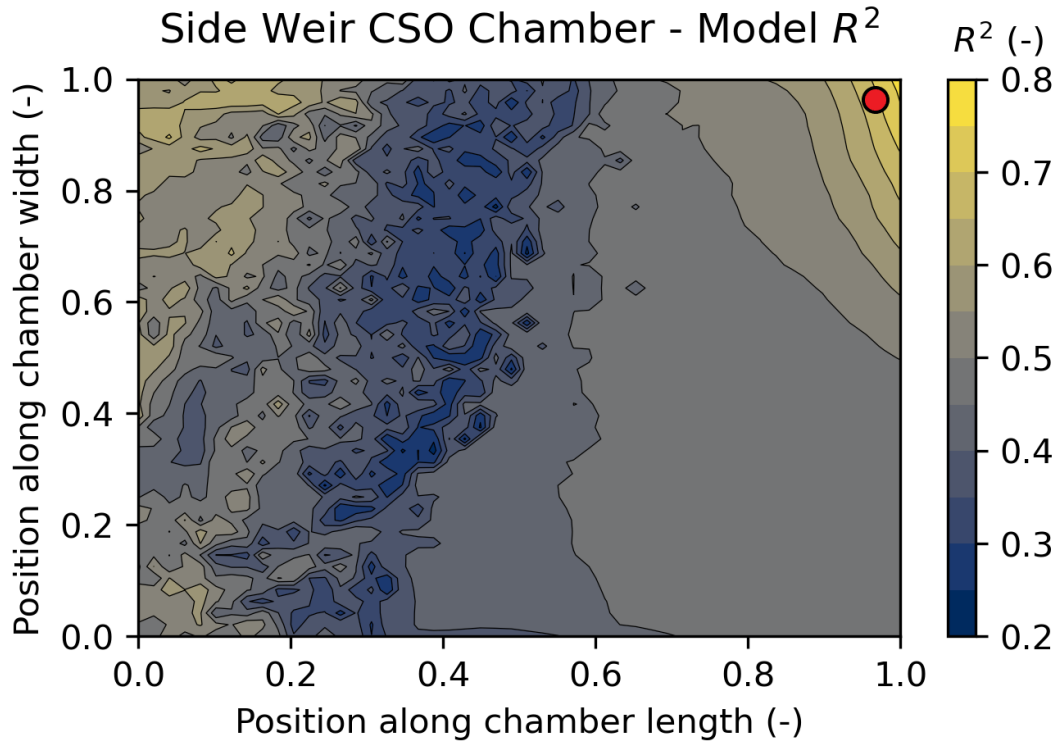


Figure 7.15. Relationship between Froude number and the weir coefficient, inflow from left to right. Weir is located at the top.

As it can be seen in table 7.9 the coefficients of determination drops slightly when the kinetic energy correction coefficient (α) is excluded. It has however been found that combining Fr_B and α in one parameter by multiplying the square root of the kinetic energy correction coefficient and the Froude number gives a fairly good prediction - see table 7.10.

Table 7.10. Coefficient of determination using the altered Froude number.

	R2	R2*
$Fr_B \cdot \sqrt{\alpha}$	0,57	0,58
$Fr_B \cdot \sqrt{\alpha, \frac{v_o}{v_i}}$	0,80	0,79

The following figure shows the weir coefficient plotted against the corrected Froude number and the inflow to outflow ratio.

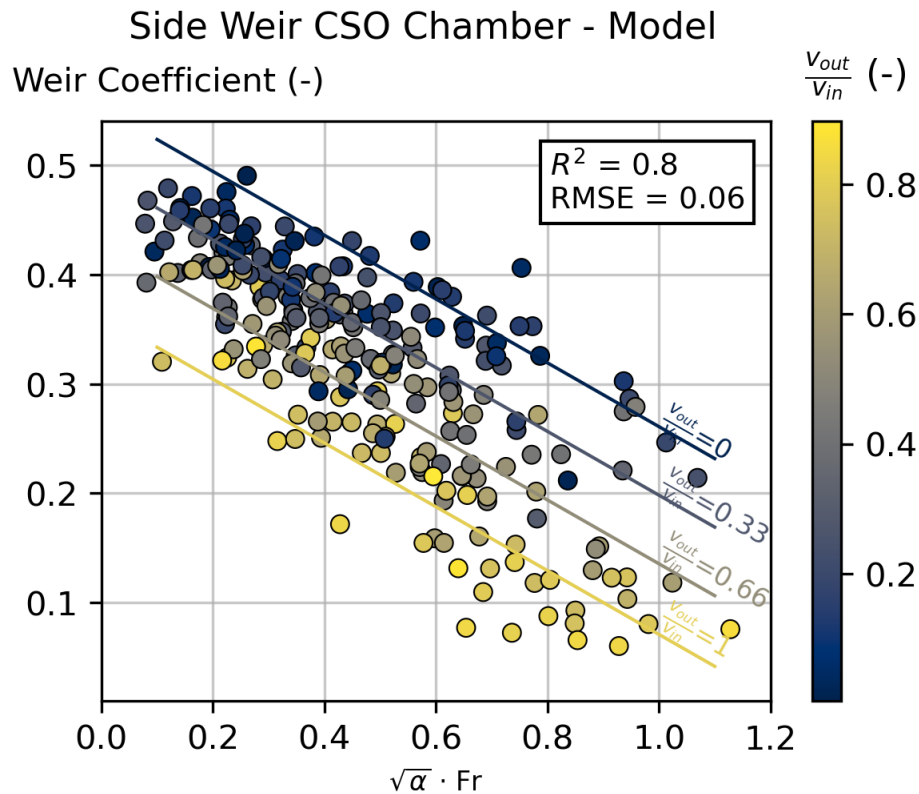


Figure 7.16. Correlation between the weir coefficient, the altered Froude number and the outflow-inflow ratio.

7.4 Splitting up the Weir Coefficient

As explained previously and shown in equation 3.9 the weir coefficient can be seen as a combination of the ideal weir coefficient (C_i) and a model coefficient that compensates for the error when determine the water level (C_m). When predicting the weir coefficient using the Froude number, it is hypothesized that we are effectively compensating for the uneven water surface within the chamber, however we aren't taking into account the ideal weir coefficient, which depends on the geometry of the weir in relation to the height of the water level, as shown for the side weir.

As the Froude number approaches zero, the water effectively comes to a standstill. The weir coefficient for the side weir and the stilling pond CSO structure should therefore theoretically be the same, as the flow no more has any effect. The interception at $Fr = 0$ can consequently be interpreted as the average ideal weir coefficient of the generated structures. As it can be seen of figure 7.2 and 7.6 the fitted curve for both the stilling pond CSO structure and the ideal side weir intercepts the y-axis

at $C=0.46$. By using this as the average ideal weir coefficient, the model coefficient (C_m) can be predicted by dividing the equation 7.6 and 7.5 with 0.46.

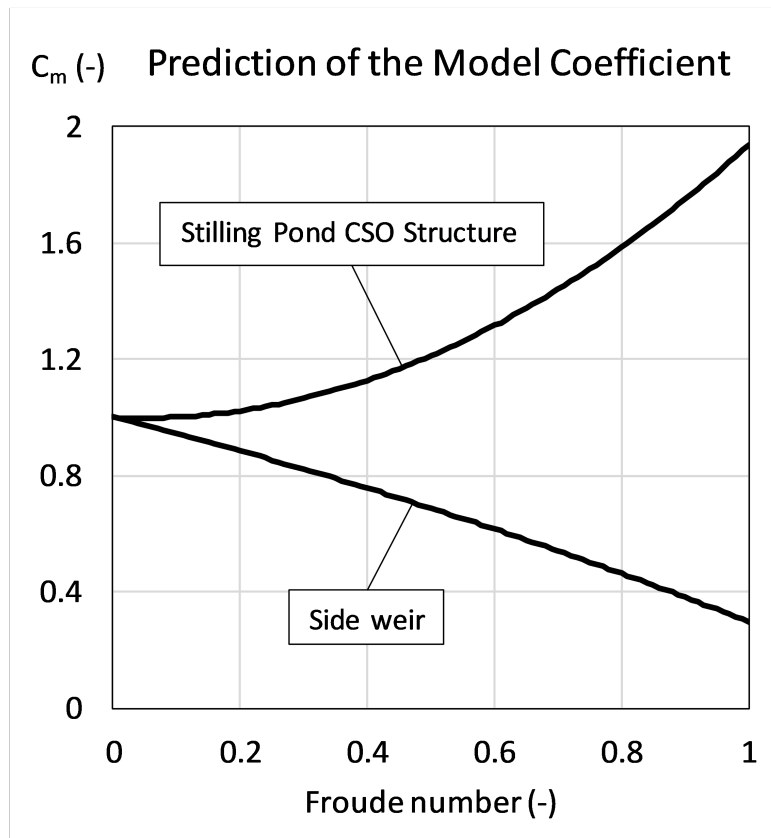


Figure 7.17. The predicted model coefficients of the stilling pond CSO structure and the ideal side weir. The coefficients are specific for position where the water level is determined.

Knowing the ideal weir coefficient of the weir considered eg. by using the relationships of figure 6.4 and 6.5 or using equation 7.7. The weir coefficient of a given structure can be estimated by multiplying the model coefficient with the ideal weir coefficient. This has been done for entire dataset of the simulated side weirs using the ideal weir coefficient of equation 7.7 in combination with the model coefficient of figure 7.17. A comparison of the modelled and the predicted weir coefficients has been shown in figure 7.18.

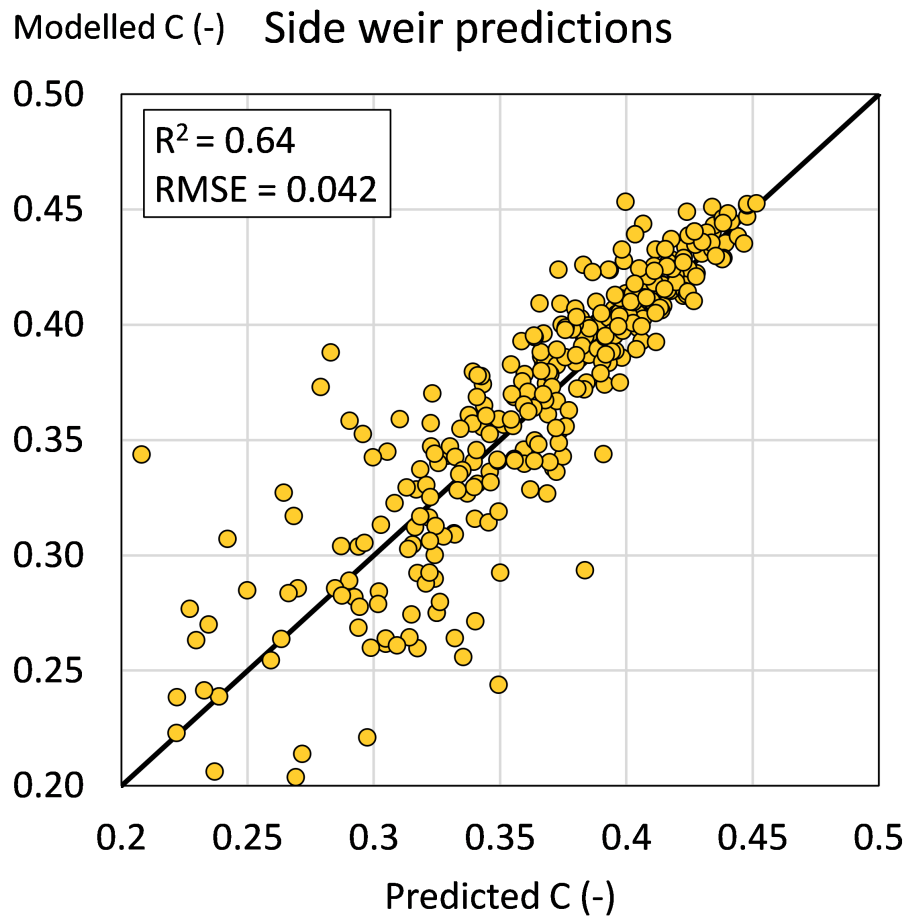


Figure 7.18. The predicted weir coefficients of the 351 side weirs, plotted against the values extracted from the CFD model.

Adjusting for CSO Fittings

8

To reduce the effect of CSO discharges on the natural environment as well as to minimize aesthetic pollution, many CSO structures have from start been fitted or have later been retrofitted with screens and scumboard. The aforementioned screening of CSO structures from the Municipality of Aarhus, Denmark has also looked into what contraptions the 67 structures were equipped with [Murla et al., 2018].

Table 8.1. [Murla et al., 2018]

CSO fitting	Frequency
Screen	70 %
Scumboard	26 %

All of the CSO structures equipped with a scumboard were also equipped with a screen. Of the structures categorise as weir based, 90 % were equipped with a screen.

Many CSO chambers are equipped with baffles or scumboards (from hereon called scumboards). Scumboards are a very simple contraption often just build as a metal plate, made to retain floatables within the CSO chamber thereby reducing the pollutant load to the receiving water body [Iwasa et al., 2019]. Correctly installed scumboards only induces little resistance to the flow, and are therefore not suspected to affect the weir flow significantly. Scumboards are however typically installed in combination with a screen as shown in the survey of [Murla et al., 2018].

The function of screens is to retain large solid objects within the sewer system. However, screens have a tendency to get clogged, which reduces the flow over the weir and alters the rating curves of the CSO structure. Due to the clogging nature of the screen, regular maintenance is needed to ensure proper function. In some locations, mechanical self-cleaning screens have been installed to mitigate this problem [WaPUG, 2006].

Screens are designed to capture and retain gross solids, which typically are defined as solids with a length exceeding 6 mm in any two dimensions [Murali et al., 2019]. In the UK, regulation of the

screen size exist, requiring the retention of gross solids near public accessible areas [WaPUG, 2006]. However, in Denmark, there are no specific regulations regarding screen size, and it is suspected that the grid size of danish screens typically is larger than 6 mm. Various types of screens exist, however steel bar gratings are often seen.

The screens can be installed in the CSO structure in a variety of ways, but most common is vertically mounted screens placed on top of the crest as well as horizontal mounted screens placed upstream the weir [WaPUG, 2006]. Both types has been illustrated in figure 8.1 and 8.2. Horizontal screens placed on the dry side of the weir are also sometimes seen, but they are suspected to be less common, and effects on the hydraulics of the CSO chamber is typically only seen under fully clogged conditions.

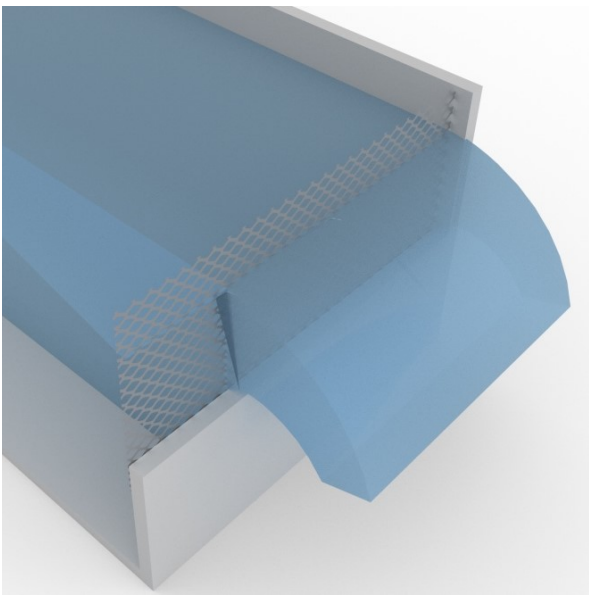


Figure 8.1. Vertical mounted screen.

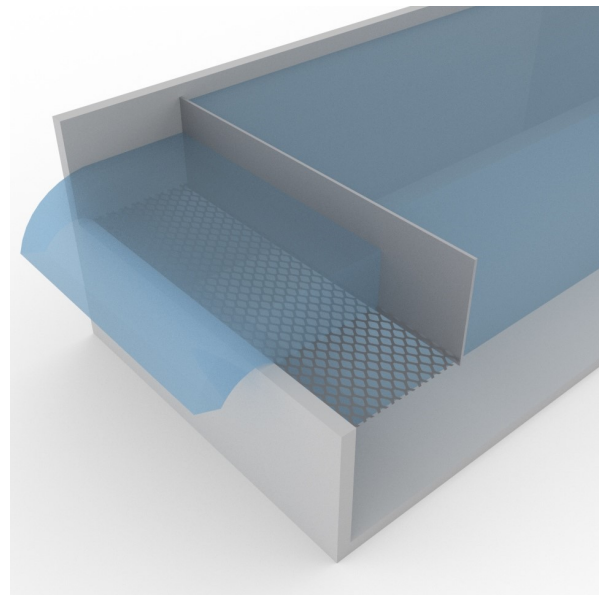


Figure 8.2. Horizontal mounted screen.

The vertical mounted screen is characterized by its effective area depending on the water level, with clogging typically occurring gradually from the bottom and up. The effective screen area of horizontal mounted screens is independent of the water level, and the screen is expected to be clogging evenly over the whole area. Horizontal screens can cover the whole area of the CSO structure, or can be mounted in combination with a baffle, reducing the screen area as shown in figure 8.2. The baffle does under these circumstances typically also function as a release weir, which will come in effect if the screen is severely clogged [WaPUG, 2006].

8.1 Hydraulic Effects of Screens

The presence of a screen within a CSO chamber introduces increased hydraulic resistance to the flow, resulting in a pressure loss. The pressure loss can be calculated knowing the hydraulic resistance of the screen using equation 8.1.

$$\Delta H = \zeta \cdot \frac{v^2}{2 \cdot g} \quad (8.1)$$

where ΔH is the loss of pressure (m), ζ is the hydraulic resistance (-), v is the velocity ($\text{m} \cdot \text{s}^{-1}$) and g is the gravitational acceleration ($\text{m} \cdot \text{s}^{-2}$).

Lots of research have been conducted describing the resistance of screens in pressurised flow systems eg. by Idelchik [1960]. It is hypothesised that most of the same theories developed for pressurised systems can be transferred to free surface flows without the introduction of significant errors. For non-clogged screens the hydraulic resistance can be estimated based on the geometry of the screen. If the thickness of the screen is small compared to the grid size of the screen, the screen can effectively be seen as a grid of small sharp orifices, and the resistance can therefore be calculated as such - see equation 8.2 [Idelchik, 1960]:

$$\zeta = (\sqrt{\zeta'} \cdot (1 - f)^{0.375} + 1 - f)^2 \cdot \frac{1}{f^2} \quad (8.2)$$

ζ is the screens coefficient of hydraulic resistance, f is the free surface area fraction. ζ' depends on the geometry of the screen, and is effectively the coefficient of hydraulic resistance of the inlet to one of the orifices. If the grid of the screen are sharp 90 degree holes ζ' equals 0.5. However, if the orifices are beveled, the coefficient is smaller, and deepens on the angle of the bevel [Idelchik, 1960].

Equation 8.2 is valid for screens where the thickness is significant smaller than grid size. The formula is valid for: $\frac{l}{d} < 0.015$, where l is the thickness of the screen (m), and d is the hydraulic diameter of the grid openings (m).

For screens with a thickness that makes equation 8.2 inapplicable, the resistance along the thickness of the screen has to be taken into account. For screens made of bar gratings the resistance can be calculated as explained in appendix E.

Vertical screens

As the water passes through the vertical screen mounted above the weir, it is hypothesised that the pressure loss is only affecting the acceleration of the water, and that the thickness of the screen is too small to affect the effective water level. Introducing the pressure loss of equation 8.1 in the weir equation, the following altered equation is derived:

$$q = \frac{2}{3} \cdot C_d \cdot \sqrt{2 \cdot g} \cdot \sqrt{h - \zeta \cdot \frac{q^2}{2 \cdot g \cdot h^2}} \cdot h \quad (8.3)$$

Where q is the flow over the weir per unit of length ($\text{m}^3 \cdot \text{s}^{-1}$). The equation has been shown using the discharge coefficient C_d instead of the weir coefficient previously used.

Equation 8.3 is based on the assumption that the water level at the weir and the water level measured is the same. Due to the curvature of the water surface close to the screen this is not exactly the case. However, the resistance of the screen will significantly reduce the curvature of the water table upstream the weir, and the error will therefore decrease, as the resistance increases. The above equation can be simplified into:

$$q = \frac{2}{3} \cdot C_d^* \cdot \sqrt{2 \cdot g} \cdot h^{1.5} \quad (8.4)$$

Where C_d^* is the effective weir coefficient for the screen equipped weir:

$$C_d^* = \frac{1}{\sqrt{\frac{1}{C_d^2} + \zeta}} \quad (8.5)$$

Measuring the weir coefficient of a reference weir and the weir with a screen equipped, the hydraulic resistance of the screen can also be estimated as:

$$\zeta = \frac{1}{C_d^{*2}} - \frac{1}{C_d^2} \quad (8.6)$$

Horizontal screens

For the horizontal screen, how one should handle the screen depends on the location where the water level is being measured. If the water level is measured above the screen, which is likely the case when the screen fully covers the surface, the effect of the screen can be effectively ignored. However, if the measurement is taken upstream of the screen, which is typically the case with partially covering horizontal screens, the effect needs to be considered. It is hypothesized that in this scenario, the screen affects both the water pressure and the cross-sectional area of the nappe. The weir equation has been modified as shown equation 8.7.

$$q = \frac{2}{3} \cdot C_d \cdot \sqrt{2 \cdot g} \cdot \left(h - \zeta \cdot \frac{q^2}{2 \cdot g \cdot L_s^2} \right)^{1,5} \quad (8.7)$$

Where L_s is screen length (m). Equation 8.7 is however too complex for the flow to be isolated as in equation 8.4. The weir flow can however quite easily be solved iteratively.

8.2 CFD Model - Screens

To examine the hypothesized equation 8.4 and 8.7, both types of screens have been implemented in a CFD model.

As the geometry of the screen typically is too fine to accurately be described in the CFD model without unreasonable computation times, the effect of the screen instead has to be approximated within the model. One option to do so is to use a porous region. This feature induces a pressure drop by implementing a sink term into the momentum term of the Navier-Stokes equations. The pressure drop is calculated from the Forchheimer equation [Siemens Industry Software, 2020]:

$$\Delta P = A \cdot v + B \cdot v^2 \quad (8.8)$$

Where ΔP is the pressure drop per unit of length ($\text{Pa} \cdot \text{m}^{-1}$), A is the viscous resistance ($\text{kg} \cdot \text{m}^{-3} \cdot \text{s}^{-1}$) and depends on the permeability of the material as well as the viscosity of the fluid. B is the inertia resistance ($\text{kg} \cdot \text{m}^{-4}$) which corresponds to the hydraulic resistance. B however also depends on the density of the fluid.

By introducing a porous region, the need to model the geometry of the screen can be avoided. However, the space occupied by the screen still needs to be incorporated into the mesh. For an accurate modelling of the screen, the mesh size should therefore not exceed the thickness of the screen. As this is undesirable, when dealing with screens of small thicknesses, the porous region can be artificially enlarged to reduce the required spatial resolution. When doing so, the resistance of the region has to be adjusted since it now introduces the resistance over a greater distance. The relationship between the coefficient of hydraulic resistance and the resistance constant introduced in the model has been presented in equation 8.9.

$$B = \frac{1}{2} \cdot \zeta \cdot \frac{\rho}{L} \quad (8.9)$$

Where ρ is the density of the fluid ($\text{kg} \cdot \text{m}^{-3}$), L is the thickness of the porous region introduced in the model (m). The viscous resistance (A) has been set to 0, as viscous effects are neglected.

The region has been set to have a depth of 2 cm equal to the base mesh size used in the model. However a quick analysis using a region of 4 and 6 cm showed no differences. The region has been placed upstream the weir, however no difference on the weir coefficient where seen, when the region was placed downstream the weir.

To enable direct comparison, the geometry of weir in the experimental setup were used in the model of the vertical mounted screen. The geometry as well as the boundary conditions has been shown in figure 8.3:

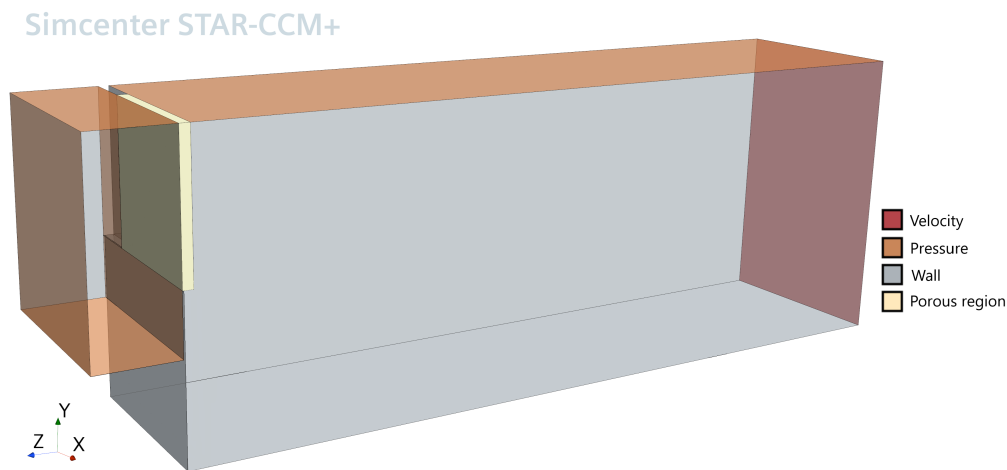


Figure 8.3. The geometry of the vertical screen CFD model. The boundary conditions of the model has been illustrated by color. The front side has not been shown, however it has been modelled as a symmetry plane to reduce computation time.

6 different hydraulic resistances has been simulated at two different flow rates, to ensure that any effects observed were independent of the flow rate.

The horizontal screen has been located just below the crest over the whole width of the channel. To simplify the geometry, the side contraptions of the weir were removed. To accommodate for this, an additional pressure boundary were included on the downstream side of the weir to ensure a proper ventilation of the nappe. A range of hydraulic resistances were simulated for 5 different screen lengths. The resistances used were adjusted based on the screen length, to ensure a build up of water large enough to securely determine any effects. The geometry of the CFD model of the horizontal mounted screen has been shown in figure 8.4.

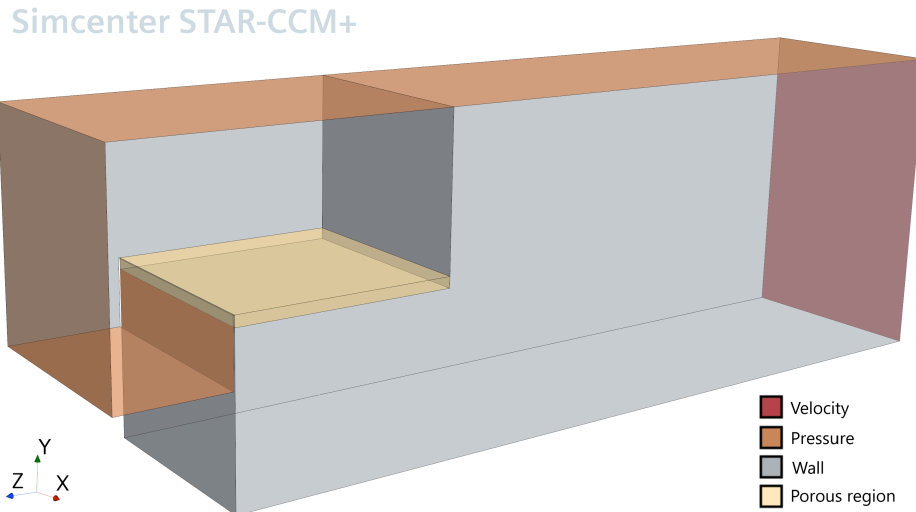


Figure 8.4. The geometry of the horizontal screen CFD model. The boundary conditions of the model has been illustrated by color. The front side has not been shown, however it has been modelled as a symmetry plane to reduce computation time.

The integration of a porous region were found to make the model somewhat more unstable. To accommodate for this, the resistance were increase gradually over a period of 10 simulated seconds using a time step of 0.01 seconds. From here on the simulation ran until convergence keeping the resistance constant. At convergence, the resistance where then again increased over a period of 10 seconds until the next specified resistance was attained.

8.3 Screens - Results

Vertical screen

To access the accuracy and validity of the hypothesized equation 8.4. The hydraulic resistance implemented in the porous region of the CFD model of the vertical screen has been plotted against the calculated resistance using equation 8.6. A regression between the predicted and the actual hydraulic resistance as well as a plot of the relative difference has been shown in figure 8.5 and 8.6.

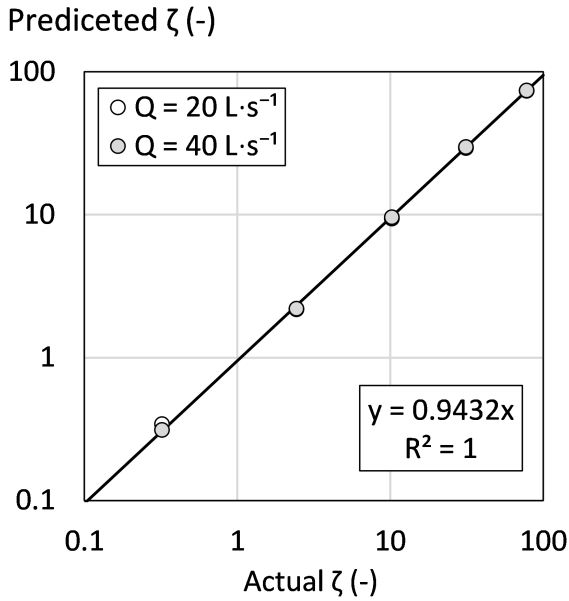


Figure 8.5. Correlation between the predicted hydraulic resistance using equation 8.6, and the actual hydraulic resistance used as input in the model.

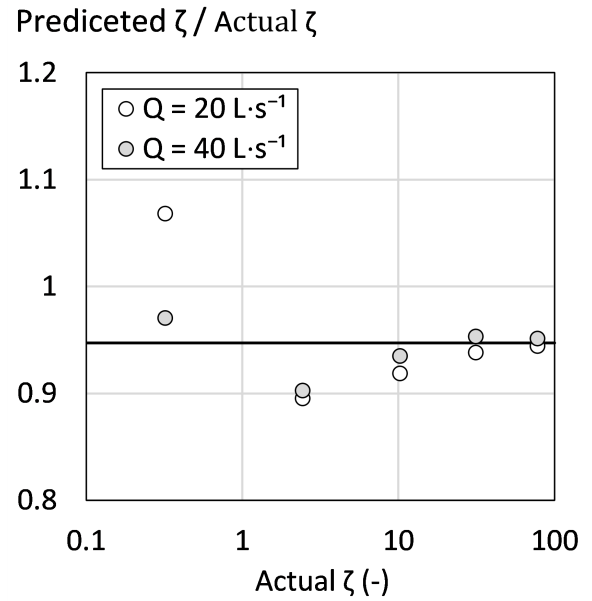


Figure 8.6. Ratio between the predicted hydraulic resistance and the actual hydraulic resistance.

The calculated weir coefficients from the laboratory experiment with the vertical screen attached to the weir have been shown in table 8.2. The weir coefficients have been determined for different flow rates with the clean screen attached. The weir coefficients have been converted to a hydraulic resistance using equation 8.6.

Table 8.2. Laboratory results of the screen equipped weir.

h (cm)	Q (L · s ⁻¹)	C (-)	ζ (-)
3,9	7,5	0,33	1,35
4,9	10,0	0,33	1,54
5,7	13,1	0,35	1,03
6,3	15,6	0,36	0,87
6,4	15,2	0,34	1,14
6,3	14,8	0,34	1,26

The average hydraulic resistance has been shown together with the standard deviation in table 8.3. The calculated hydraulic resistance has been shown together with two theoretical calculated resistance based on the geometry of the screen used. The calculations have been shown in appendix F.

Table 8.3. Comparison of the measured hydraulic resistance of the screen and the calculated values based on the work of Idelchik [1960].

Measured	Theoretical orifice	Theoretical wire
1.21 ± 0.22	1.68	1.11

The weir coefficients for the clogged screen has been shown in table 8.4 for the 5 different degrees of clogging:

Table 8.4. Laboratory results of the screen equipped weir at different degrees of artificial clogging.

Clogging fraction	h (cm)	Q (L · s ⁻¹)	C (-)	ζ (-)
0,65	6,0	3,5	0,09	58,8
0,55	6,2	5,2	0,12	27,6
0,40	6,5	7,5	0,16	14,1
0,27	6,4	10,1	0,23	6,1
0,13	6,3	12,7	0,29	2,64

The measured hydraulic resistance has been shown in figure 8.7 together with the theoretical value from equation 8.2. The theoretical graphs has been shown assuming sharp edges of the grid ($\zeta'=0.5$) and beveled edges ($\zeta'=0.18$).

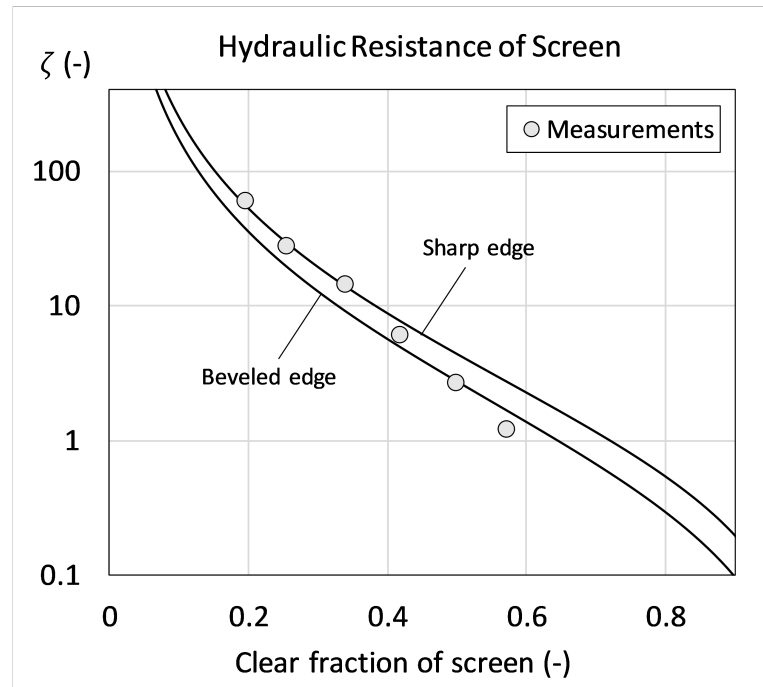


Figure 8.7. Hydraulic resistance of the screen, measurements and two different literature formulas as a function of the clear fraction of the screen (f).

Using the relationship of equation 8.5 the weir coefficient has been calculated and the results are shown as a function of the clogging degree in figure 8.8.

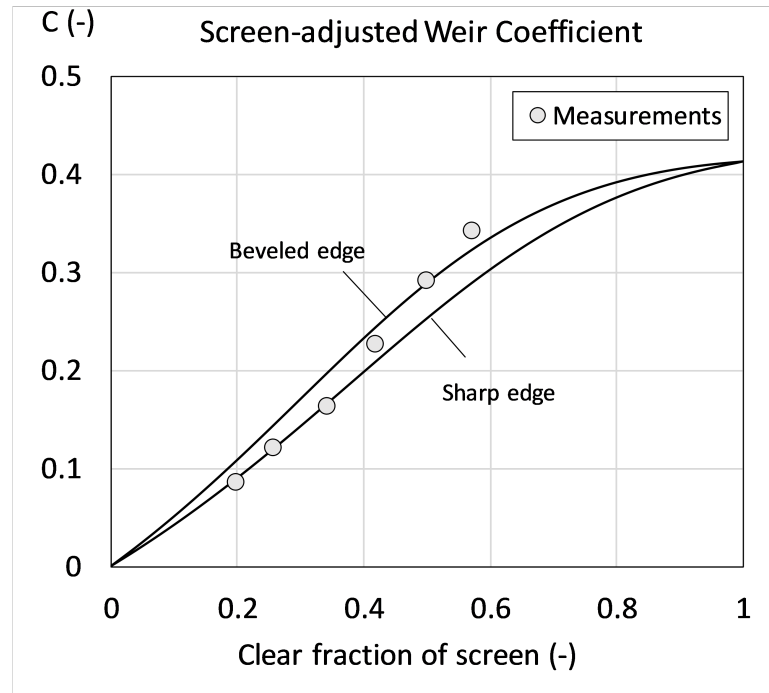


Figure 8.8. Weir coefficient of the screen used in the laboratory as a function of the clear fraction of the screen (f). Shown both for the measurements and for the two literature formulas.

Horizontal screen

As explained earlier, the hydraulic resistance of a horizontal screen cannot directly be related to the weir coefficient as is the case for the vertical screen. Instead it is hypothesised that the flow can be estimated using equation 8.7. The ratio between the flow rate implemented in the CFD model of the horizontal screen and the flow rate calculated using equation 8.7 have been plotted for two different weir configurations in figure 8.9 and 8.10. Three additional configurations have been shown in G.

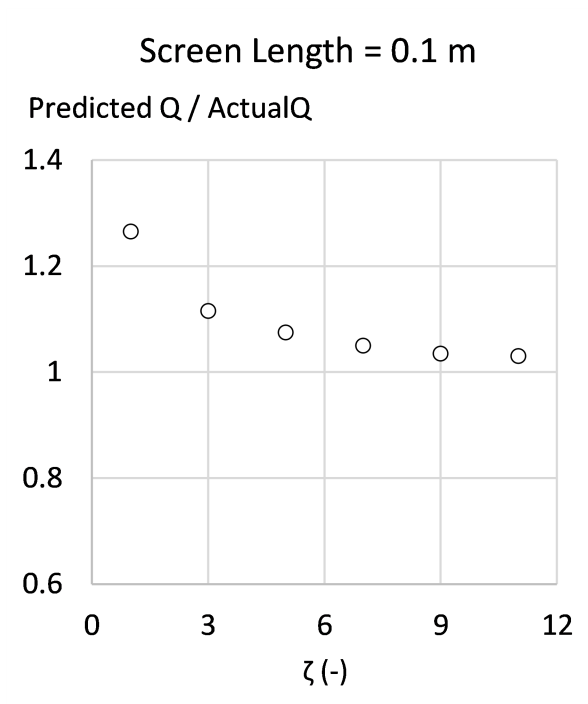


Figure 8.9. Ratio between the predicted flow and the modelled flow as a function of the hydraulic resistance of the screen using a screen length of 0.1 m

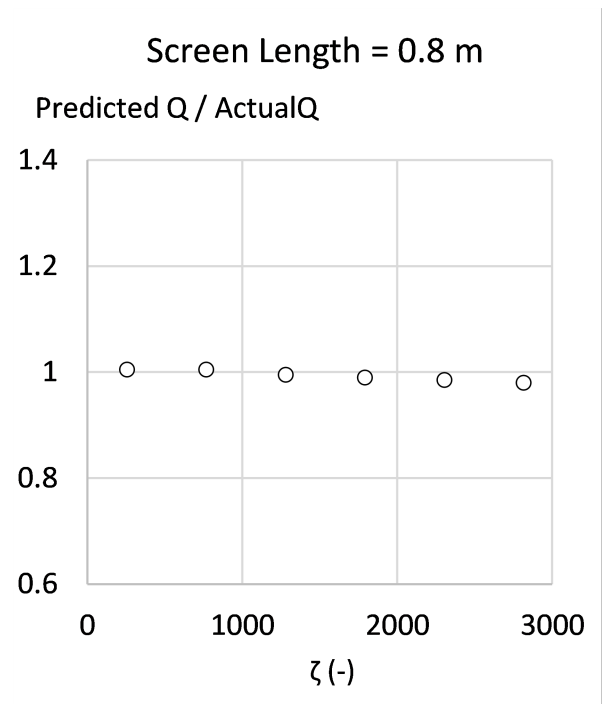


Figure 8.10. Ratio between the predicted flow and the modelled flow as a function of the hydraulic resistance of the screen using a screen length of 0.8 m

As it can be seen from figure 8.9 and figure 8.10 the ratio is close to 1 in most cases. At low hydraulic resistance in combination with small screen lengths equation 8.7 overestimates the flow. This is due to the screen length being so narrow, that opening itself induces a significant hydraulic resistance, which is not taken into account.

Submersion of the Weir 9

Under intense rainfall events, the discharge capacity of the CSO structure can become limited by the capacity of the discharge pipe leading water from the CSO chamber to the receiving water body. Under these conditions, water builds up downstream the weir, and the weir is said to be submerged. When this happens, the characteristics of the rating curve changes dramatically. Moreover, the water level that governs the flow has shifted downstream the weir. The upstream water level can however still be related to the downstream water level using the equation for the flow over a submerged weir. The flow over a submerged weir can be estimated by dividing the flow into two parts: a free discharge over the downstream level (Q_1), and a submerged discharge below the downstream head (Q_2), as firstly proposed by [Dubuat, 1816].

$$Q_1 = \frac{2}{3} \cdot C_d \cdot b \cdot \sqrt{2 \cdot g} \cdot (h_1 - h_2)^{1.5} \quad (9.1)$$

$$Q_2 = C_d \cdot b \cdot h_2 \cdot \sqrt{2 \cdot g \cdot (h_1 - h_2)} \quad (9.2)$$

Where C_d is the discharge coefficient (-), b is the length of the weir (m), g is gravitational acceleration ($\text{m} \cdot \text{s}^{-2}$), h_1 is the upstream water level (m) and h_2 is the downstream water level (m).

An illustration of a submerged weir has been shown in figure 9.1.

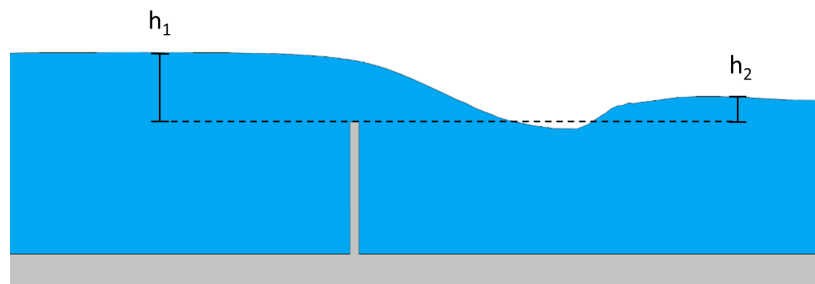


Figure 9.1. Illustration of a submerged weir.

A study investigating CFD determined rating curves of two CSO structures by Fach et al. [2008] showed that the flow of both structures became limited by the outlet, and that the flow under these conditions could be described as a controlled outflow using the same formula as for an orifice [Fach et al., 2008]:

$$Q = k \cdot A \cdot \sqrt{2 \cdot g \cdot h} \quad (9.3)$$

Where k is the discharge coefficient of the orifice (here denoted k not to confuse with the discharge coefficient of a weir), A is the area of the orifice (m^2) and h is the head above the center of the orifice (m).

The coefficient k from equation 9.3 however poses a problem, as it was found to be outside typical literature values. Furthermore, Fach et al. [2008] neglects the effect of the pipe in its full length and only includes the effect of the pipe inlet.

An analysis of the placement of 94 combined sewer overflow (CSO) structures from Odense Municipality, Denmark, revealed that the average distance from a CSO structure to the discharge location is approximately 200 meters. However, the majority of CSO structures have discharge pipe lengths below 100 meters. Therefore, it does not seem reasonable to assume that the formula for an orifice is valid. The distribution of the discharge pipe lengths is illustrated in Figure 9.2.

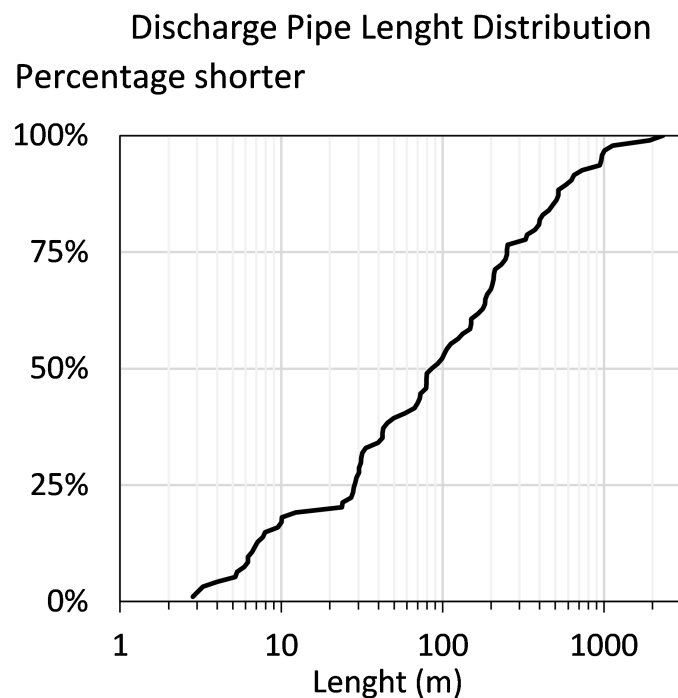


Figure 9.2. Distribution of distances between the CSO structure and the point of discharge, which is assumed to be approximately the same as the length of the discharge pipe.

Whether or not the discharge pipe becomes limiting depends on the size and the slope of the pipe as well as the height of the weir above the inlet to the discharge pipe. It is not suspected that all CSO structures regularly becomes limited. However, due to the dramatic change of the rating curve, the error of neglecting the capacity of the outlet pipe can be severe.

9.1 Modelling the Downstream Network

To predict the rating curve when the discharge pipe becomes limiting and the weir submerges, a simple hydraulic model has been built. As shown in figure 9.2 the typical discharge pipe is a few hundred meters, meaning that any changes in the upstream water level will quite rapidly propagate downstream. Therefore it is assumed that the use of a stationary model is reasonable. Alternatively a dynamic 1 D model could be applied, however this would not allow for the design of a single rating curve, as a range of flows could exist at the same water level. The length of the discharge pipes are however assumed to be large enough for fully developed flow and thereby natural depth to emerge.

The model relies on the downstream boundary condition to be known. Two different boundary conditions can exist; the pipe can be located above the water table of the receiving waterbody, and the pipe is freely discharging, or the pipe exit can be completely or partly below water.

Knowing the downstream boundary condition, the upstream water level will be calculated at different flow rates.

At each flowrate we determine whether the pipe is full and pressurised or we have to do with free surface flow. This is done by comparing the flowrate to the natural flow at full capacity, calculated using the manning equation 9.4 [Winther et al., 2016].

$$Q = A \cdot M \cdot R^{2/3} \cdot \sqrt{I_S} \quad (9.4)$$

Where Q is the flowrate ($\text{m}^3 \cdot \text{s}^{-1}$), A is the area of the full pipe (m^2), M is the manning number ($\text{m}^{1/3} \cdot \text{s}^{-1}$), R is the hydraulic radius of the full pipe (m) and I_S is the slope of the pipe (-). If the flowrate is above the natural flow at full capacity, the energy gradient is steeper than the slope of the pipe, and it can be calculated using the simplified version of the darcy-weisbach equation:

$$I_e = \frac{Q}{Q_f} \cdot I_S \quad (9.5)$$

Where I_e is the energy gradient (-) and O_f is the natural flow at full capacity.

From this the pressure loss in the pipe due to friction can be calculated:

$$\Delta h_{fr} = I_e \cdot L \quad (9.6)$$

Where Δh_{fr} is the pressure loss due to friction (m) and L is the length of the pipe.

If the flowrate is below the natural flow. The pipe is only partially full, and the slope of the energy gradient equals the slope of the water surface, the pressure loss within the pipe is therefore 0. The water depth within the pipe, can be estimated using the Bretting equation [Winther et al., 2016]:

$$\frac{Q}{Q_f} = 0.46 - 0.5 \cdot \cos\left(\pi \cdot \frac{y}{d}\right) + 0.04 \cdot \cos\left(2 \cdot \pi \cdot \frac{y}{d}\right) \quad (9.7)$$

Where y is the water depth in the center of the pipe (m) and d is the diameter of the pipe (m).

Using the water depth, the cross-sectional area and the velocity can be calculated.

At the inlet of the pipe the water accelerates, and a local loss happens leading to a pressure drop. The pressure drop is calculated as:

$$\Delta h_{loc} = (\zeta_{loc} + f) \cdot \frac{v^2}{2 \cdot g} \quad (9.8)$$

Where Δh_{loc} is the local pressure loss, ζ is the hydraulic resistance coefficient (-) typically set to 0.5 [Idelchik, 1960]. f is a number between 0 and 1 that accounts for the acceleration of the water. If the water is assumed to be completely still within the CSO chamber the value is 1. The value is 0 if a perfect jet exist within the chamber from the inlet to the outlet, and no kinetic energy is lost within the chamber. As long the water have to pass over a free flowing weir, it is suspect that all the energy is lost, and the value is assumed to be 1. However, the value is expected to decreases as the weir submerges.

The water level within the chamber can then be calculated:

$$h = y + \Delta h_{fr} + \Delta h_{loc} \quad (9.9)$$

Where h is the water level within the chamber downstream the weir, and y is the water depth within the pipe.

If the water level is below the weir edge, we have a free weir, and the upstream water level is unaffected by the downstream pipe, the weir equation is then valid. If the water level is above the weir edge, the weir is said to be submerged. The flow over a submerged weir can be described by the upstream and downstream water level using equation 9.1 and 9.2. Using a simple solver, we can then calculate the water level upstream the weir.

5 different real life CSO structures were provided by 3 danish water companies; Aarhus vand, Vandcenter syd, and Novafos. Rating curves have been determined for each of the structures using CFD modelling, and has been compared with the predicted rating curves using the Froude number - weir coefficient relationship previously derived. Furthermore the capacity of the discharge pipe has been assessed and the altered rating curve has been determined.

If water level data and flow data are available for the considered CSO structure, the rating curves will be compared to the collected data. Additionally, annual discharge loads will be calculated and compared to the reported loads in the Danish database for CSO discharges, known as the PULS database. The discharge loads from the PULS database are publicly available [Danmarks Miljøportal, 2023].

The CFD models have been set up in the same manner as explained in section 5. However, in some cases adaptations had to be made to model the system downstream the weir adequately. This will be further explained for each individual structure.

10.1 Kalkværksvej

A side weir CSO structure located at Kalkværksvej Aarhus Denmark were provided by Aarhus Vand. The CSO chamber is equipped with a horizontal screen covering the whole water surface (not shown in figure 10.1). Furthermore the structure is equipped with a gate to regulate the flow through the downstream pipe. The weir has a thickness of 0.1 m, and has no side contractions. Furthermore the downstream side of the crest is curved, and most closely resembles an ogee crested weir. Downstream the weir the water have to pass through a 25 x 25 cm square opening expected to function like a orifice, before merging with a storm water pipe. The geometry of the CSO structure has been shown in figure 10.1.

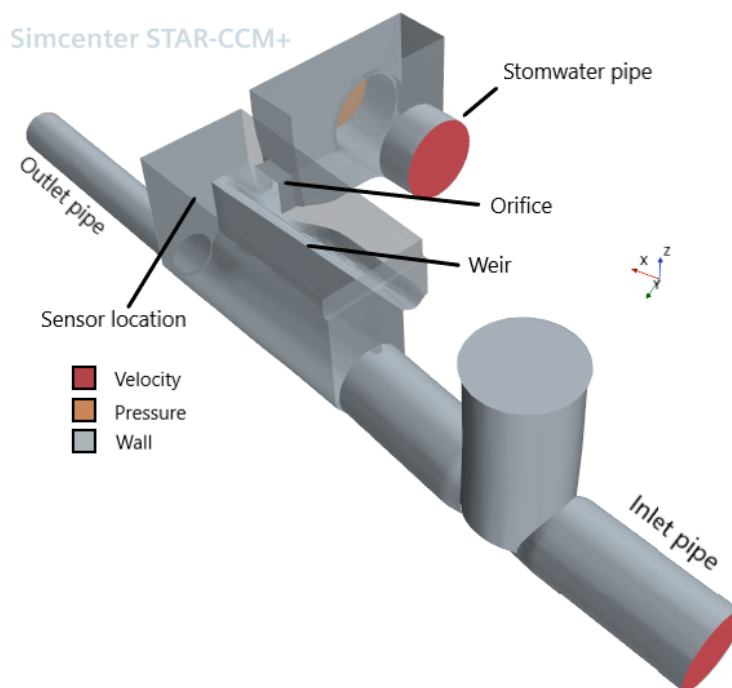


Figure 10.1. Illustration of the structure with applied boundary conditions.

Two CFD simulations have been conducted, one where the downstream gate has been assumed to be closed, resulting in no downstream flow, and one where natural flow velocity at full capacity has been assumed ($688 \text{ L} \cdot \text{s}^{-1}$). Due to the small size of the chamber and therefore the water levels quick response to changes in inflow and outflow conditions, the rating curves have been determined based of a single transient simulation, where the inflow gradually has been increased with 10 l/s per second.

A variable timestep has been used in combination with the implementation of implicit multisteping. This has been done to ensure the water-air interface stays well defined downstream the weir. This is done as the orifice downstream the weir is expected also to affect the raing curve. The implicit multi-step splits the tracking of the volume fraction of water into multiple steps, ensuring that the surface stays sharp - also at high water velocities [Siemens Industry Software, 2020].

Even though the structure is categorized as a side weir, calculation of the dimensionless parameters of the structure has shown that some of the parameters fall outside the range of the randomly generated structures analysed preciously. The relationship between the Froude number and the weir coffined can therefore not be applied directly. Instead the predicted rating curve has been based of the discharge coefficient for a short crested weir using the equation presented in figure 6.4. The weir coefficient has then been adjusted using the model coefficient (c_m) of the simple side weir of figure 7.17. The downstream system has been modelled as an orifice using equation 9.3 and a standard

k-value of 0.6 according to [Akan and Houghtalen, 2003].

In table 10.1 the predicted and modelled weir coefficients have been shown for the scenario where the gate is closed, and the downstream flow is 0. In table 10.2 the coefficients have been shown for the scenario where the gate is open, and the flow through the outlet pipe equals the natural flow at full capacity.

Table 10.1. Estimated weir coefficient when the gate is closed.

h (cm)	Predicted	CFD
2	0.35	0.37
4	0.36	0.36
8	0.37	0.34

Table 10.2. Estimated weir coefficient when the gate is open.

h (cm)	Predicted	CFD
2	0.28	0.33
4	0.29	0.28
8	0.30	0.33

The predicted rating curve for the CSO structure at Kalkværksvej has been shown in figure 10.2 along with the CFD generated rating curve and the standard weir equation. Furthermore a curve similar to the predicted rating curve has been shown, where the weir coefficient and the orifice discharge coefficient (k) has been fitted to match the CFD results. The rating curve has been based on the scenario, where the gate is closed.

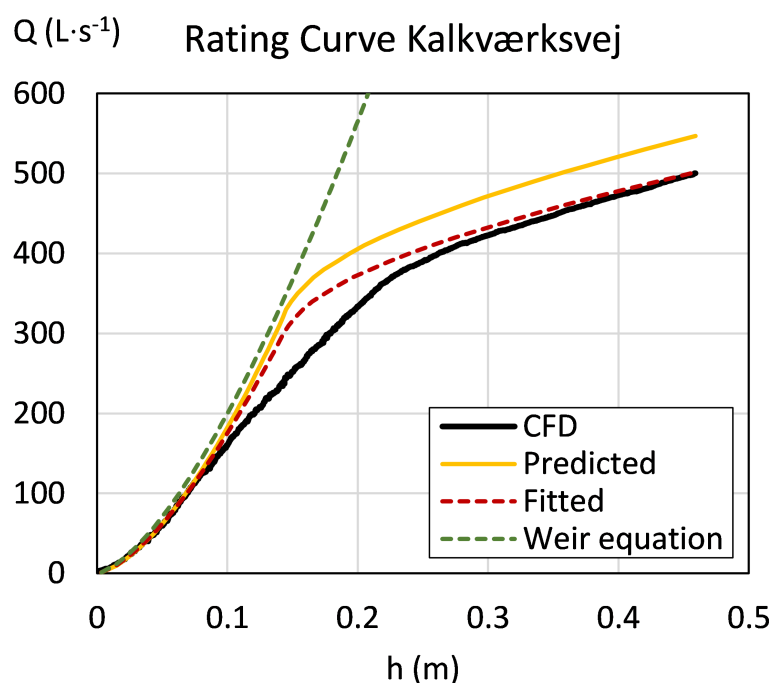


Figure 10.2. The rating curves of kalkværksvej. The Predicted rating curve has been shown alongside the rating curve from the CFD model and the standard weir equation.

The rating curve for the open-gate-scenario has been found to be very similar, and it has therefore not been shown. Only the beginning of the curve ($h < 0.1$ m) have been found to be affected by the weir coefficient. Due to this, the curves are almost similar, despite the slight difference of the weir coefficient. As it can be seen of figure 10.2 the rating curve starts deviating from the weir equation at $h = 0.1$ m. Here the weir starts to become submerged. At approximately $h = 0.22$ m the weir is totally submerged, and the rating curve instead resembles that of an orifice. The 3 different flow conditions have been shown in figure 10.2.

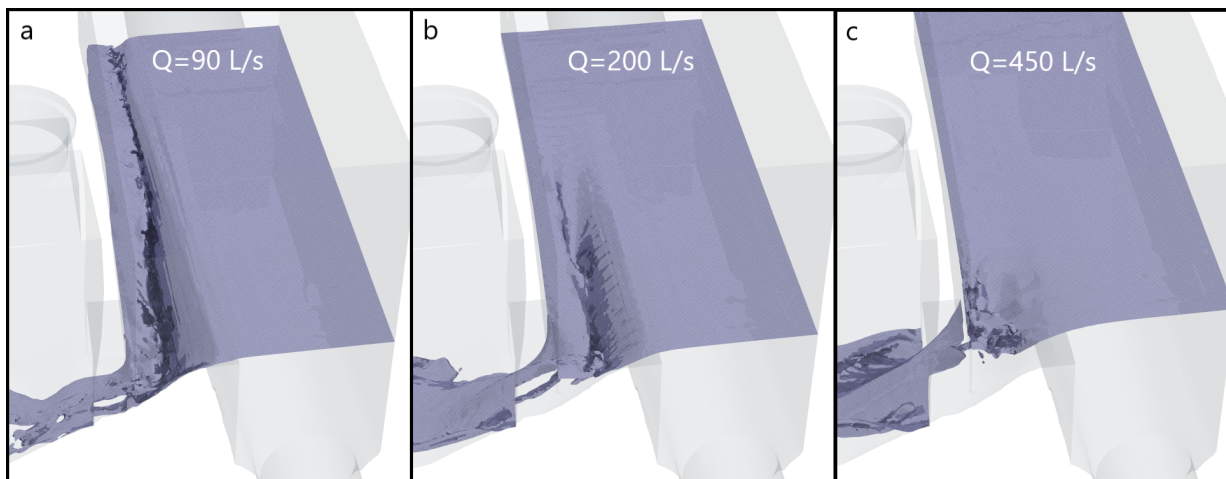


Figure 10.3. The water surface generated by the CFD model at 3 different flowrates, where the weir is flowing free (a), partly submerged (b) and fully submerged (c).

10.2 Fredtoftevej

Novafos has provided a CSO structure located at Fredtoftevej in Farum Denmark. Previously a CFD model has been made of the structure [Rambøll, 2022a]. The results from this will be used as comparison. The simulation by Rambøll did however not include the effect of the discharge pipe, and results are therefore not suspected to be identical. The CSO structure consists of two weirs. A primary weir equipped with horizontal screens which leads water to a large basin. From the basin the water is discharged to Farum Lake over a secondary weir and through a 140 meter long discharge pipe. Both weirs are classified as side weirs, however the model will only focus on the secondary weir. The secondary weir has a length of 24.75 meters, and consists of a 25 cm thick concrete crest. On the front of the concrete crest a small sharp metal plate has been attached. The metal edge increases in height along the length of the weir, from 0 cm in one end to 7 cm in the other end, ensuring a horizontal crest. The weir is therefore some combination of a sharp crested weir and a broad crested

weir, depending on the position along the weir. The CSO structure is equipped with two inlets. The geometry of the structure has been shown in figure 10.4 and the selected boundary conditions used in the CFD model have been illustrated.

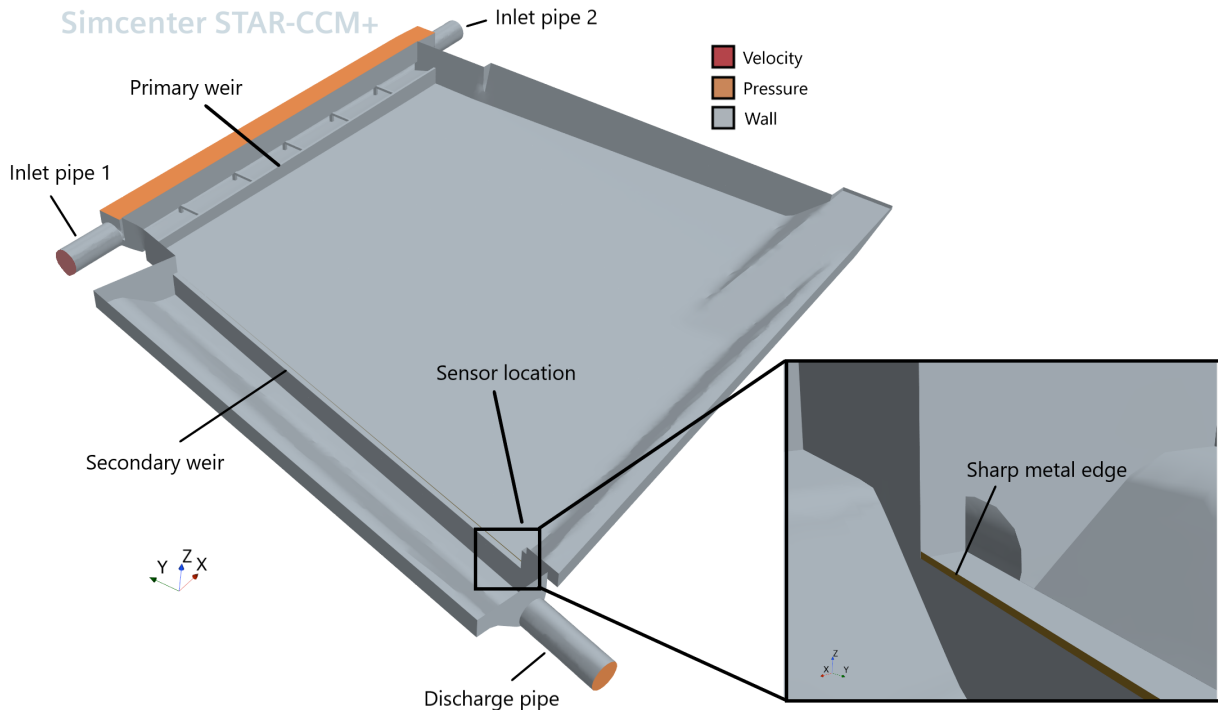


Figure 10.4. Illustration of The CSO structure at Fredtoftevej with applied boundary conditions. The top of the domain have not been shown, it has however also been modelled as a pressure boundary.

The metal plate has been modelled as an impermeable baffle to decrease the spatial resolution necessary. The screen at the primary weir has not been included in the model, as it is suspected only to have very little effect on the flow over the secondary weir. As the water enters the chamber through the vertical opening of the screen, any energy from the two inlet pipes is assumed to be dispersed. Therefore the f in equation 9.8 is set to equal 0 in the modelling of the discharge pipe. Only the first 4 meters of the discharge pipe has been included in the model, to decrease computation time.

Like the CSO structure at kalkværksvej, the dimensionless parameters of the structure at Fredtoftevej has been found to be outside the range of the randomly generated structures previously analysed. Therefore the Froude number cannot in itself predict the weir coefficient. The prediction of the weir coefficient is instead based on the ideal weir coefficient (C_i) of a sharp crested weir (due to the metal edge) in combination with the model coefficient (C_m) of a ideal side weir.

The weir coefficient from the CFD model has been shown in 10.3 together with the predicted coefficient. The data presented in Rambøll [2022a] has been shown as well.

Table 10.3. The CFD-determined weir coefficients presented alongside the predicted weir coefficients at five different flow rates.

flow	CFD	Rambøll	Fr	Predicted
500	0.46	-	0.02	0.41
1000	0.48	-	0.04	0.40
2000	0.39	0.36	0.06	0.40
2500	0.37	0.36	0.08	0.39
4000	0.34	0.36	0.11	0.38

Figure 10.5, shows the predicted rating curve together with the results from the CFD model and that from Rambøll [2022a].

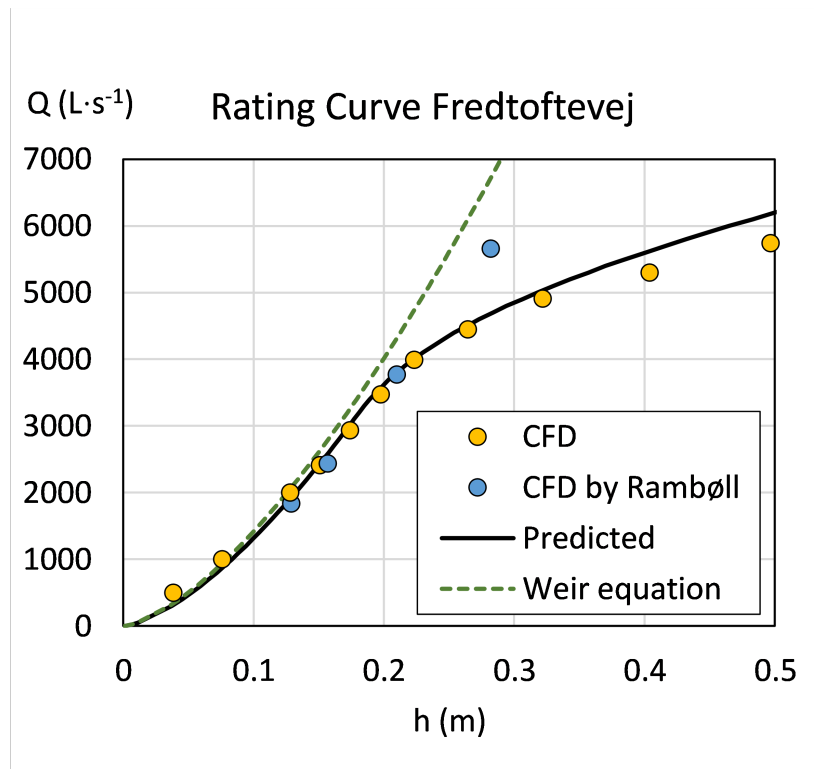


Figure 10.5. The predicted rating curve for the CSO structures at Fredtoftevej, with a 4 meter outlet pipe.

As only the first 4 meters of the discharge pipe has been included in the CFD model, the rating curve doesn't represent the real life structure. The predicted rating curve has been shown in figure 10.6 using the true discharge pipe length of 141 meters. The slope of the pipe is almost 0 and is therefore close to negligible. A free outlet has been assumed, however it is suspected, that the water level in

the Lake Farum might affect the true rating curve. The rating curve has been shown together with the measurements.

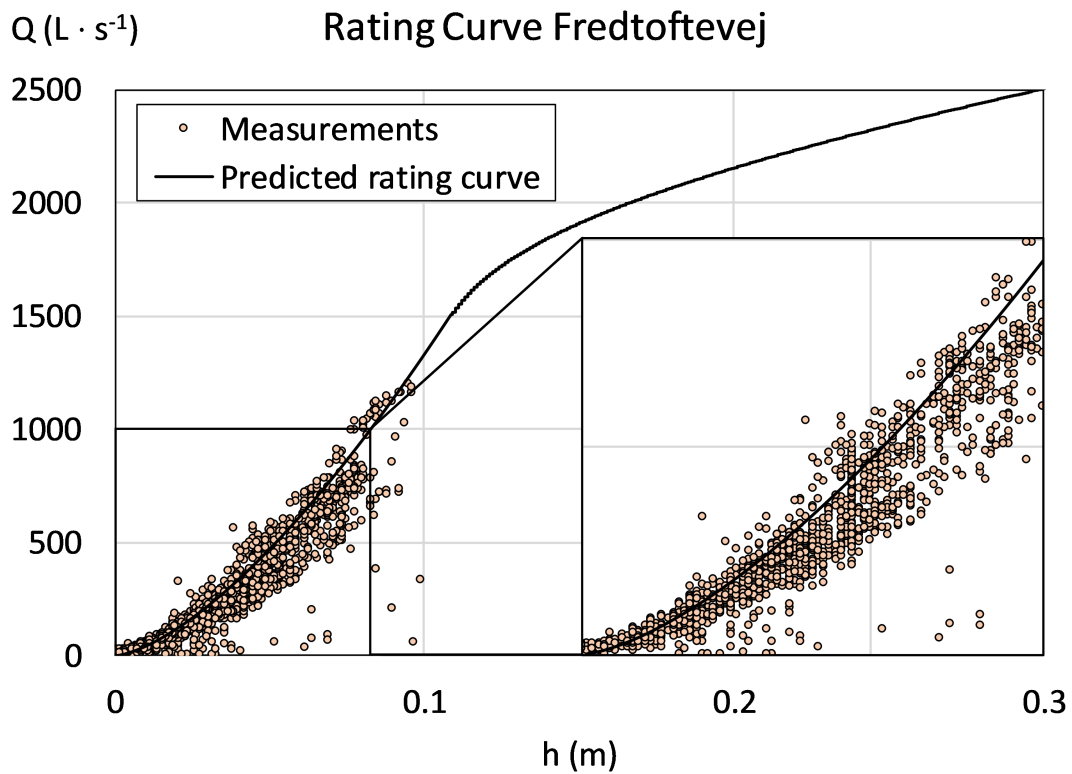


Figure 10.6. The predicted rating curve for the CSO structures at Fredtoftevej with the 141 meter discharge pipe shown alongside the real-life measurements.

Flowdata from the largest events has unfortunately not been available. However within the measurement period of June 2022 to June 2023, the water level has been measure during several large events, with the highest water level being measured at 0.202 meters. A picture of the real life structure at this event has been shown together with the water surface generated by the CFD model at a similar flowrate - see figure 10.7.

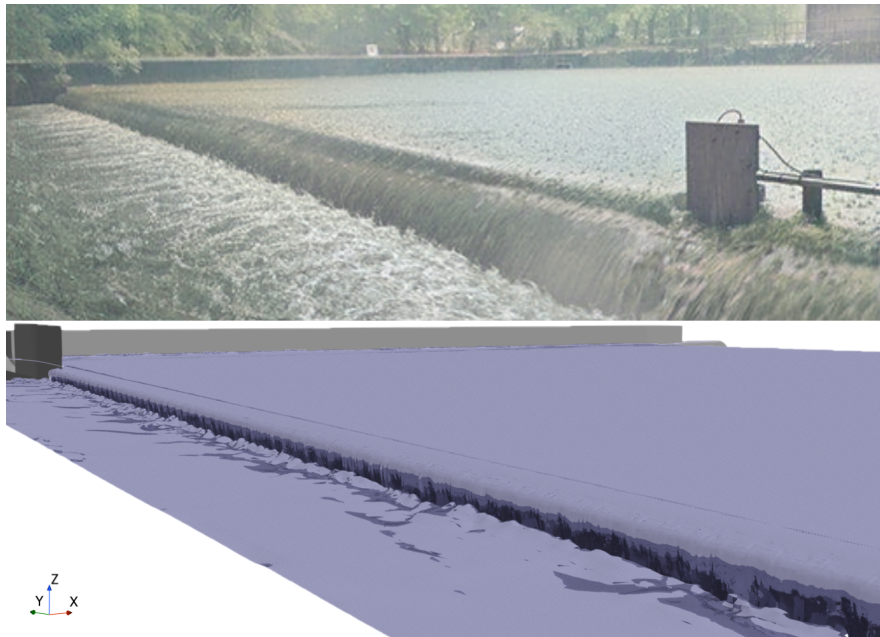


Figure 10.7. A photo tanken at the largest event in 2022 at flow of approximately 2000 l/s, and the water surface of the CFD model at the same flowrate [Sørensen, 2022].

Before the rating curve can be applied to determine the flow based on the measured water level. The water level data has to be related to the level of the weir. A method to determine the level of the crest based on the water level data has been presented in appendix D. It is estimated that the method has been able to determine the crest level with ± 0.5 cm of uncertainty.

The accumulated flow from June 2022 to June 2023 has been calculated using three different methods: the predicted rating curve, the CFD determined rating curve, and the standard weir equation with a coefficient of 0.41. Table 10.4 presents the results along with the reported data from PLUS for the year 2022. The PULS data is derived from a Mike Urban model. The predicted discharge loads are presented as ranges to account for the uncertainty of ± 0.5 cm in the crest level.

Table 10.4. The accumulated discharge loads calculated using the water level data and different rating curves, shown together with the PLUS reporting

Fredtoftevej Discharges from June 2022 to June 2023 (m^3/year)	
Weir equation	87230 (74747 - 100709)
CFD without discharge pipe	76592 (65632 - 88428)
CFD with discharge pipe	75905 (64997 - 87734)
Predicted	80652 (69098 - 93111)
Puls reporting (Mike Urban) (2022)	70000

10.3 Lindevangsvej

At Lindevangsvej located in Birkerød Denmark a small CSO structure has been provided by Novafos. Like the structure at Fredtoftevej, a CFD model has previously been made of the structure [Rambøll, 2022b]. The structure is a side weir CSO structure equipped with an inclined screen at the weir edge. In the middle of the structure a few irregularly placed boards are installed. The weir has a length of 2,13 m. The weir edge deviate from a classical weir edge, in the sense that the edge is made as an gradual raise and a sharp lowering of the floor level, most closely resembling a crump crested weir. The inlet and the discharge pipe both have diameters of 0.6 meters while the outlet pipe has a diameter of 0.2 m. The discharge pipe has a length of 57 meters and a slope of 0.32 %. A picture from within the CSO chamber has been shown in figure 10.8.



Figure 10.8. Photo taken within the CSO chamber [Rambøll, 2022b].

The discharge pipe has been included in its whole length in the CFD model as it is suspected to be limiting for the flow. The long discharge pipe however increases the computation time significantly as the number of cell increases significantly and due to changes in flow and waterlevel having to dissipate downstream the pipe, slowing down the convergence. 3 CFD simulations have been carried out, however 4 additional CFD simulations by Rambøll [2022b] have been used. In the simulations by Rambøll [2022b] the geometry of the screen has been included in the model. From the results the effect of the screen were reckoned to be negligible. The screen has therefore not been include in the CFD model carried out in this project. The resistance of the boards has been estimated as a function of the water level using the formula for the Resistance of a sharp orifice [Idelchik, 1960], and as been used in the prediction of the ratinc curve.

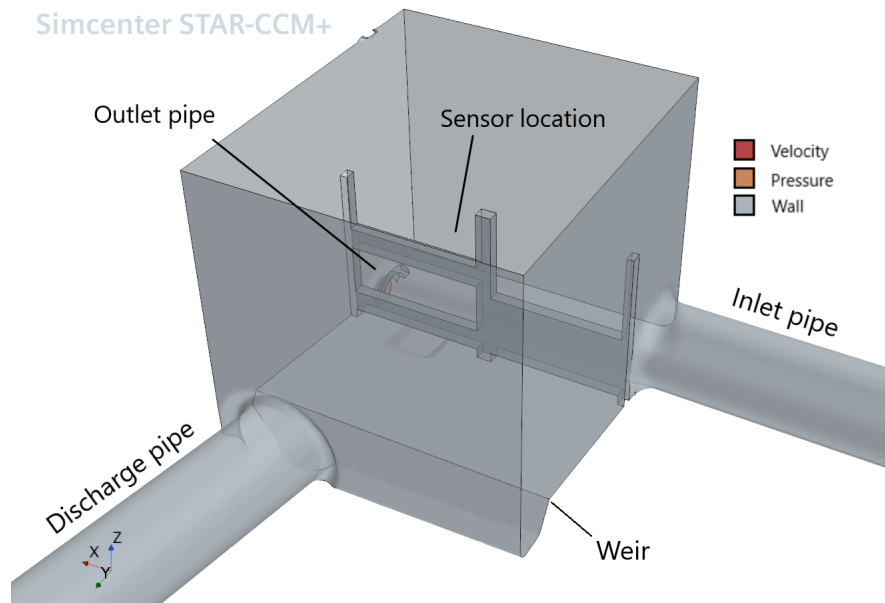


Figure 10.9. The geometry and selected boundary conditions of the CSO structure at Lindevangsvej. The screen has not been included.

The predicted rating curve of the CSO structure of Lindevangsvej has been shown in figure 10.10. The predicted rating curve has been shown twice using different values of the loss of momentum within the chamber. In the one case all of the incoming momentum is suspected to be lost within the chamber, and in the other case a perfect jet is assumed, and no energy is suspected to be lost.

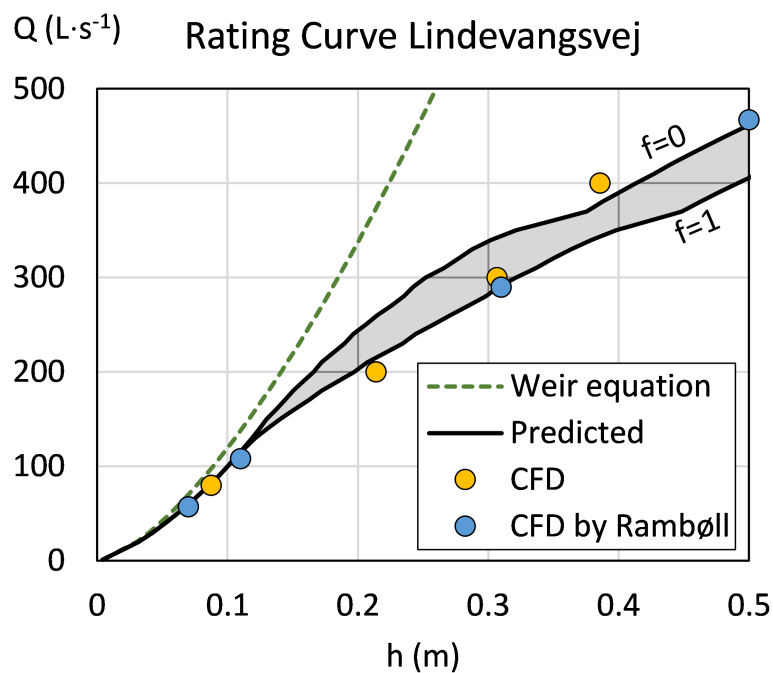


Figure 10.10. The predicted rating curves shown together with the results from the CFD modelling.

10.4 Bergsøe plads

At Bergsøe plads in Odense Denmark a CSO structure has been provided by Vandcenter Syd. The structure has 3 inlets with diameters of 0.63 m, 0.7 m and 1.1 m respectively, and only 1 outlet of with a diameter of 0.3 meters. The capacity of the outlet is therefore magnitudes lower than the inlet, leading to frequent overflow events. Two sharp crested weirs are located at an angle to the inflow. The CSO structure can therefore neither be classified as a side weir or as a stilling pond weir.

3 pipes with diameters of 0.63 m, 0.7 m and 1 m discharges the overflow into Odense River. The pipes all have lengths of 7 meters. At the river the pipes are equipped with flap valves. The large outlet is located close to the water surface of the river, and is partly drowned. The two small outlets are suspected never to be drowned. To simplify the simulation, it has been decided not to model the flap valves. This will postpone the submerging of the weir. The modelling of the flap valves is quite complex, as it includes the modelling of solid moving parts, for which reason it is considered outside the scope of this project. The geometry of the structure has been shown in figure 10.11.

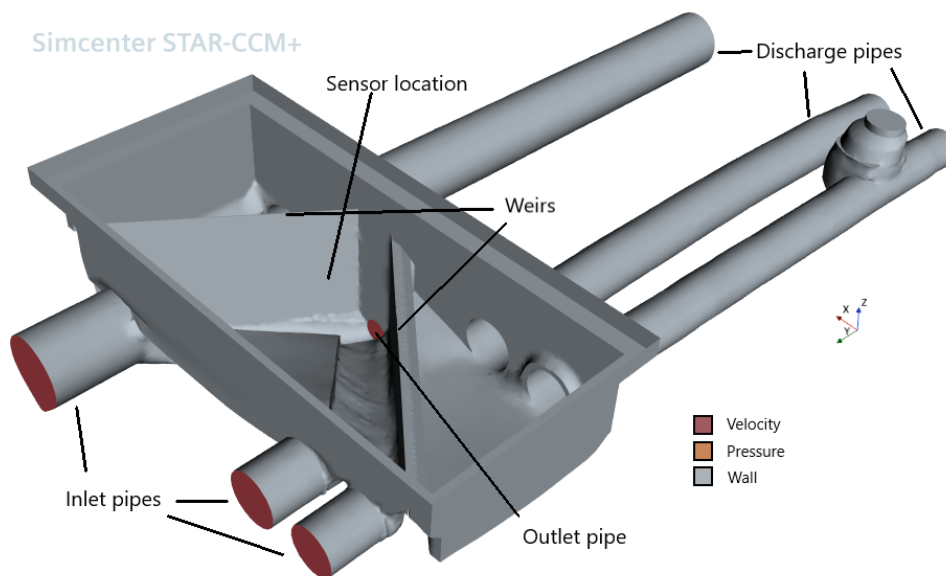


Figure 10.11. The geometry of the CSO structure from Bergsøe Plads. The boundary conditions has been shown by color. The end of the discharge pipes and the top of the domain are set as pressure boundaries.

As the structure neither resembles a side weir CSO structure or a stilling pond structure, no rating curve has been predicted for the structure based on the Froude number. As the structure however is sharp crested the predicted rating curve will be solely based of the weir coefficient of such being 0.41.

The CFD-determined rating curve has been shown together with the standard weir equation in figure 10.12.

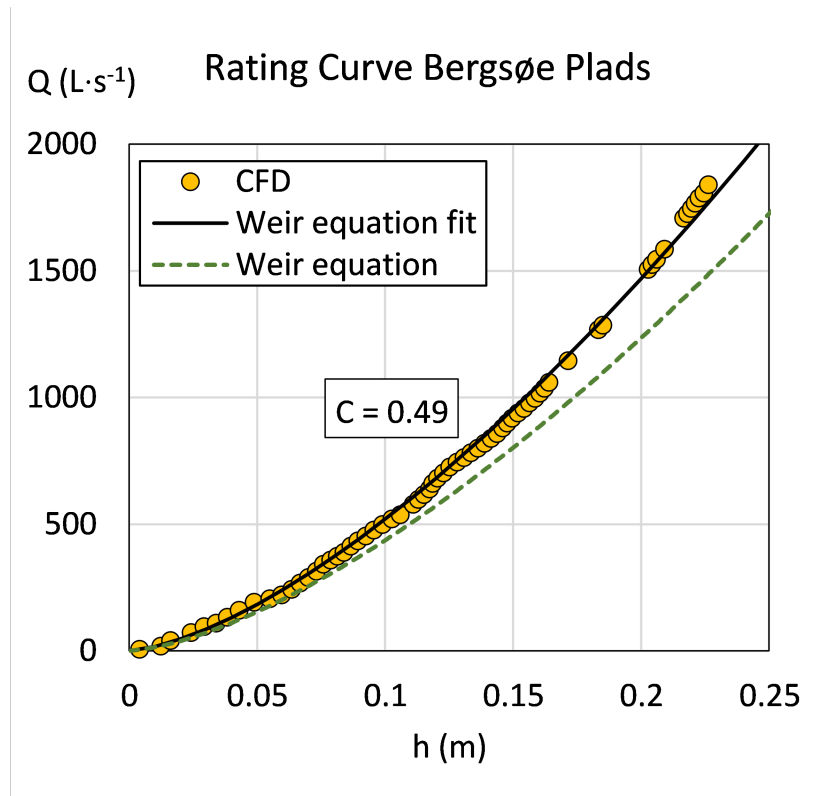


Figure 10.12. The rating curve of Bergsøe plads. Some of the datapoints are missing due to a lack of memory as the simulation was conducted.

Due to the neglect of the flap vales, the flow were never seen to be restricted by the discharge pipes. However, it is possible that this would in fact be the case, if they were taken into account. The rating curve generated by the CFD model approximately follows the weir equation with a weir coefficient of 0.49 as shown in figure 10.12.

The structure has been equipped with a water level sensor, which has been running continuously for 3 years. The accumulated annual discharges of 2020, 2021, 2022 have been estimated using the two rating curves of figure 10.12, and has been compared to the reported discharges from the PULS-database. The crest level has been determined in appendix D within a 0.5 cm uncertainty, and has been used in the estimation of the annual discharges. Furthermore the discharges have been calculated using the weir equation based of the non-adjusted crest level. The results have been presented in table 10.5.

Table 10.5. Estimated annual discharged volumes from the CSO structure at Bergsøe Plads. The PLUS data are based on urban drainage models using the MIKE Urban software.

	Bergsøes Plads Discharges (m ³ /year)		
	2020	2021	2022
Weir eq.	125155	148222	125765
Weir eq., adjusted crest	39895 (33813 - 46471)	52352 (45307 - 59923)	35097 (28856 - 41945)
CFD, adjusted crest	47679 (40411 - 55538)	62567 (54148 - 71615)	41945 (34487 - 50129)
PULS reporting (MU)	29985	46440	32026

10.5 Thulevej

The CSO structure at Thulevej located in Odense Denmark were provided by Vandcenter syd. The structure consists of a primary weir which leads water into a chamber connected to a secondary weir, which discharges the water into Stavis River. The secondary weir is equipped with a vertical screen of approximately 20 cm height. The screen consists of vertical bar gratings and has been shown in figure 10.13. Furthermore a scumboard is installed within the chamber upstream the secondary weir.



Figure 10.13. Photo of the screen at the CSO structure at Thulevej. The photo was taken after an attempted cleaning of the screen [Sørensen, 2022].

The secondary weir is 11 meters in length, and has been observed not to be perfectly horizontal. Instead, a portion of the weir has a slight slope, resulting in an approximate 3 cm height difference between the two ends of the weir. Downstream from the weir, the water enters a rainwater pipe with a steep slope of 3%. The pipe has a diameter of 0.8 m. The CSO structure has been equipped with flow sensors at the inlet and outlet as well as water level sensors in the primary channel and in the

main basin. The geometry of the structure and the boundary conditions selected has been shown in figure 10.14.

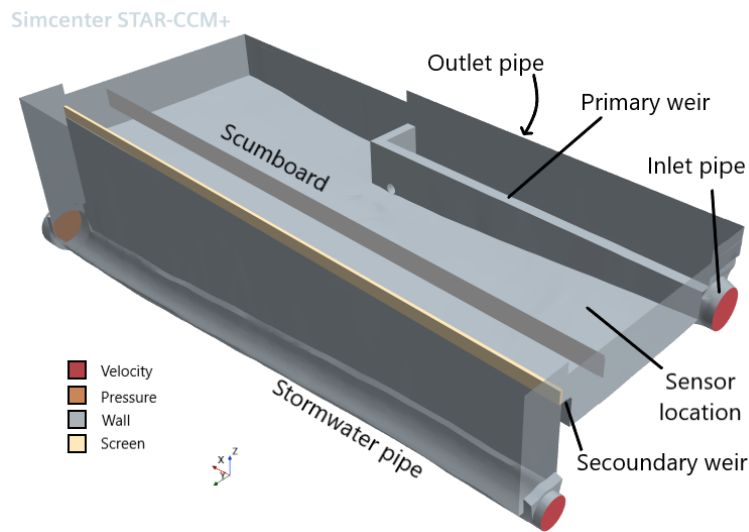


Figure 10.14. The geometry of the CSO structure at Thulevej. The top of the basin is not seen, but has been modelled as a pressure boundary.

The screen has not been included in the CFD model, however the effect will be taken into account when predicting the rating curve of the structure. The rating curve has been predicted using equation 7.4 inserting the parameters ($a=0.255$, $b=-0.25$ and $c=0.475$) estimated from appendix H based on the location of the sensor. The results of the CFD simulations has been shown in figure 10.15 together with the predicted rating curve.

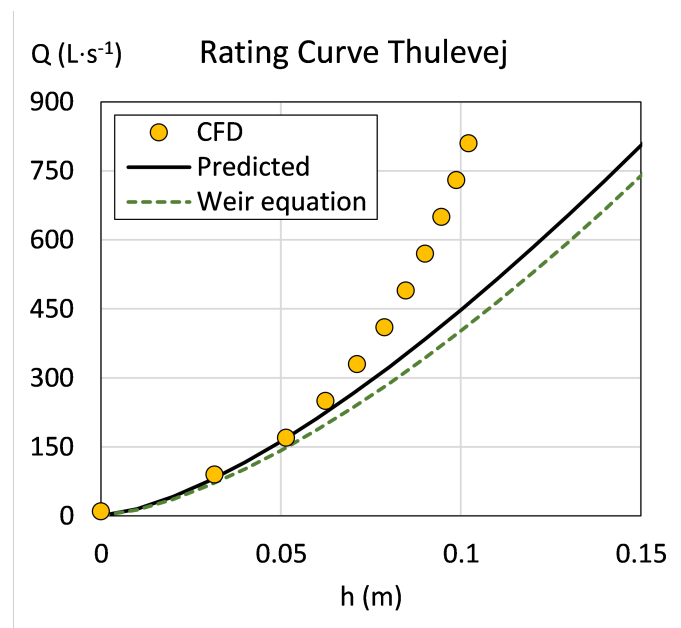


Figure 10.15. The results of the CFD modeling presented alongside the predicted rating curve and the standard weir equation. The results presented all neglects the effect of the screen.

The CFD results diverges from the predicted rating curve after a flow of 150 l/s. From here on, a significant build up of water is observed at end opposite the sensor location. The rating curves of figure 10.15 do not include the effect of the screen. To include the effect of the screen, the rating curve of the CSO structure has been adjusted by altering the weir coefficient using the approach discussed in section 8. The resistance of the screen has been predicted at different degrees of clogging assuming the use of equation 8.2 setting ζ' equal to 0.5. The screen has been assumed to have an even clogging distribution.

The measured flow and water level data has been analysed. The crest level has been calibrated as shown in appendix D. The water level and flow data has been plotted in figure 10.16 alongside the predicted rating curve at different degrees of clogging.

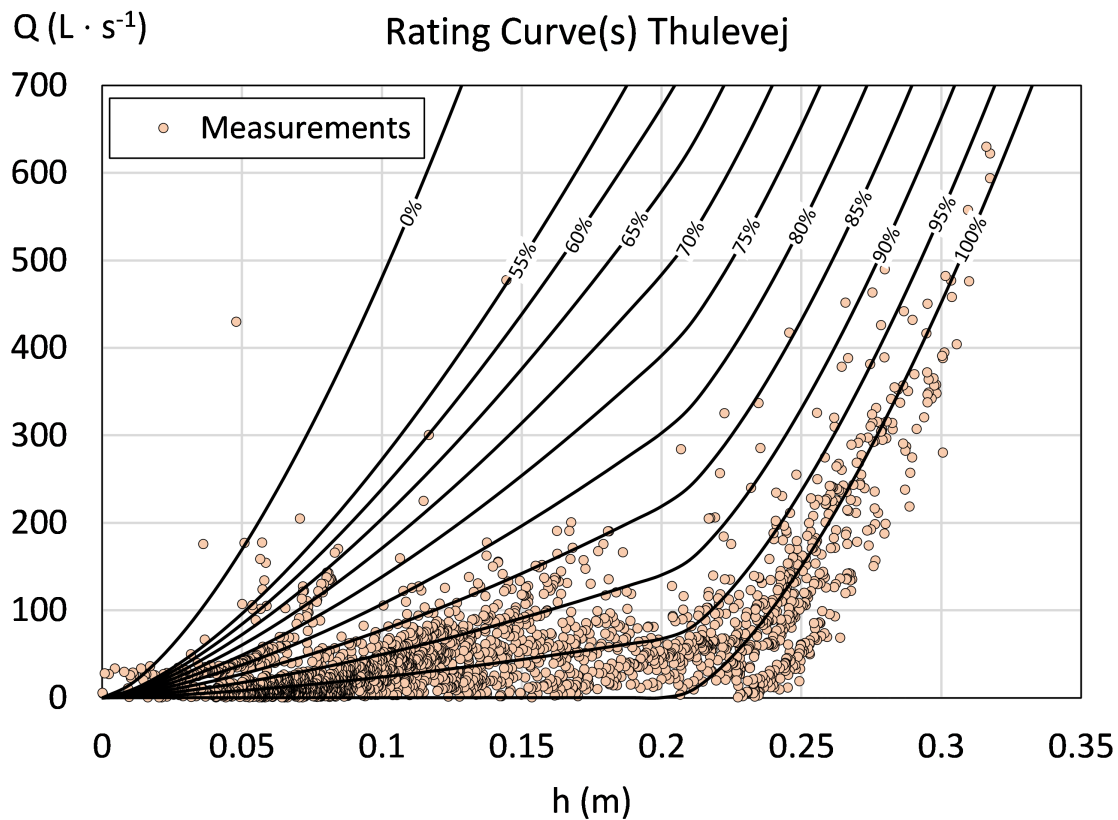


Figure 10.16. The predicted rating curve of Thulevej at different degrees of clogging shown alongside the measured data.

At a height of 0.2, the water starts to overflow the screen. This leads to a significant change of the rating curves trajectory. As it can be seen from figure 10.16 the screen induces a significant resistance to the flow, and almost all of the data points are located below the rating curve of an 85% clogging degree. On average the screen has been found to be 92% clogged.

Accuracy of CFD Modelling

It has been shown that the use of CFD modelling accurately can predict the flow over sharp crested weirs, as the modelled weir coefficient and the measured weir coefficient are very similar. Furthermore the weir coefficient of the simulated sharp crested weir has been found to increase linearly as a function of the h/p ratio similar to what is proposed by literature formula 3.5. The CFD model has however been found to slightly overestimate the weir coefficient compared to literature values as shown in figure 6.1. It is unknown what causes the slight error, however it is unavoidable that some numerical error will arise when using a numerical model. The error has however been found to be unaffected by the mesh resolution and the timestep used as seen in table 6.2, and as the data follows the same trend as proposed in the literature, it is concluded that the CFD in fact can be used to accurately determine the flow over a weir.

Predicting the Weir Coefficient

The statistical analysis of the randomly generated CSO structures showed that it is possible to predict the weir coefficient using the Froude number as predictive variable for sharp crested weirs. The Froude number describes the ratio between inertial and gravitational forces, and thereby is a good predictor for the build up of water within the CSO chamber and the water surface profile. The analysis has been based on subcritical conditions, and it is uncertain if the Froude number is also a good predictor at supercritical conditions. Supercritical conditions are however expected to be rare in CSO chambers.

All of the simulations have been simulated using a constant crest thickness of 4 cm to take into account that the weirs of real-life CSO structures aren't always sharp. As the simulations of short and broad crested weirs are included in the simulations of the side weir, the Froude number is no

longer able to predict the weir coefficient by itself as shown in figure 7.10. At small water heights compared to the crest thickness, the weir coefficient significantly decreases. It is therefore proposed that the weir coefficient can be split up into an ideal discharge coefficient determined by the geometry of the crest with respect to the water level height and a model coefficient that compensates for the water surface profile along the weir. It is hypothesized that the Froude number in fact predicts the model coefficient, and not the ideal discharge coefficient. This is substantiated by the fact that the relationship between the Froude number and the weir coefficient is strongly depended on the location of the water level measurement as shown in appendix H.

In all of the simulations a significant amount of scatter has been observed. Some of the scatter is suspected to be ascribed to variations in the ideal drag coefficient. If this was the case we would suspect to see some significant effect, when $\frac{h}{p}$ and $\frac{h}{T}$ are removed from the correlations which is not the case. The reason for this might be have to due with the non linearity of the relationship between the weir coefficient and the $\frac{h}{T}$ -ratio, as the weir springs free from the crest, a significant difference in the weir coefficient is observed. An increased amount of scatter has been observed at large Froude numbers. This might just be due to increased numerical errors as the water velocity increases. However for side weirs in specific a more plausible explanation might exist. At large Froude numbers a large water surface build up is observed along the weir. The difference in the water level along the length of weir might lead to the ideal weir coefficient not being constant along the weir. This was also seen in the simulations, where the nappe in some cases sprung free from the weir in only part of the weir length.

The ideal weir coefficient has been found to depend on the geometry of the crest in regard to the water level above the crest. A longer crest typically leads to more friction lowering the weir coefficient. At very short crest lengths, the nappe is seen to springs free from the weir, and the weir is said to be sharp crested. In the simulations this has been observed to happen at $\frac{h}{T} = 34$ and not at $\frac{h}{T} = 2$ as proposed by [Azimi and Rajaratnam, 2009]. The sharp crested weir coefficient has been found to be approximately the same as predicted by the theoretical equation 3.5. The weir coefficient of the short crested weir is however significantly different, indicating that the CFD model might not be able to adequately model the flow over the short crested weir at the used discretization. According to Azimi and Rajaratnam [2009] the weir coefficient should increase linearly up to a value of 0.8 before it spring free, such high weir coefficients are however not seen in the CFD models.

Even though the relationship derived between the Froude number and the weir coefficient indicates

that the weir coefficient can be determined accurately knowing the Froude number, the equations are only valid for CSO structures that fall within the range of the randomly generated structures. The division of the weir coefficient into a model coefficient and an ideal weir coefficient enables the relationships derived to be extrapolated to CSO structures outside the range of the random generated structures. Thereby allowing for an approximation closer to the actual weir coefficient, as exemplified by two of the five simulated CSO structures (Kalkværksvej and Fredtoftevej).

Determining the Froude Number

Even though the Froude number is a good predictor of the weir coefficient, for real-life CSO structures the Froude number itself is however unknown. The Froude number can be estimated by knowing the flow within the chamber and the water level data obtained from a water level sensor installed in the chamber. However, the flow within the chamber is influenced by both the flow over the weir and the flow through the outlet pipe. The flow over the weir is then again dependent on the weir coefficient. Assuming that the flow through the outlet pipe is known, we can establish a system of three equations with three dependent variables. This enables us to calculate the weir coefficient and subsequently determine the flow iteratively.

To assess the flow through the outlet pipe, an additional water level sensor can be installed in a downstream manhole. The difference in water level can then be used to estimate the flow. Alternatively, urban drainage models can be utilized to extract information regarding the outlet flow. However, it is important to note that any uncertainties associated with estimating the flow through the outlet pipe will affect the accuracy of the calculated weir coefficient. In many cases, the flow over the weir during storm events greatly exceeds the outflow. In some instances, water can even enter the chamber through both the inlet and outlet pipes due to water buildup in the system. It is therefore expected that the potential uncertainties regarding the flow through the outlet pipe in many cases only will have limited effect on the prediction of the weir coefficient.

Real-Life Structures

The analysis of the five real-life structures revealed that real-life structures don't necessarily fit into the two principal categories of CSO structures discussed in this report, being side weir and stilling ponds. Some real-life structures like the one at Bergsøe Plads doesn't fall into either category, and

some structures like the one at Thulevej may appear to belong to the side weir category, but a small feature such as the inlet having to pass over a primary weir, changes the flow characteristics of the structure, making the relationships derived non applicable.

For the CSO structure at Fredtoftevej and Bergsøe Plads annual discharge loads have been calculated and compared to what has been reported to the PULS database. The reported values have in both cases been based on 1 D dynamic urban drainage models, using MIKE Urban. For Fredtoftevej the predicted discharge loads have been estimated for the period between June 2022 and June 2023, and can therefore not directly be compared to what has been reported for the year of 2022. Nevertheless, the estimated values are within the same range as what has been reported. A comparison of the rating curve derived from the CFD model with the predicted rating curve and the standard weir equation found that the calculated annual discharge loads were all within a range of 10%. The difference has been found mainly to be due to the lower weir coefficient predicted by the CFD models. No significant effect was seen when implementing the effect of the discharge pipe. The reason for this is that only a single event within the measurement period surpassed the capacity of the discharge pipe. Based on this it can however not be concluded that the discharge pipe is negligible, as more intense storms might happen in the future. For the structure at Bergsøe Plads the predicted discharge loads can directly be compared to the MIKE Urban predicted loads, as water measurements have been provided for three consecutive years. The CFD based rating curve and the predicted rating curve both slightly overestimates the urban drainage models - especially for the year of 2020 and 2021, where the CFD is up to 50% larger than what has been calculated using the urban drainage models. The calculated loads from the urban drainage models are for the year of 2021 and 2022 within the range of the predicted model, indicating that the calibrated crest level might have been calibrated to be 0.5 cm too low. An alternative explanation for the difference lies in the neglect of the flap valves at the end of the discharge pipes, thereby overestimating the discharge during intense rainfall events.

For both the CSO structures at Fredtoftevej and Bergsøe plads the weir coefficients calculated from the CFD models are seen to be larger than what is predicted. For Fredtoftevej this is however only the case at low flow rates, whereas it is the case for all flow rates at Bergsøe Plads. This might have to do with the ventilation of the nappe. In the simulations of the randomly generated structures, a pressure boundary is placed on the downstream side of the weir to ensure a well ventilated nappe. In the simulations of the real-life CSO structures the downstream system has been included in the

model, it is therefore not possible to install a pressure boundary downstream the weir in the same manner. In real life a nappe can naturally be clinging or depressed, which increases the flow over the weir, however a small contraction or a small imperfection of the weir is often enough for the nappe to spring free - especially at high flow rates. In the CFD model, this is however suspected to be more difficult, also due to the resolution of the model. The air might have difficulties entering the underside of the nappe, when the resolution only is refined at the water-air interface. At figure 10.7 the water surface of the real life weir and the modelled weir of Fredtoftevej have been shown side by side. From the figure it looks like the nappe springs free from the weir in the foto, as the nappe follows what looks like a parabola. In the CFD model however the nappe seems to be clinging to the downstream side of the weir. The weir is contracted in the end closest to the discharge pipe, however it might not be enough for air to pass under the nappe in it's full length within the CFD model. In the CFD simulation performed by Rambøll, the system downstream the weir has not been included, and a pressure boundary has instead been installed. This ensures a fully ventilated nappe, and it can be seen from the results, that the weir coefficients of Rambøll in fact is lower than what has been estimated by the CFD model of this project. This is also why the weir coefficient predicted by Rambøll has been used in the prediction of the annual discharges. For the structure at Bergsøe Plads it is however unknown whether or not the nappe in fact springs free in real life or is in fact clinging. The overestimation of the yearly discharge loads could indicate that the weir coefficient is overestimated, however as previously explained the difference could also be due to the discharge pipes limiting the flow.

The Effect of the Discharge Pipe

The discharge pipe has been shown to potentially be limiting in 3 of the 5 structures modelled, and it is further expected to maybe also be limiting in the structure at Bergsøe Plads. Comparison of the CFD results with the predicted rating curves, shows that the rating curve can be predicted quite accurately just using the simple hydraulic model presented in this project. For the CSO structure at Kalkværksvej the orifice equation was used to predict the rating curve after the weir was submerged. The Rating curve was found to be almost entirely determined by the downstream system. It can be seen from figure 10.2 that the resistance of the orifice was slightly underestimated, this might be due to the channel connecting the weir to the orifice also inducing some hydraulic resistance, which has not been taken into account. Furthermore it can be seen, that the transition from a free

flowing weir to a fully submerged weir happens more gradually in the CFD model than what has been predicted. The reason for this is the simple model used in the prediction of the rating curve assumes the submersion of the weir to happen evenly along the length of the weir. As it can be seen in figure 10.3 the submersion however happens gradually along the length of the weir. For the structure at Linevangsvej, two predicted rating curves were shown, one where a perfect jet is assumed, and no energy is lost within the chamber, and one where all the energy from the inlet is dissipated within the chamber. As it can be seen, the CFD results follow the predicted curve assuming a complete dispersion until the discharge pipe gets completely submerged. Post this point the CFD results is seen to be located along the curve assuming a perfect jet. For some CSO structures, it is therefore possible that the kinetic energy entering the chamber through the inlet also has to be taking into account when predicting the rating curve after the weir has been submerged.

The Effect of Screens

As shown in table 8.1 CSO structures are frequently equipped with screens. Ideally the screens should be placed upstream the location of the water level sensor as is the case for the structure of Fredtoftevej. Often this is however not the case. The screen can significantly alter the rating curve - especially if the screen is severely clogged. This has been shown to be the case for the CSO structure at Thulevej, and it can be seen from the real life measurements shown in figure 10.16 that neglecting the screen will lead to substantial errors. This project doesn't propose a way to determine the degree of clogging of real-life screens, however a method to asses the hydraulic resistance of the screen as a function of the degree of clogging has been proposed. For the vertically mounted screen the hydraulic resistance can be related directly to an effective weir coefficient using equation 8.5. As shown in figure 8.5 and 8.6 the CFD models indicated that this method successfully converts the hydraulic resistance to an effective weir coefficient with an error of approximately 5%. The error might have to do with the screen affecting contraction effects of the nappe, however it could also just be due to the uncertainty of the CFD model. For the horizontal screen the CFD model showed that the proposed equation 8.7 was able to accurately predict the flow, however at low resistances and low screen lengths the baffle, at which the screen is attached, has been found also to induce a resistance. It is however expected that the resistance of real life screens are of a size where the effect of the baffle itself is insignificant.

The proposed method has been tested for a real-life weir equipped with a vertical screen. The

literature formula calculating the hydraulic resistance based of the degree of clogging has been showed to follow the measurements when the screen is significantly clogged. however as the screen is only lightly clogged the predicted values slightly deviates from the measurements. This might have to do with grid size of the screen used in the laboratory being to small for the formula to be valid. However as the size of the tape used to simulation of clogging are significant larger than the thickness of the screen, the measurements approaches the theoretical value at high degrees of clogging. This also explains why the theoretical equation of a wire screen more closely matches the calculated resistance of the non-clogged screen as seen in table 8.3. It is therefore suspected that even though the geometry of the screens determines the hydraulic resistance of the clean screen, the resistance of the screen will approach the one assuming a grid of sharp edged orifices.

Uncertainties of the Predicted Flow

Accordingly to [Nielsen et al., 2020] using a CFD model to determined the rating curve of a CSO structure allows for flow estimations within 5% uncertainty. This might be the uncertainty of a well set up CFD model, however the uncertainties are far larger when the CFD model gets coupled with real-life water level measurements. This has been shown in table 10.4 and table 10.5 where uncertainties of $\pm 15\%$ have been estimated. The problem is the crest level that has to be defined before combining the rating curve with the water level data, and any errors in the estimation of this level will lead to either a systematic over- or underestimation of the weir flow. Typically the crest and the sensor level are related using a differential GPS, however as has been shown for the CSO structure at Bergsøe Plads, using this technique the crest has been misplaced by 5 centimeters leading to flow predictions 3 times too large. Using the distribution of the measured water levels it has been shown that it is possible to determine the crest level quite accurately solely using the water level data of the sensor. It has however been estimated, that the level can only be determined within an accuracy of ± 0.5 cm. This is despite the water level data used in the calibration having a resolution of only 1 mm. The noise of the data is however too large for more accurate estimations to seem valid. The ranges of values presented in table 10.4 and table 10.5 shows that this 1 cm of uncertainty results in around $\pm 15\%$ uncertainty for both Fredtoftevej and Bergsøe Plads. As this uncertainty is an absolute uncertainty it decreases the when the build up of water is large. If the weir edge is very long, the build up of water is small, and the uncertainty will increase and vise versa. Ideally the crest length should therefore be quite small, or the crest might even be inclined to allow

for large waterlevel variations at small flow rates. CSO structures have however not been build to enable accurate flow measurements, but rather to ensure a certain water level not to be surpassed, which is effectively accomplished by the installation of a long horizontal weirs.

Another way to decrease the relative uncertainty of the water level measurement is to place the sensor where the largest build up of water within the chamber is observed. For side weirs this has been found to be at the backend of the structure opposite the inlet. This location has also been found to be the place with the lowest RMSE and highest R^2 when predicting the weir coefficient based on the Froude number. For the stilling pond the largest build up has been found right up against the side contractions of the weir. However even though the large build up would result in a reduced uncertainty of the water level, the accuracy in the prediction of the weir coefficient is reduced significantly. When placing the sensor considerations should also be done regarding the physics of the sensor. As the sensors used typically are ultrasonic sensors or radars which measure the water level over a surface, they should ideally be placed where the surface is plane. Furthermore, they should not be placed near walls, where the wall can interfere with the signal.

Conclusion 12

In this project a way to predict the rating curve of two types of CSO structures were developed; namely side weir CSO structures and stilling pond CSO structures. Three parameters were found to influence the rating curve; the weir coefficient determined affected the water surface profile within the chamber and the crest geometry, the presence of screens inducing an increased hydraulic resistance to the flow, and the capacity of the discharge pipe leading water away from the CSO structure.

The model has found that the weir coefficient can be predicted using the main channel Froude number for sharp-crested weirs. For short- and broad-crested weirs, it is proposed that the weir coefficient can be split up into a model coefficient and a ideal weir coefficient. By splitting up the weir coefficient, the weir coefficient can be estimated for a given structure. The model coefficient can be predicted using the main channel Froude number and the ideal weir coefficient can be estimated based of the geometry of the crest with respect to the water depth above the crest.

The optimal location for measuring the water level were determined for both types of CSO structures. For the side weir CSO structure the location giving the best correlation between the Froude number and the weir coefficient were found to be against the back wall of the CSO structure, for the stilling pond CSO structure the middle of the chamber were found to be the best location.

A method to adjust the rating curve to take into account the effect of screens have been proposed. Two different formulas has been proposed for horizontal and vertical mounted screens. It was found that the hydraulic resistance of the screen directly can be related to an altered weir coefficient for the vertical screen, and that it is also possible to accurately determine the flow of the horizontal screen knowing the hydraulic resistance of the screen. Based on laboratory experiments it has further been shown that the degree of clogging directly can be related to a hydraulic resistance of the screen.

A simple model that predicts the effect of the discharge pips has been proposed, and the model has been validated against CFD models of real life CSO structures. The model has been found to accurately predict at what flowrate the discharge pipe becomes limiting, and it further matches the

CFD results reasonably.

The analysis of five real-life CSO structures showed that the rating curves could accurately be predicted for three of the five structures. The three structures were all categorised as side weir structures. The analysis of the five structures also showed that not all structures fall into one of the two categories being side weir and stilling pond CSO structures. In three of the five real-life structures, the discharge pipe was seen to be potentially limiting for the flow. Yearly discharge loads have been calculated for two of the five structures and have been compared to discharge loads estimated using MIKE Urban drainage models. In both cases the predicted loads are within the same range as the loads estimated by the urban drainage models. The yearly discharge loads have been found to be strongly depended to the assumed crest level of the weir. A method to predict the crest level with an accuracy of ± 0.5 cm by analyzing the distribution of the water level measurements has been developed. For both CSO structures the uncertainty of ± 0.5 cm was found to result in $\pm 15\%$ uncertainty in the calculated annual discharge loads.

This project provides a method to predict the rating curve of two types of CSO structures, namely stilling ponds and side weir CSO structures. Thereby providing an alternative between the development of expensive custom CFD determined rating curves and just using the regular weir equation without considering its validity for the given structure. However the analysis of 5 real-life structures showed that not all CSO structures fall within one of the two categories. Therefore additional types of CSO structures could be investigated, eg. double sided weirs or CSO structures being a combination of side weirs and stilling ponds. It is suspected that the predictive variables being the Froude number and the crest geometry also will be good predictors for other types of structures, and the statistical approaches presented in this report is therefore suspected to also be used in when analysing other types of structures. Analysis of more types of CSO structures would allow to generate a catalogue, providing the location for optimal placement of the water level sensor as well as how to adjust the weir coefficient to fit this type of structure, thereby making accurate determination of CSO discharges using real time measurements widely accessible.

The statistical analysis used in the prediction of the weir coefficient has been based on multiple linear regression as well as polynomial regression, however as has been shown, the system is strongly nonlinear. Alternative statistical approaches could therefore have been used to increase the accuracy of the predictions. One such option is neural network based regression. The problem using neural networks is their tendency for over-fitting, and predictions based on neural networks would probably not be applicable outside the validity spectrum of the randomly generated CSO structures. Furthermore wide spread use of a trained neural network might be more difficult to attain than that of a simple regression, as it might be harder to distribute and to obtain widespread useage. Furthermore the training of a neural network typically requires vast amount of training data increasing the number of randomly generated CSO structures having to be analysed.

In this project a method to predict the effect of the screens installed in two different configurations were proposed. The method however is based on the knowledge of the clogging degree, which in

reality is unknown. For the method to be used in real life a way to determine the degree of clogging therefore has to be known. This could be achieved by the installation of a sensor that can determine the degree of clogging. A study by See et al. [2021] has proposed that the use of microphones and speakers can determine the degree of clogging based on the reflection of the sound by the screen. An alternative approach could be the modelling of the screen clogging. A model based on a gross solid concentration in the water could be used in combination with the water level measurement to gradually clog the screen as water passes through and the screen clogs. The degree of clogging could then be assessed when manually cleaning the screen eg. by the use of image analysis. The problem is however that the screen often clogs very fast as is the case at Thulevej, and the installation of mechanical self cleaning screens are often a good idea. Depending on the rate of cleaning the mechanical cleaned screen should induce a more or less constant resistances.

The comparison of the yearly discharge loads calculated for the real-life structures showed that the uncertainty of the predicted discharge loads might not explain that the use of measurements are much better than the use of urban drainage models. However there are more advantages to the implementation of real life measurements than just calculations of the yearly discharge loads. The use of real life measurements provides near real time data of the CSO discharges providing valuable knowledge which allows for closing of public baths, planning of cleaning and maintenance of the CSO structure and screens and the water bodies, and knowledge about if the system is working properly, or if eg a clogged sewer system leads to frequent overflow events.

References

- Aarhus Kommune (2022). Spildevandsplan 2021-2026.
- Akan, A. O. and Houghtalen, R. J. (2003). *Urban hydrology, hydraulics, and stormwater quality: engineering applications and computer modeling*. John Wiley & Sons.
- Al-Khateeb, H., Sahib, J., and Alyassiry, H. (2019). An experimental study of flow over v-shape crump weir crest.
- Azimi, A. H. and Rajaratnam, N. (2009). Discharge characteristics of weirs of finite crest length. *Journal of Hydraulic Engineering-asce - J HYDRAUL ENG-ASCE*, 135.
- Bagheri, S., Kabiri-Samani, A., and Heidarpour, M. (2014). Discharge coefficient of rectangular sharp-crested side weirs, part i: Traditional weir equation. *Flow Measurement and Instrumentation*, 35:109–115.
- Balmforth, D. (2009). Modelling ancillaries: Weir coefficients. *WaPUG USER NOTE*, (27).
- Chanson, H. (2004). *The Hydraulics of Open Channel Flow: An Introduction*. Number ISBN: 0750659785 in eBook. Elsevier Butterworth-Heinemann.
- Danmarks Miljøportal (2023). *Arealinformation*. <https://arealinformation.miljoeportal.dk>. downloaded: 07-06-2023.
- Department for Environment Food and Rural Affairs (2022). Storm overflows discharge reduction plan. (ISBN: 978-1-5286-3671-1).
- Di Bacco, M. and Scorzini, A. R. (2019). Are we correctly using discharge coefficients for side weirs? insights from a numerical investigation. *Water*, 11(12).
- Domínguez, F. J. (1935). Curso de hidráulica general (continuará).
- Dubuat, P. L. G. (1816). *Principes d'hydraulique et de pyrodynamique, vérifiés par un grand nombre d'expériences faites par ordre du gouvernement*, volume 1. Didot.

- Dufresne, M., Vazquez, J., Terfous, A., Ghenaim, A., and Poulet, J.-B. (2009). Cfd modeling of solid separation in three combined sewer overflow chambers. *Journal of Environmental Engineering-asce - J ENVIRON ENG-ASCE*, 135.
- Emiroglu, M. E., Agaccioglu, H., and Kaya, N. (2011). Discharging capacity of rectangular side weirs in straight open channels. *Flow Measurement and Instrumentation*, 22(4):319–330.
- Fach, S., Sitzenfrei, R., and Rauch, W. (2008). Assessing the relationship between water level and combined sewer overflow with computational fluid dynamics.
- Francis, J. B. (1883). *Lowell Hydraulic Experiments*. D. VAN NOSTRAND.
- Frank-Gopolos, T., Nielsen, L., and Skovmark, B. (2021). *Punktkilder 2020*. Number ISBN: 978-87-7038-368-4. Miljøstyrelsen.
- Guo, N. (2011). Improving the operation and maintenance of cso structures. *The University of Sheffield*.
- Hager, W. H. (1987). Lateral outflow over side weirs. *Journal of Hydraulic Engineering*, Vol. 113, Issue 4:s. 491–504.
- Horten (2023). *Ny nævnsafgørelse om udledning af regnvand til miljøbelastede recipienter*. <https://www.horten.dk/nyhedsliste/2023/marts/ny-afgoerelse-om-udledning-af-regnvand-til-miljoebelastede-recipienter>. downloaded: 06-06-2023.
- Idelchik, I. E. (1960). *Handbook of Hydraulic Resistance*. Jaico Publishing House.
- Iwasa, Y., Ito, M., Okuda, C., Steinhardt, J., and Morita, H. (2019). Combined effect of cso screen and water surface control device on floatables removal. *9th International Conference on Sewer Processes Networks*.
- Jung-Madsen, S., Boutrup, S., Nielsen, V. V., Hansen, A. S., Svendsen, L. M., Fredshavn, J., Blicher-Mathiesen, G., Thodsen, H., Hansen, J. W., Høgslund, S., Johansson, L. S., Nygaard, B., Kjær, C., Ellermann, T., Thorling, L., and Frank-Gopolos, T. (2021). *VANDMILJØ OG NATUR 2020*. Aarhus Universitet, DCE – Nationalt Center for Miljø og Energi.

- Larrarte, F., Lepot, M., Clemens-Meyer, F. H. L. R., Bertrand-Krajewski, J.-L., Ivetic ´, D., Prodanovic ´, D., and Stegeman, B. (2021). "Water level and discharge measurements". In Bertrand-Krajewski, J.-L., Clemens-Meyer, F., and Lepot, M., editors, *Metrology in Urban Drainage and Stormwater Management*, chapter 3, pages 35–97. IWA Publishing, 1 edition. ISBN: 9781789060119.
- Madsen, H. M. (2021). Nyt banebrydende projekt: Datadrevne løsninger skal nedbringe overløb og forbedre vandmiljøet.
- Malte Ahm, Søren Liedtke Thorndahl, J. E. N. and Rasmussen, M. R. (2016). Estimation of combined sewer overflow discharge: a software sensor approach based on local water level measurements. *Water Sci Technol*, 74(11):2683–2696.
- Miljø- og Fødevarerklagenævnet (2023). Ophævelse og hjemvisning af § 25-tilladelse til etablering af ny forbindelsesvej.
- Moesgaard, T. C. (2021). Lokalpolitikere kendte ikke til problem med urensset spildevand. *Tv2 Østjylland*.
- Murali, s., Hipsey, M., Ghadouani, A., and Yuan, Z. (2019). The development and application of improved solids modelling to enable resilient urban sewer networks. *Journal of Environmental Management*, 240.
- Murla, D., Ellerbæk, J., Sørensen, L., and Rasmussen, M. R. (2018). Cso structure analysis and class library building.
- Nadesamoorthy, T. and Thomson, A. (1972). Discussion of 'spatially varied flow over side-weirs'. *Journal of the Hydraulics Division*, 98(12):2234–2235.
- Nielsen, K. T., Ørjan Heggdal, and Rasmussen, M. R. (2020). Puls-indberetning af overløb - udarbejdelse af grundlag for standardiseret indberetning af overløb. *Forsyningssekretariatet*.
- Openchannelflow (2023). *Aeration of Weir Nappes*.
<https://www.openchannelflow.com/blog/aeration-of-weir-nappes>. downloaded: 04-06-2023.
- Poleni, G. (1717). *Joannis Poleni de Motu Aquae Mixto Libri Duo*. Number 9781166954598. Kessinger Publishing, Llc.

- Raju, K. G. R., Gupta, S. K., and Prasad, B. (1979). Side weir in rectangular channel. *Journal of the Hydraulics Division*, 105(5):547–554.
- Rambøll (2022a). Fredtoftevej: Cfd-analyse af overløbsbassin. *CFD Overløb MUDP*.
- Rambøll (2022b). Lindevangsvej: Cfd-analyse af overløbsbassin. *CFD Overløb MUDP*.
- Regeringen (2022). Ansvar for danmark - det politiske grundlag for danmarks regering.
- Schmidt, M. (1954). *Zur Frage des Abflusses über Streichwehre: eine kritische Betrachtung der bekanntesten Berechnungsverfahren und Versuche im Zusammenhang mit eigenen Versuchen*. Institut für Wasserbau der Techn. Univ.
- See, C. H., Horoshenkov, K. V., Ali, M. T. B., and Tait, S. J. (2021). An acoustic sensor for combined sewer overflow (cso) screen condition monitoring in a drainage infrastructure. *Sensors*, 21(2).
- Siemens Industry Software (2020). *Star-CCM+ User Manual*.
- Subramanya, K. and Awasthy, S. C. (1972). Spatially varied flow over side-weirs. *Journal of the Hydraulics Division*, 98(1):1–10.
- Sørensen, L. (2022). Cfd-modellering og 3d-scanning af overløbsbygværker. In *EVA themedag: Overløb – Har vi styr på dem?*, Nyborg.
- Tracy, H. J. (1957). Discharge characteristics of broad-crested weirs. *Geological Survey Circular*, 397.
- United States Department of the Interior Bureau of Reclamation (2001). *Water Measurement Manual*. eBook.
- WaPUG (2006). The design of cso chambers to incorporate screens. *Wastewater Planning Users Group Code Of Practice User Note*.
- Winther, L., Linde, J. J., Jensen, H. T., Mathiasen, L. L., and Johansen, N. B. (2016). *Afløbsteknik*. Number ISBN: 978-87-502-1015-3. Ployteknisk forlag.

Dimensional Analysis A

For an ideal weir placed in a rectangular channel, the following 9 parameters are expected to be sufficient to describe the flow characteristics. The dimensions of each parameter has been shown above the parameter (M being mass, L being length and T being time):

$$0 = f \left(\begin{matrix} L & \frac{L}{T} & \frac{M}{L^3} & \frac{M}{T^2 \cdot L^2} & \frac{M}{L \cdot T} & \frac{M}{T^2} & L & L & L \\ (h, & v, & \rho, & \gamma, & \mu, & \sigma, & B, & T, & p) \end{matrix} \right)$$

Where h is the water level above the weir crest (m), v is the weir flow velocity ($m \cdot s^{-1}$), ρ is the density of water ($kg \cdot m^{-3}$), γ is the specific weight of water ($kg \cdot s^{-2} \cdot m^{-2}$), μ is the dynamic viscosity of water ($kg \cdot s^{-1} \cdot m^{-1}$), σ is the surface tension of water ($m \cdot s^{-2}$), B is the width of the channel (m), T is the thickness of the weir (m) and p is the height of the crest (m).

By using h, v and ρ as repeating variables we can simplify the above. To being the the mass dimension can be eliminated using the density (ρ):

$$0 = f \left(\begin{matrix} L & \frac{L}{T} & \frac{M}{T^2} & \frac{L^2}{T} & \frac{L^3}{T^2} & L & L & L \\ (h, & v, & g, & \frac{\mu}{\rho}, & \frac{\sigma}{\rho}, & B, & T, & p) \end{matrix} \right)$$

We can eliminate the time dimension using the weir velocity (v):

$$0 = f \left(\begin{matrix} L & \frac{1}{L} & L & L & L & L & L \\ (h, & \frac{g \cdot h}{v^2}, & \frac{\mu}{\rho \cdot v}, & \frac{\sigma}{\rho \cdot v^2}, & B, & T, & p) \end{matrix} \right)$$

Lastly we can eliminate the length dimension using the water level above the crest (h) resulting in 6 dimensionless quantities:

$$0 = f \left(\frac{g \cdot h}{v^2}, \frac{\mu}{\rho \cdot v \cdot h}, \frac{\sigma}{\rho \cdot v^2 \cdot h}, \frac{B}{h}, \frac{T}{h}, \frac{p}{h} \right)$$

From this we can see that the first three quantities can be rewritten into Froude number, Reynolds number and the Weber number respectively:

$$0 = f \left(Fr, Re, We, \frac{B}{h}, \frac{T}{h}, \frac{p}{h} \right)$$

In the ideal channel h and v cannot vary independently, therefore the Froude number is not an independent parameter. We can therefore see the Froude number as a constant as proposed by [Tracy, 1957]. A little rewriting shows that the Froude number directly can be seen as a equivalent to the weir coefficient:

$$Fr = \frac{v}{\sqrt{g \cdot h}} = \frac{Q}{\sqrt{g} \cdot B \cdot h^{1.5}} = \sqrt{2} \cdot C \quad (\text{A.1})$$

As we can see the Froude number is directly proportional to the weir coefficient. The above equation can therefore be rearranged into:

$$C = f \left(Re, We, \frac{B}{h}, \frac{T}{h}, \frac{p}{h} \right)$$

It has been found that the Re and We are insignificant in most piratical cases [Bagheri et al., 2014]. And if we assume no contraction in the channel the expression further simplifies into:

$$C = f \left(\frac{T}{h}, \frac{p}{h} \right)$$

Which is what we see in the literature of experiments by [Azimi and Rajaratnam, 2009], where the weir coefficient can be predicted using these two parameters. From a physical perspective the $\frac{h}{p}$ can be said to compensate for the velocity head approaching, the higher the $\frac{h}{p}$, the larger the relative approach velocity. The $\frac{h}{T}$ influences the dynamics of the nappe in relation to the weir edge, eg if the nappe spring free from the weir or not [Azimi and Rajaratnam, 2009].

Unlike the ideal rectangular channel, CSO structure are typically equipped with an outlet pipe. Therefore the channel flow can vary independently of the water level height. Furthermore more dimensions have to be included to take into account the more complex geometry.

Stilling pond CSO structure

For the stilling pond CSO structure illustrated in figure 1.2 we assume the following parameters to affect the weir flow:

$$0 = f (h, v, \rho, \gamma, \mu, \sigma, B, T, p, L, D_{in}, D_{out}, b, v_1) \quad (\text{A.2})$$

Where the first 9 parameters are the same as before. The latter 5 are however new. L is the length of the chamber (m), D_{in} is the inlet diameter (m), D_{out} is the outlet diameter (m), b is the width of the weir (m), and v_1 is the main channel flow velocity ($\text{m} \cdot \text{s}^{-1}$).

Using the same approach as above we are able get the following dimensionless quantities (Π -groups):

$$0 = f (Fr, Re, We, \frac{B}{h}, \frac{T}{h}, \frac{p}{h}, \frac{D_{in}}{h}, \frac{D_{out}}{h}, \frac{b}{h}, \frac{v_1}{v}) \quad (\text{A.3})$$

By combining some of the Π -groups, the following dimensionless parameters can be defined:

$$C = f (Fr_1, Re, We, \frac{B}{h}, \frac{h}{T}, \frac{h}{p}, \frac{L}{B}, \frac{D_{in}}{B}, \frac{D_{out}}{B}, \frac{b}{B}) \quad (\text{A.4})$$

Where Fr_1 is the main channel Froude number.

Side weir CSO structure

For side weirs the channel flow changes along the length. Therefore an additional downstream flow velocity is included [Emiroglu et al., 2011]:

$$0 = f (h, v, \rho, \gamma, \mu, \sigma, B, T, p, D_{in}, D_{out}, b, v_1, v_2, L_{in}, L_{out}) \quad (\text{A.5})$$

Where the first 12 parameters are the same as before. v_1 is the main channel velocity at the upstream edge of the weir ($\text{m} \cdot \text{s}^{-1}$), v_2 is the main channel velocity at the downstream edge of the weir ($\text{m} \cdot \text{s}^{-1}$), L_{in} is the main channel upstream length (m) and L_{out} is the main channel downstream length (m)

Again using the same technique as before we get the following dimensionless parameters:

$$C = f (Fr_1, Re, We, \frac{B}{h}, \frac{h}{T}, \frac{h}{p}, \frac{D_{in}}{B}, \frac{D_{out}}{B}, \frac{b}{B}, \frac{L_{in}}{h}, \frac{L_{out}}{h}, \frac{v_{in}}{v_{out}}) \quad (\text{A.6})$$

Derivation of the Weir Equation

B

The weir equation is based of the Bernoulli's principle, which relates the water pressure to the water velocity for two cross sections within a channel. Cross section 1 is placed upstream the weir across the channel, and cross section 2 is placed above the weir.

$$h_1 + \frac{v_1^2}{2 \cdot g} = h_2 + \frac{v_2^2}{2 \cdot g} \quad (\text{B.1})$$

Assuming a horizontal weir installed across a channel of infinite cross section, the velocity of the channel (v_1) can be assumed equal to 0. The pressure at the weir (h_2) is 0, as the water is free falling.

$$h_1 = \frac{v_2^2}{2 \cdot g} \quad (\text{B.2})$$

From this the velocity can be seen to equal:

$$v = \sqrt{2 \cdot g \cdot h} \quad (\text{B.3})$$

Bernoulli's principle assumes no loss of energy, in practice however drag forces induces a loss of energy at the weir. Therefore a drag coefficient is included, called the discharge coefficient:

$$v = C_d \cdot \sqrt{2 \cdot g \cdot h} \quad (\text{B.4})$$

This equation is then integrated over the height of the water table above the crest:

$$q = \int_0^h C_d \cdot \sqrt{2 \cdot g \cdot h} \, dh \quad (\text{B.5})$$

$$q = \frac{2}{3} \cdot C_d \cdot \sqrt{2 \cdot g} \cdot h^{1.5} \quad (\text{B.6})$$

This is then the flow per unit length of the channel. For a rectangular weir with a horizontal weir edge the flow of the weir can then be calculated as:

$$Q = \frac{2}{3} \cdot C_d \cdot B \cdot \sqrt{2 \cdot g} \cdot h^{1.5} \quad (\text{B.7})$$

In some cases the assumption of insignificant velocity head in the upstream channel is insufficient, in these cases the water level is therefore substituted for the total head:

$$Q = \frac{2}{3} \cdot C_d \cdot B \cdot \sqrt{2 \cdot g} \cdot H^{1.5} \quad (\text{B.8})$$

However in practice, the effect of the approaching velocity head is often taken into account by adjusting the discharge coefficient.

To simplify the expression, the discharge coefficient is sometimes simplified into the weir coefficient by multiplying it with 2/3, it is then just denoted C:

$$Q = C \cdot B \cdot \sqrt{2 \cdot g} \cdot h^{1.5} \quad (\text{B.9})$$

Correction for Surface Tension Effects



The flow and water level measured above the weir of the laboratory experiments has been presented in the following table together with the calculated weir coefficient using the weir equation, shown in equation 3.1:

Table C.1. Measured flow and water level data shown together with the calculated weir coefficients.

h (cm)	Q (l/s)	Weir coefficient (-)
5.1	7.5	0.26
6.1	10.0	0.26
6.8	13.1	0.29
7.5	15.6	0.30
7.5	15.2	0.29
7.5	14.8	0.29

As table C.1 shows, the weir coefficient seems to increase as a function of the water level. This is somewhat surprising, and based on this as well as observations of the flow through the screen, it is hypothesised that surface tension holds back water in the top of the screen where the pressure is low, effectively reducing the screen area. The length of the screen blocked by the surface tension is suspected to be constant and unaffected by the flow and the water level. The effect of the surface tension on the calculated weir coefficient is therefore reduced as the water level increases, due to the blocked length relatively getting smaller. The effect is illustrated in the figure C.1.

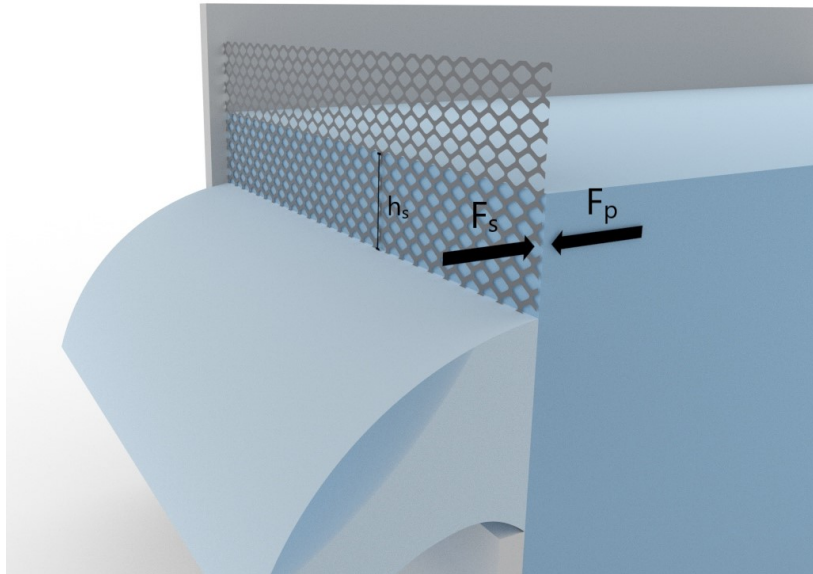


Figure C.1. Illustration of the surface tension blocking the water from passing through the top of the screen.

An experiment where the upper surface of the screen were blocked was conducted to remove the surface tension blocked part of the screen. This gave the following data:

Table C.2

h (pressure) (cm)	h (area) (cm)	Q (l/s)	C (-)
7.3	4.9	11.3	0.34

The weir coefficient has been determined using the following alteration of the weir equation:

$$Q = C \cdot B \cdot \sqrt{2 \cdot g} \cdot \sqrt{h_p} \cdot h_a \quad (\text{C.1})$$

Where h_p is the height of the water table, and h_a is the height of flow. As it can be seen the weir coefficient further increases when the top area is removed. This further indicates, that the surface tension is effectively reduces the area of the screen.

It is hypothesized that the weir coefficient should be approximately independent of the water level at the scale of water level variations seen in the experiments. Therefore the variance of the calculated weir coefficients have been shown in the following figure as a function of the assumed surface tension length (h_s):

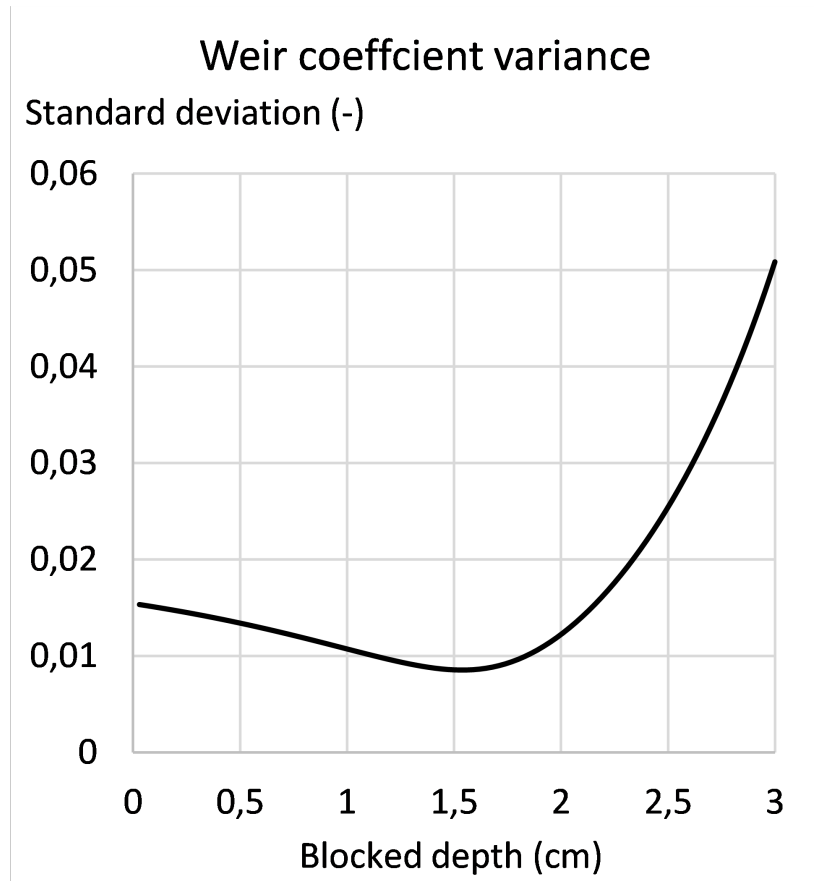


Figure C.2. Standard deviation of the 6 calculated weir coefficients as a function of the assumed depth blocked by the surface tension.

As it can be seen the lowest variability is around 1,5 cm of depth. The analysis is however based on a very limited number of data points, and therefore any measurement uncertainty will induce significant uncertainties. If we instead assume, the weir coefficient of table C.2 represents the correct weir coefficients, and adjust the depth of the blocked surface, to fit the weir coefficients to this value, we get the following depth: 1,14 cm.

The depth of the surface tension blocking can be calculated as the depth at which the hydrostatic pressure force exceeds the force of surface tension. The pressure force on an area equals:

$$F_p = A \cdot h \cdot \rho \cdot g \quad (\text{C.2})$$

Where A is the area of a grid opening, h is the depth, rho is the density of water and g is the gravitational acceleration.

The force of surface tension equals:

$$F_s = \sigma \cdot L \cdot \cos(\theta) \quad (\text{C.3})$$

Where σ is the surface tension of water, L is the perimeter of a grid opening, θ is the contact angle.

Right before the surface tension breaks, the contact angle equals 90 degrees, and the surface tension has the maximal force. Water typically has a surface tension of $0,072 \text{ N} \cdot \text{m}^{-1}$.

The length which the surface tension functions over equals the circumference of a screen hole, and the area used to calculate the pressure force is the area of the same hole. These two quantities has been measured:

Table C.3

Circumference (m)	Area (m ²)
$1.03 \cdot 10^{-2}$	$6.4 \cdot 10^{-6}$

A picture of the screen used has been shown below.

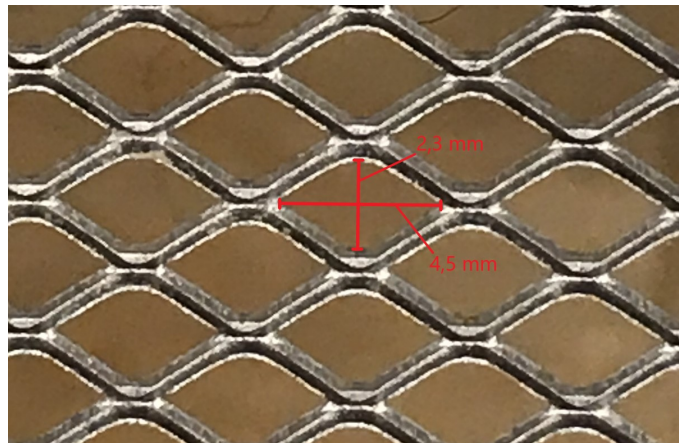


Figure C.3. Zoomed in picture of the screen used.

The depth can then be calculated setting the forces equal, and the solving for the depth:

$$h_s = \frac{\sigma \cdot L \cdot \cos(90)}{A \cdot \rho \cdot g} \quad (\text{C.4})$$

$$h_s = \frac{0,072 \frac{\text{N}}{\text{m}} \cdot 1.03 \cdot 10^{-2} \text{ m} \cdot 1}{6.4 \cdot 10^{-6} \text{ m}^2 \cdot 997 \frac{\text{kg}}{\text{m}^3} \cdot 9.81 \frac{\text{m}}{\text{s}^2}} = 1.17 \text{ cm} \quad (\text{C.5})$$

As it can be seen this is almost exactly the same value as found when fitting to the value of table C.2 (1.14 cm). It therefore seems reasonable to assume that we can compensate for the surface tension by subtracting 1.17 cm from the measured water level to calculate h_a and applying equation C.1 using the regular water level as h_p . This has therefore been done when determining the weir coefficient for the experiments where the weir is equipped with a screen, as the grid size of real life screens typically is far too large for any surface tension effects to be significant.

Automatic Calibration of the Weir Crest

D

As of today state of the art when determining the elevation of the weir and the ultrasonic sensor is the use of a differential GPS. The advantage of such is the ability to assign the level measurements into a universal system. And measurements in different part of the sewer systems can directly be related to each other. The determination of crest, and sensor levels requires high precision, and for this use the differential GPS is considered somewhat uncertain. The Differential GPS only allows for measurement accuracies of 1-3 cm, and furthermore this approach is very sensitive to manual errors, such that displacement of the sensor of only a few centimeters will result in significant error. It makes no sense using rating curves obtained by expensive CFD models if the input data is off. An alternative approach is to use the data from the sensor to determine the level of the crest. As the charastics of the systems changes dramatically when the waterlevel surpasses the crest level, this will also be seen in the waterlevel data.

Under rainfall events the water level in the CSO structure will increase until the outflow from the CSO chamber equals the inflow. As the outflow capacity increases drastically when the water level surpasses the crest, the water level have difficulties surpassing this level. Therefore water levels right above the weir edge will be far more common than water levels right below the weir edge. Plotting the distribution of measured water levels, it is possible to quite accurately determine the crest level. The clearness of the weir edge in the data depends on the weir length, and the CSO chamber. Especially for high weir CSO chambers the weir edge is expected to be easily determined. The advantage of doing such is further that the water level sensor and the weir level is directly related, and possible errors from sensor displacement are avoided, disregarding any installation mistakes. The concept has been illustrated in figure D.1.

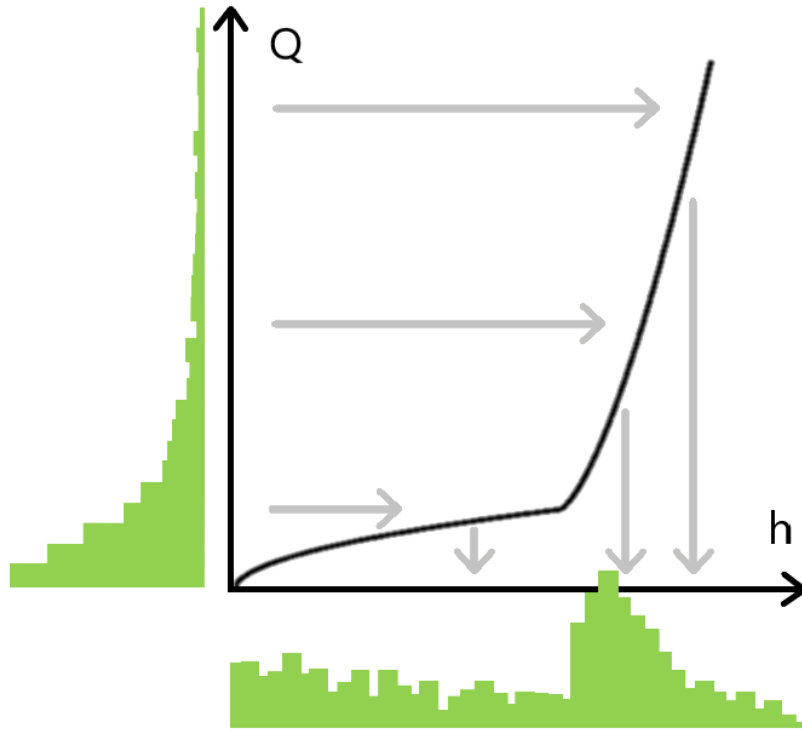


Figure D.1. Illustration of how the distribution of flow rates are transformed into a distribution of water level data.

The disadvantage using this method is that the crest level cannot be determined when the sensor is installed, and can first be estimated after some data has been obtained.

This concept has been tested using the flow measurements of Thulevej, and a hypothetically CSO structure. The inflow rate is the measured inflow rates into Thulevej, the outflow rate is assumed constant. The water level of the structures is modelled using simple Euler:

$$\frac{dz}{dt} = \frac{Q_i - Q_u - Q_o}{A} \quad (\text{D.1})$$

Where Q_o is the weir flow calculated as: if $z > p$

$$Q_o = C \cdot B \cdot \sqrt{2 \cdot g} \cdot (h) \quad (\text{D.2})$$

else:

$$Q_o = 0 \quad (\text{D.3})$$

Using two years of flow data, and a CSO structure with an area of 20 m², a outflow of 50 L · s⁻¹, a crest level of 4 meters and a weir width of 1 meter the following distribution was calculated. The model was simulated using a time step of 1 second.

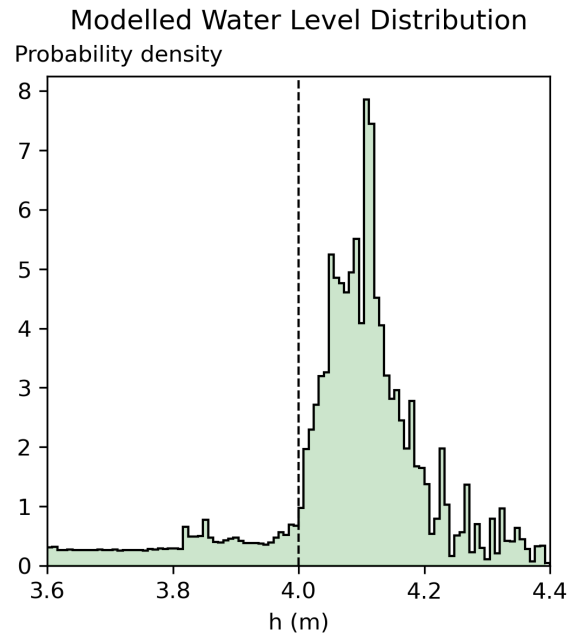


Figure D.2. Probability density of the weir in the model

As it can be seen the density sharply increases after the water level of 4 meters. However also a small increase before the weir edge is seen. This is suspected to be a random bump like what is seen around 3.85 meters of height. Based on this the method considered accurate. However, as it can be difficult to determine the exact crest level, the level has been determined with a ± 0.5 cm uncertainty. In figure D.3 an analysis of the water level data from Bergsøes Plads has been shown.

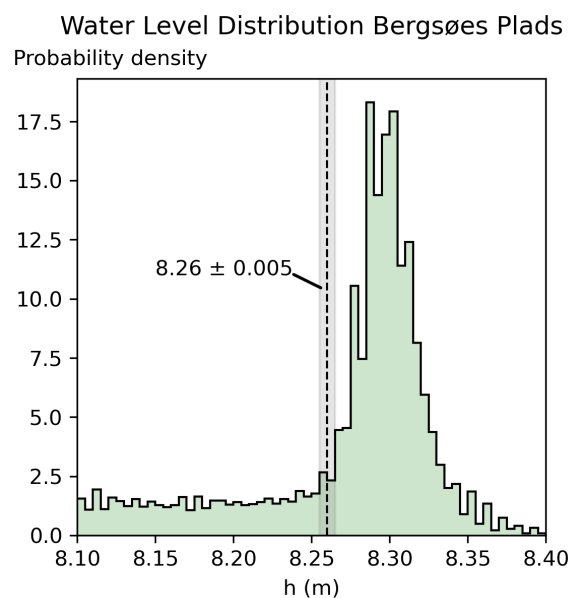


Figure D.3. Probability density of the CSO structure at Bergsøes Plads.

The real life data looks very similar to the modelled, the increase however seem a little more gradual

inducing a small uncertainty when determining the elevation of the crest level. This can be due to noise of the data. The crest level of structure at Bergsøe Plads has originally been determined by the use of a differential GPS to be located at a height of 8.21 m. This is 5 cm below the one found in the calibration. In figure D.4 the analysis of the CSO structure at Thulevej has been shown.

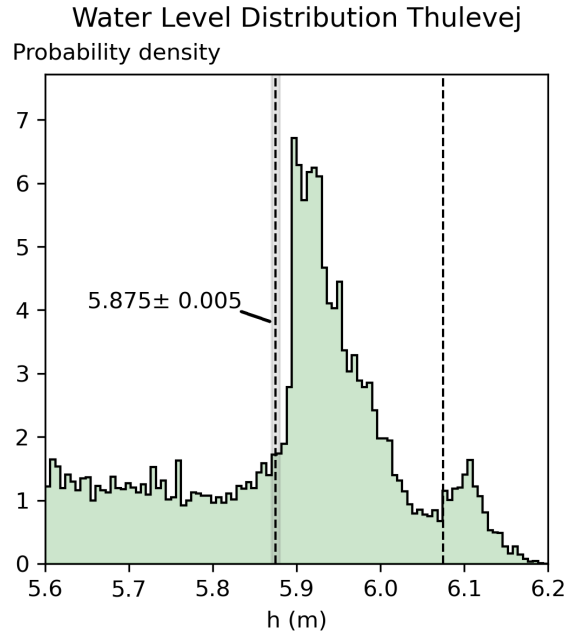


Figure D.4. Probability density of the CSO structure at Thulevej.

At Thulevej a second increase in the in the density is seen at 6.1 m, this corresponds to the top of the screen. When the screen is fully clogged, it overflows, increasing the overflow capacity. In figure D.5 the water level distribution for the CSO structure at Fredtoftevej has been shown.

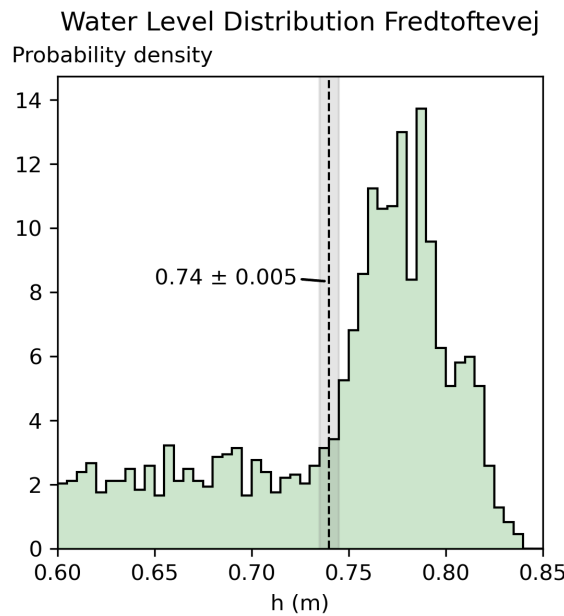


Figure D.5. Probability density of the CSO structure at Fredtoftevej.

Resistance of Bar Gratings E

The coefficient of hydraulic resistance can for bar gratings be estimated using equation E.1 [Idelchik, 1960].

$$\zeta = \beta \cdot \zeta' \cdot \sin(\Theta) \quad (\text{E.1})$$

Where β is the drag coefficient of the bar, that depends on the shape of the bars, see figure E.1. Θ is the angle of the bars with respect to the flow direction. The angle equals 90° if the water is flowing perpendicular to the screen. ζ' is the orifice resistance coefficient of a thick orifice installed in a channel with approximately indefinite upstream and downstream cross sections.

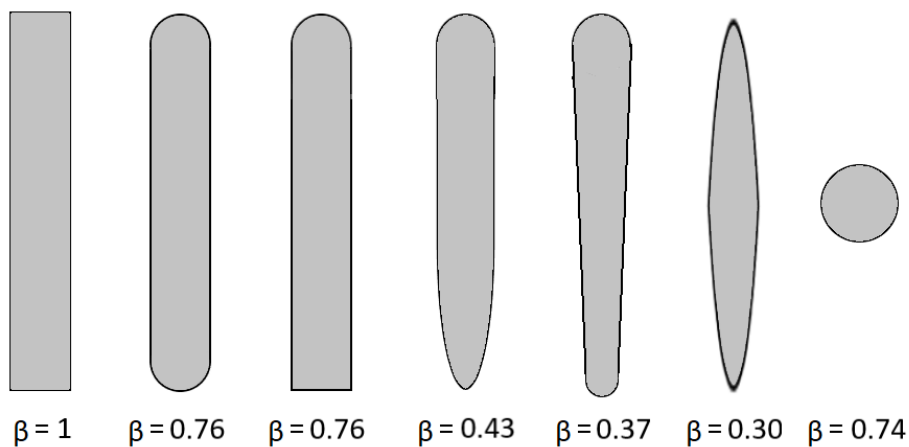


Figure E.1. The drag coefficient of the bars (β). Figure is modified after [Idelchik, 1960].

ζ' is determined using equation E.2 [Idelchik, 1960].

$$\zeta' = \left(0.5 \cdot (1 - f)^{0.75} + \tau \cdot (1 - f)^{1.375} + (1 - f)^2 + \lambda \cdot \frac{l}{d_h} \right) \cdot \frac{1}{f^2} \quad (\text{E.2})$$

Where f is the clear fraction of the screen, and λ is the Darcy friction coefficient of the screen surface (-), l is the thickness of the screen (m) and d_h is the hydraulic diameter of the screen (m).

τ is defined as:

$$\tau = (2.4 - l)^\phi \quad (\text{E.3})$$

and ϕ is then calculated as:

$$\phi = 0.25 \cdot \frac{0.535 \cdot l^8}{0.05 + l^7} \quad (\text{E.4})$$

Screen Resistance Calculations

F

The geometrical quantities of the screen used in the laboratory have been assessed through the analysis of a picture of the screen as shown in figure C.3 of appendix C. The calculated geometrical dimensions has been presented in table F.1.

Table F.1

Parameter	symbol	value
Clean fraction of the screen (-)	f	0.57
Hydraulic diameter (mm)	d_h	0.06
Thickness of the screen (mm)	l	1
angle (°)	α	60

From table F.1 the ζ' from equation 8.2 can based on data presented in Idelchik [1960] be determined to equal 0.18. This then gives a coefficient of hydraulic resistance of:

$$\zeta = (\sqrt{\zeta'} \cdot (1 - f)^{0,375} + 1 - f)^2 \cdot \frac{1}{f^2} \quad (\text{F.1})$$

$$\zeta = (\sqrt{0.18} \cdot (1 - 0.57)^{0,375} + 1 - 0.57)^2 \cdot \frac{1}{0.57^2} = 1.65 \quad (\text{F.2})$$

From table F.1 $\frac{1}{D_h}$ has been estimated to 0.06, which makes the above equation invalid, as the formula only is valid for screens where $\frac{1}{D_h} < 0.015$ [Idelchik, 1960].

Alternatively the formula for a wire screen might be valid [Idelchik, 1960].

$$\zeta = k \cdot (1 - f) + (f^{-1} - 1)^2 \quad (\text{F.3})$$

Where k for clean screens equal 1.3 [Idelchik, 1960].

Using this gives the following coefficient of hydraulic resistance:

$$\zeta = 1.3 \cdot (1 - 0.57) + (0.57^{-1} - 1)^2 = 1.11 \quad (\text{F.4})$$

Horizontal Screen - Additional Results



Ratios between the predicted flow and the modelled flow as a function of the hydraulic resistance for different screen lengths and resistances.

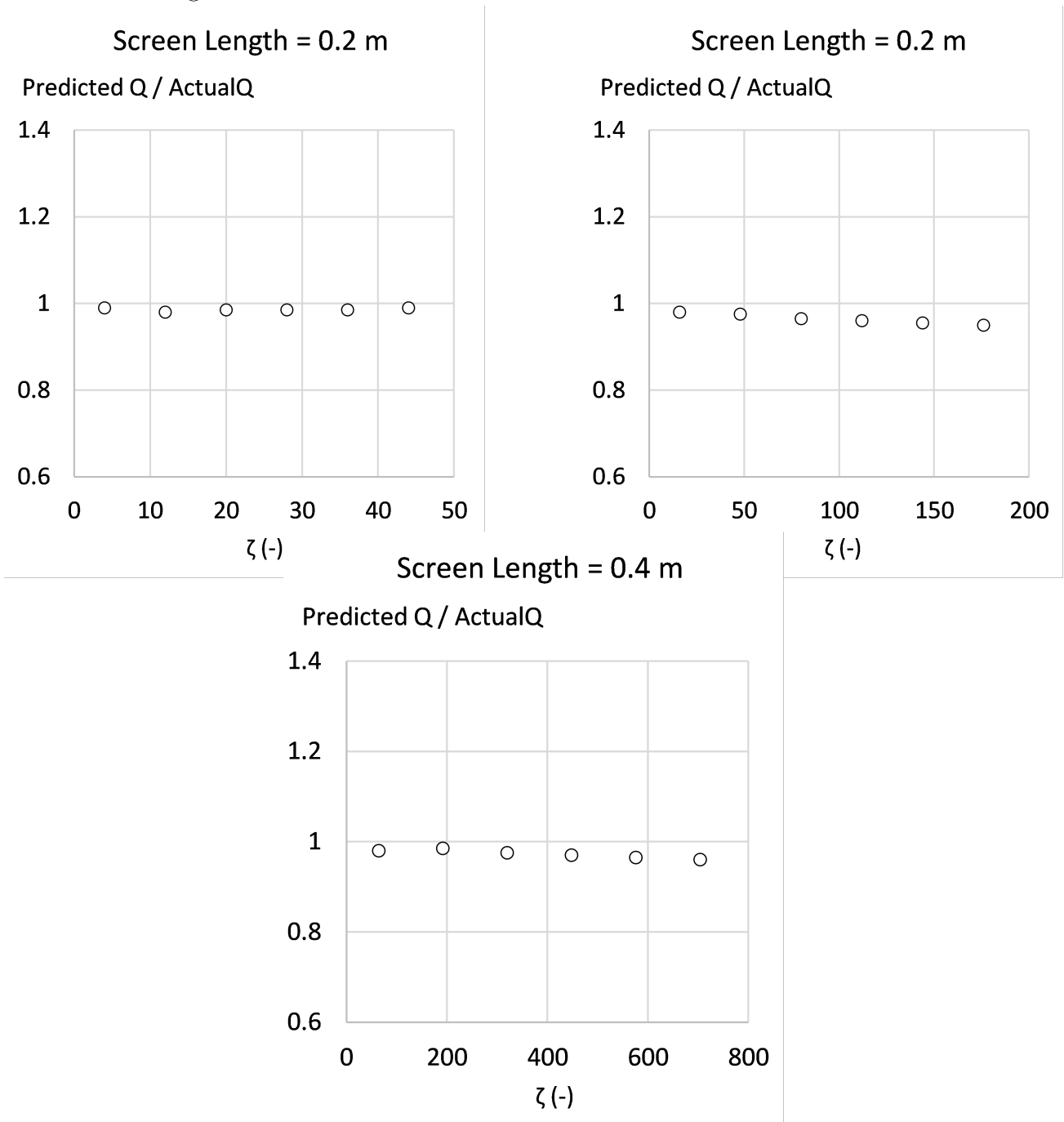


Figure G.1. Ratio between the predicted and the actual flow.

Weir Predictions Parameters



The fitted values for a, b and c used in equation 7.4 to predict the weir coefficient has been prented throughout the domain of the chamber for the stilling pond CSO structure and the side weir.

Stilling Pond CSO Structure

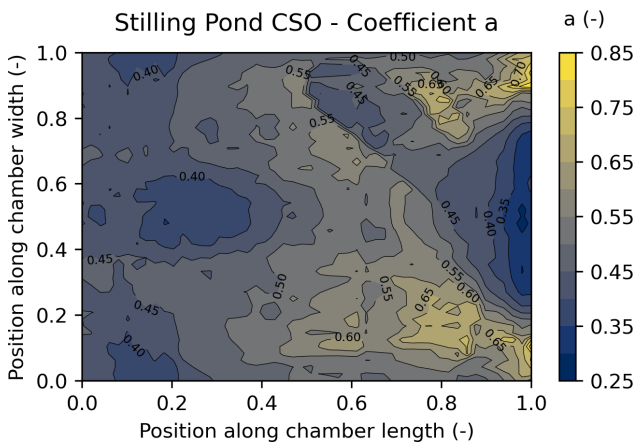


Figure H.1. Fitted values for a.

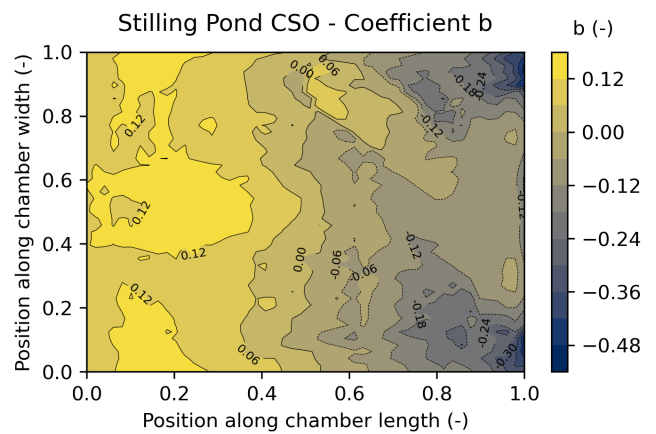


Figure H.2. Fitted values for b.

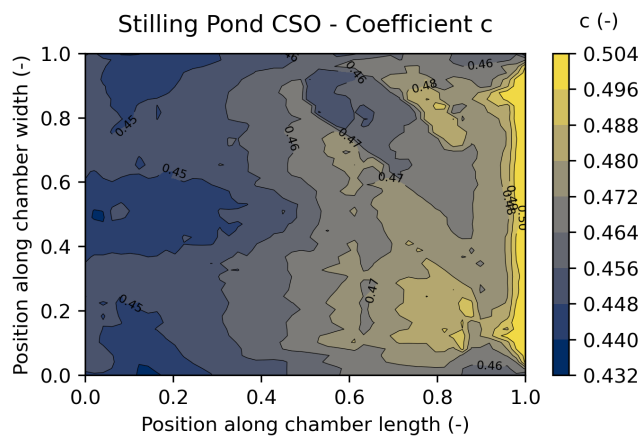


Figure H.3. Fitted values for c.

Side Weir

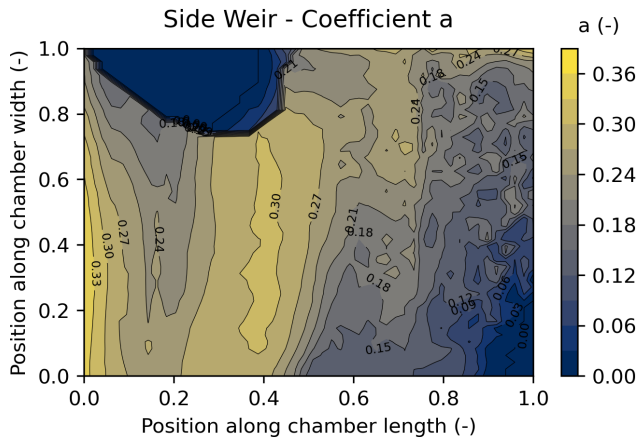


Figure H.4. Fitted values for a.

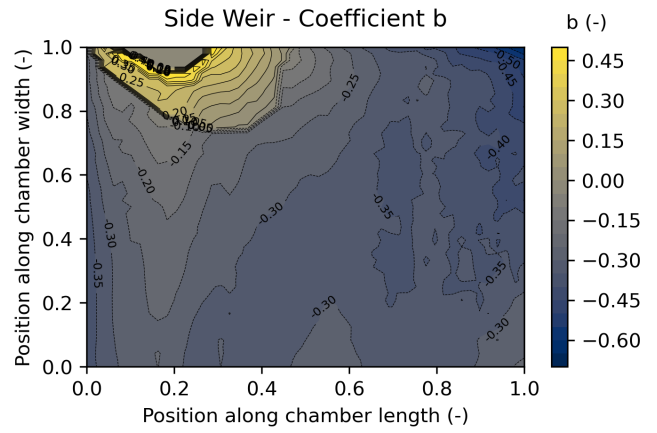


Figure H.5. Fitted values for b.

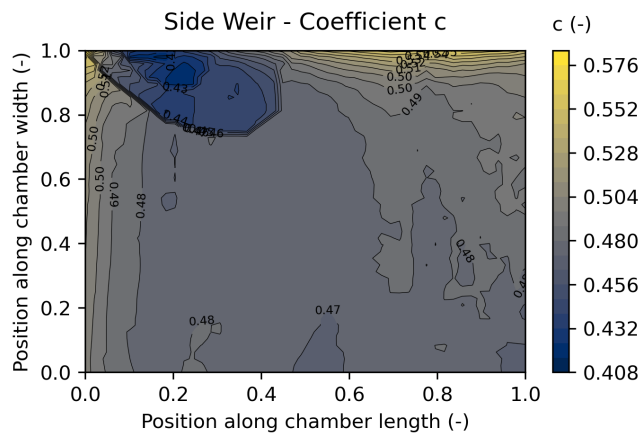


Figure H.6. Fitted values for c.